THE UNIVERSITY *of* EDINBURGH

Tidal Evolution of Dwarf Spheroidal Galaxies and Dark Matter Subhaloes

Raphaël Errani

Doctor of Philosophy
The University of Edinburgh

July 2019

I declare that this thesis was composed by myself, that the work contained herein is my own except where explicitly stated otherwise in the text, and that this work has not been submitted for any other degree or professional qualification.

Parts of this work have been published in

i) RE, J. Peñarrubia, C.F.P. Laporte & F. Gómez: The effect of a disc on the population of cuspy and cored dark matter substructures in Milky Way-like galaxies. MNRAS 465, L59-L63 (2017), arXiv:1608.01849 (Paper 1)

ii) RE, J. Peñarrubia, M. Walker: Systematics in virial mass estimators for pressure supported systems. MNRAS 481, 5073–5090 (2018), arXiv:1805.00484 (Paper 2)

iii) RE, J. Peñarrubia: Can tides disrupt cold dark matter subhaloes? Submitted to MNRAS in May 2019, arXiv:1906.01642 (Paper 3)

Raphaël Errani, July 2019

Abstract

Understanding the distribution of dark matter (DM) on galactic scales is at the root of constraining the nature of DM and processes of galaxy formation like baryonic feedback. Dwarf spheroidal galaxies (dSphs), lying at the faintest end of the galaxy luminosity function, are the most DM dominated systems known to date. They are a promising candidates to probe the DM distribution on kpc scales. In this work, we study the tidal evolution, abundance and observable properties of dSphs embedded in DM subhaloes.

Tidal evolution of subhaloes and dwarf galaxies *Chapter 2*

We run controlled simulations of the tidal evolution of a single cold dark matter subhalo with a centrally-divergent density cusp, tailored to follow the evolution of the subhalo for arbitrarily large fractions of tidally stripped mass. Based on simple dynamical arguments and numerical experiments, we argue that cuspy DM subhaloes cannot be completely disrupted by smooth tidal fields. Using a model of the Tucana III dSph galaxy as an example, we show that tides can strip dSph galaxies down to sub-solar luminosities. The remnant *micro-galaxies* would appear as co-moving groups of metal-poor, low-mass stars of similar age, embedded in sub-kpc DM subhaloes.

Subhalo depletion driven by the galactic disc *Chapter 3*

To further quantify the abundance of subhaloes in Milky Way-like galaxies containing a galactic disc, we use high-resolution re-simulations of all subhaloes of the Aquarius A2 merger tree with masses $M \geq 10^8\,\mathrm{M}_\odot$ at accretion. We model the tidal evolution of subhaloes with both cuspy and cored DM profiles, finding that cuspy models have twice as many surviving subhaloes within the virial radius of the host at redshift z=0 as their cored counterparts. The presence of a galactic disc reduces the number of surviving subhaloes further by a factor of $\lesssim 2$ for subhaloes on orbits that pass through the disc.

Mass estimates for Milky Way dwarf galaxies *Chapter 4*

With the aim of comparing observed properties of Milky Way dSph galaxies to simulations, we construct an estimator for enclosed masses based on the virial theorem, insensitive to anisotropy in the velocity dispersion and tailored to yield masses with minimum uncertainty introduced by our ignorance on (i) the shape of the inner DM profile, and (ii) how deeply the stellar component is embedded within the subhalo. Tests against controlled simulations show that the estimator provides unbiased masses with an accuracy of ~ 10 per cent. Application to published kinematic data of Milky Way dSph galaxies reveals a tight correlation between enclosed mass and luminosity. Comparison against cuspy and cored DM haloes extracted from controlled cosmological simulations shows that the high mass densities of ultrafaint galaxies are not compatible with large DM cores, and that the (total) halo masses of the classical Milky Way dSph galaxies span a remarkably narrow range ($8 \lesssim \log_{10}(M/\mathrm{M}_\odot) \lesssim 10$) at present, showing no clear trend with either galaxy size or luminosity.

Lay summary

The most successful model for gravity to date, Einstein's general relativity (1915) – coinciding in the limit of weak fields with Newton's original description (1687) – does not reproduce the motion of stars and gas on galactic scales when assuming that gravity is sourced by the observed matter alone. Evidence for the existence of *dark matter* is compelling, ranging from the seeds of cosmic structure formation to the motion of stars in the smallest of galaxies. The nature of such hypothesised dark matter is still largely unconstrained, precisely because of its fundamental property of being dark and its predominant (and perhaps only) interaction with luminous matter being through gravity. The large scale structure of the universe as mapped out by deep surveys of galaxies is well reproduced by models where dark matter interacts exclusively through gravity. Such models predict dark matter substructures on a vast range of spatial scales, with small substructures forming first and subsequently merging to build a hierarchy of *subhaloes* and *haloes*.

Our Galaxy, the Milky Way, hosts dozens of smaller satellite galaxies, and the number of known satellites has more than doubled in recent years thanks to discoveries in data acquired by wide field surveys. The motion of stars in the faintest of satellites, named *dwarf spheroidal galaxies*, suggests that these systems are dominated by dark matter, containing more dark than luminous matter by factors of thousands. These satellite galaxies therefore are a promising window into the hierarchy of dark matter subhaloes on galactic scales. With the aim of linking observable properties of dwarf spheroidal galaxies to the properties of the underlying distribution of dark matter, this thesis studies the evolution of dwarf spheroidal galaxies within a larger host galaxy like the Milky Way, using dynamical models and numerical methods.

Tidal forces of the host galaxy strip mass off dwarf galaxies. The specific response of a dwarf galaxy to these forces depends largely on its internal distribution of dark matter. Numerical simulations indicate that if dark matter interacts exclusively through gravity, the substructures it forms have centrally-divergent densities, while the presence of luminous matter or potential self-interactions may lower the central densities. We show that dwarf galaxies with centrally-divergent dark matter densities are remarkably resilient to tidal stripping, and cannot be fully disrupted by tides. In contrast, dwarf galaxies with non-diverging central densities can be disrupted. *Chapter 2*

This motivates to quantify the abundance of dark matter subhaloes and dwarf galaxies in Milky Way-like galaxies for different models of the shape of their underlying dark matter density profiles. Using controlled simulations, we show that the galactic disc drives the depletion of subhaloes in the inner regions of the galaxy, and that this depletion is particularly efficient if subhaloes have non-diverging central densities. *Chapter 3*

To compare structural properties of Milky Way dwarf spheroidal galaxies to simulated dark matter subhaloes, we develop an estimator for the masses of dwarf spheroidal galaxies based on their internal stellar motions. The estimator is tailored to minimise the uncertainty on estimated masses originating from our ignorance of the underlying distribution of dark matter. Combining the mass estimates of Milky Way dwarf spheroidal galaxies with results from controlled simulations, we show that the faintest of Milky Way satellites require dark matter subhaloes with particularly high central densities, and total halo masses that appear to be independent of the number of stars in those galaxies. *Chapter 4*

Contents

This thesis is the result of doctoral studies carried out under the guidance of Jorge Peñarrubia at the University of Edinburgh in the period November 2015 - July 2019. The findings presented in chapter 3 stem from a collaboration with Chervin Laporte (University of Victoria) and Facundo Gómez (University of La Serena), whereas the work of chapter 4 derives from a collaboration with Matthew Walker (Carnegie Mellon University). To emphasize the significance of feedback and discussions during the course of these studies, the thesis is written in the first person plural.

The structure of the thesis is different from the chronological order in which the respective studies were carried out. This allows to present in detail the tidal evolution of a single subhalo before discussing the properties of the population of subhaloes in Milky Way-like galaxies.

Submitted July 12, 2019; Viva August 19, 2019.

Chapter 1

Introduction

The clustering of cold dark matter on Mpc scales is a successful model for the observed large scale structure of the universe (Davis et al., 1985) and the driving process enabling the formation of galaxies (White & Rees, 1978). On kpc scales and smaller however, the dark matter density distribution is yet the subject of fierce debate. On these small galactic scales, potential dark matter particle properties and interactions (e.g. Tremaine & Gunn, 1979; Vogelsberger et al., 2012), including those with baryons (e.g. Navarro et al., 1996; Pontzen & Governato, 2012), leave an imprint on the density distribution, which in turn might allow insights into the nature of dark matter. Challenges on constraining the nature of dark matter arise both from the side of observation (after all dark matter is *dark*), and theoretical modelling (the range of candidates is vast).

Dwarf spheroidal (dSph) galaxies lie at the faintest end of the galaxy luminosity function, with the faintest systems known to date reaching luminosities as low as $\lesssim 10^3\,\mathrm{L}_\odot$ (for a recent review of observed dSph properties, see Simon, 2019). While similar in luminosity, velocity dispersion and metallicity to some globular clusters, dSph galaxies are more extended, with half-light radii of $10^1 \sim 10^3$ pc. In contrast to globular clusters, their internal dynamics cannot be explained by (Newtonian) gravity sourced from their stellar component alone: with dynamical mass-to-light ratios as extreme as $\sim 10^4$, dSph galaxies are the most dark matter dominated systems that are accessible to direct observation.

Using dSph galaxies as probes of the underlying potential, this thesis addresses basic questions about the dark matter distribution on galactic scales:

Can tides disrupt dark matter subhaloes and embedded dwarf galaxies?	*Chapter 2*
How many subhaloes survive the tidal interaction with the galactic disc?	*Chapter 3*
What are the masses and halo properties of Milky Way dwarf galaxies?	*Chapter 4*

The questions are being discussed in the context of dark matter models allowing for centrally-divergent density cusps, and constant-density cores, using dynamical models and controlled simulations. The spirit of these controlled simulations is of *numerical experiments* which allow to develop an intuition for the response of the system to a

range of model parameters. Different re-simulations techniques are being developed along the way to minimize numerical artefacts driven by limited resolution.

The present introduction serves to motivate both the questions asked and numerical techniques developed in this thesis. Sections 1.1 and 1.2 place the thesis work in a historical context, whereas sections 1.3 and 1.4 discuss more technically the tidal effects on subhaloes in the framework of collisionless dynamics. The N-body methods applied in later chapters to model subhaloes and their evolution in a host galaxy are being summarized in section 1.5.

1.1 Dark matter clustering

The historical overview follows Frenk & White (2012) sections 2 and 3, and van den Bosch et al. (2018) section 1. For a technical review on current DM simulations, see Kuhlen et al. (2012).

In the ΛCDM picture, matter forms structures through gravitational collapse in an expanding universe, seeded by primordial density fluctuation. The observed large scale structure of the cosmic web as mapped out by deep spectroscopic surveys (e.g. Davis et al., 1982; Zehavi et al., 2002) is well described through the clustering of cold dark matter (CDM) (e.g. Blumenthal et al., 1984; Bond et al., 1996). Small clumps form first through gravitational collapse and merge to build the hierarchy of clusters, haloes and subhaloes (Fig. 1a), arranged in intersecting sheets and filaments throughout the universe. Galaxies are subsequently formed from gas that is accreted into and cools within the deep potential wells of dark matter haloes (White & Rees, 1978).

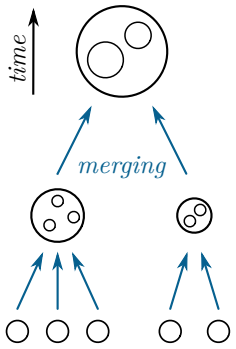

Fig. 1a: *The smallest cold dark matter substructures form first and subsequently merge* bottom-up, *forming a hierarchy of haloes and subhaloes.*

The advances in studying the non-linear structure formation were closely tied to the development of numerical methods and the availability of computational resources that allowed to model gravitating systems of increasing complexity. The cosmological N-body simulations (albeit assuming Einstein-de-Sitter cosmology) of Aarseth et al. (1979) used $N = 4000$ particles to study large-scale structure formation, approximating the gravitational force due to distant particles to avoid the numerically expensive $\mathcal{O}(N^2)$ direct summation of forces. Solving Poisson's equation on a grid in Fourier space and summing forces for nearby objects directly, Efstathiou & Eastwood (1981) increased the number of simulated particles to $N = 20000$. The formation of CDM structures in a flat universe with density parameter $\Omega_\mathrm{m} = 0.2$ was first studied by Davis et al. (1985) with $N = 32^3 = 32768$ particles, using a Fourier approach.

Tree codes (Fig. 1b) allowed for a further increase in particle number N, with force calculations scaling as $\mathcal{O}(N \ln N)$ (Barnes & Hut, 1986) and more recently as $\mathcal{O}(N)$ (Dehnen, 2002). While DM haloes in early simulations were devoid of substructures, in contradiction to the observed substructures in galaxy clusters and galaxies (an issue dubbed *overmerging*, e.g. Klypin et al., 1999a), once simulations had sufficient resolution to probe the scales in question, haloes were found to host vast hierarchy of substructures: Tormen et al. (1997) used the Navarro & White (1993) tree code to re-simulate cluster haloes and study the mass evolution due to the accretion of substructures, starting from a cosmological simulation with 10^6 particles, and resolving

main haloes at $\sim 10^4$ particles. Moore et al. (1998) identified 10^3 substructures in a main cluster halo containing 3×10^6 N-body particles within its virial radius.

Substructures in galactic haloes (Fig. 1c) are resolved by current DM-only simulations down to subhaloes of masses of $\sim 10^5\,\mathrm{M}_\odot$, with main galactic haloes containing $10^8 - 10^9$ N-body particles (Springel et al., 2008; Griffen et al., 2016). These are the scales studied in this thesis, and subsection 1.1.1 summarizes structural and statistical properties of DM haloes and subhaloes as inferred from DM-only simulations.

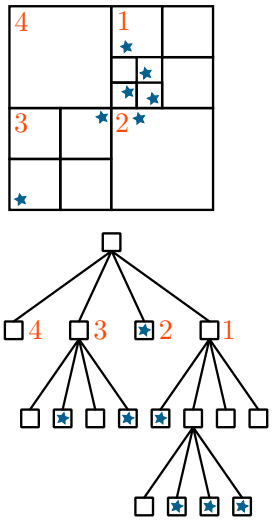

Fig. 1b: *A* tree code *groups particles in space. The force by distant particles may be approximated by the net force of a branch of the tree, reducing the number total force calculations. In contrast,* particle mesh *(Fourier) methods as used in this thesis are discussed in section 1.5.1.*

1.1.1 Substructure within haloes

Within the virial radius of the main halo, roughly ten per cent of mass are bound in subhaloes (Springel et al., 2008). The abundance N of subhaloes scales with their mass M: low-mass subhaloes are more frequent than more massive ones. For subhaloes in Milky Way-like main haloes, Gao et al. (2004) and Springel et al. (2008) measure from simulations that at redshift $z = 0$,

$$\frac{\mathrm{d}N}{\mathrm{d}M} \propto M^{-1.9} \,. \tag{1.1}$$

The shape of DM halo density profiles is universal in the sense that it does not depend on halo mass or redshift. Densities of DM haloes are frequently parametrized using the spherical Navarro et al. (1997) (hereafter NFW) profile,

$$\rho_{\mathrm{NFW}}(r) = \frac{\rho_s}{(r/r_s)(1 + r/r_s)^2} \,. \tag{1.2}$$

In the above equation, r_s and ρ_s are a scale radius and scale density, respectively. Denoting by M_s the mass enclosed within r_s, as $M(< r) = 4\pi\rho_s r_s^3\,[\ln\left((r + r_s)/r_s\right) - r/(r_s + r)]$, scale mass and density are related by $M_s = 4\pi\rho_s r_s^3[\ln(2) - 1/2]$.

Equation 1.2 is often expressed in terms virial radius r_{200}, virial mass M_{200} and concentration $c = r_{200}/r_s$. The virial radius r_{200} encloses a mean density 200 times larger than the critical density of the universe $\rho_c = 3H^2/8\pi G$ (where H is the Hubble parameter), and the virial mass is the mass enclosed within that radius, i.e. $M_{200}/(4\pi r_{200}^3/3) = 200\,\rho_c$.

Gao et al. (2008) find that for radii $10^{-2} < r/r_{200} < 1$, the NFW profile matches simulated haloes with deviations of $\lesssim 10$ per cent, where the largest deviations arise in the inner regions of the halo: The inner slope $\gamma = -\partial \ln \rho / \partial \ln r$ might differ from the NFW value of ($\gamma = 1$), though Navarro et al. (2004) and Hayashi et al. (2004) constrain the slope to be shallower than $\gamma \lesssim 1.5$.

Within the resolution limits of current simulations, also the Einasto density profile

$$\rho_{\mathrm{E}}(r) = \rho_{-2} \exp\left\{-\frac{2}{\alpha}\left[\left(\frac{r}{r_{-2}}\right)^{\alpha} - 1\right]\right\} \tag{1.3}$$

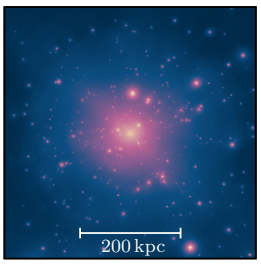

Fig. 1c: *Dark matter substructures in a Milky Way-like halo: snapshot at redshift $z = 0$ of the simulation introduced in chapter 3. For a larger version, see Fig. 3.A.1, p.66.*

with shape parameter α and a rolling power-law slope $\partial \ln \rho_{\rm E} / \partial \ln r = -2\,(r/r_{-2})^{\alpha}$ provides a good match to simulated DM haloes (Gao et al., 2008; Navarro et al., 2010). This also holds when fixing the shape parameter to $\alpha \sim 0.16$ and thereby having the same number of free parameters as the NFW profile (Springel et al., 2008). In equation 1.3, r_{-2} denotes the radius at which $\partial \ln \rho / \partial \ln r = -2$, and $\rho_{-2} = \rho(r_{-2})$. In a spherical system, independently of chosen density profile, this is the radius which contains the largest fraction of total mass as $\mathrm{d}^2 m / \mathrm{d}r^2 = \mathrm{d}/\mathrm{d}r \left[4\pi r^2 \rho(r)\right] = 0$ for $r = r_{-2}$. For NFW profiles, $r_s = r_{-2}$, and $\rho_{-2} = \rho_s / 4$.

Numerical simulations show that DM haloes are better described by triaxial density profiles than by spherical models (Frenk et al., 1988). Cole & Lacey (1996) find axis ratios of typically $1 : 0.8 : 0.65$ at the virial radius, with inner halo regions being gradually more spherical. Despali et al. (2014) study the redshift evolution of triaxiality, finding that at fixed halo mass, deviations from sphericity increase with increasing redshift, and at fixed redshift, more massive haloes are less spherical. With the focus of this thesis being low-mass subhaloes at redshift $z = 0$, for sake of simplicity, density profiles adopted in this thesis for DM subhaloes assume spherical symmetry.

Masses and sizes of haloes are correlated, and different empirical mass-concentration-redshift relations have been derived from simulations (e.g. Prada et al., 2012; Ludlow et al., 2014). For subhaloes, per definition located within a larger main halo, the definition of concentration c with respect to the critial density of the universe becomes ambiguous. In this thesis, we therefore prefer to parametrize subhaloes using masses and sizes directly, and frequently will refer to the mass $M_{\rm max}$ enclosed within the radius $r_{\rm max}$ where the circular velocity curve peaks:

$$v_{\rm max} = \max \left[\left(\frac{GM(<r)}{r} \right)^{1/2} \right] = \left(\frac{GM_{\rm max}}{r_{\rm max}} \right)^{1/2} \quad . \tag{1.4}$$

This choice of parameters also has the advantage of being defined independently of a particular DM halo profile. Springel et al. (2008) find in the Aquarius simulations that subhalo mass M and $v_{\rm max}$ scale on average as $M \propto v_{\rm max}^{3.5}$, whereas Klypin et al. (2011) measure from the Bolshoi simulations $M \propto v_{\rm max}^{3.3}$. Assuming $M \propto M_{\rm max}$, then (to one significant figure in the exponent)

$$r_{\rm max} \propto M_{\rm max}^{0.4} \ , \tag{1.5}$$

which is an approximative relation that will be used for order-of-magnitude estimates throughout the thesis. Application of this relation between halo mass and size to NFW haloes has an interesting consequence: for a fixed radius r, the most massive NFW haloes also have the highest density $\rho_{\rm NFW}(r)$. This is shown in Figure 1.1, where density profiles scaling according to equation 1.5 do not intersect.

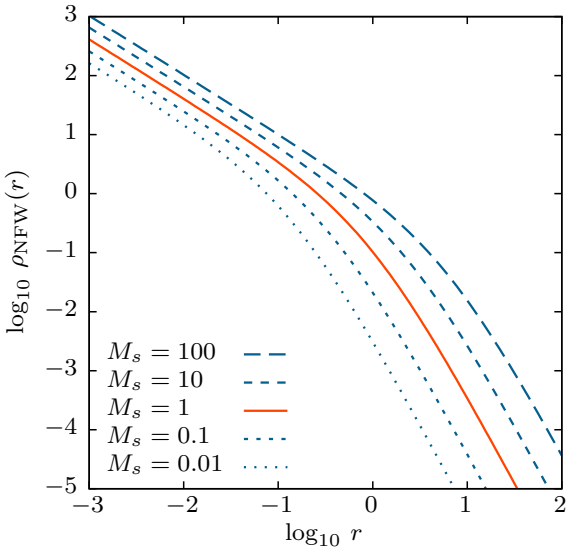

Figure 1.1: The most massive NFW haloes also have the highest densities: haloes following the mean mass - size relation of equation 1.5 have density profiles (equation 1.2) that do not intersect. The plot uses dimensionless quantities normalised so that $r_s = 1$ for $M_s = 1$.

1.2 Dwarf spheroidal galaxies

Observed structural and kinematic properties of Milky Way dwarf galaxies are summarized in the reviews by Simon (2019), McConnachie (2012) and Mateo (1998).

Dwarf spheroidal galaxies (dSphs) with luminosities spanning between $10^2 \lesssim L/\mathrm{L}_\odot \lesssim 10^8$ and dynamical mass-to-light ratios reaching values as extreme as $\langle M/L \rangle \sim 10^4$ include the faintest and most dark matter dominated systems known to date (Simon, 2019). The metallicities of ultra-faint dwarfs reach values as low as [Fe/H] $= -3$, indicating their origin in earliest processes of galaxy formation. Two of the brightest Milky Way dSphs, the Fornax and Sculptor dwarfs, are shown in Figure 1.2. The dynamical mass-to-light ratios of these two galaxies are of order ~ 10 (see section 4.5.5).

Figure 1.3 gives an overview of luminosities, half-light radii, velocity dispersions and metallicities of a sample of Milky Way dwarf galaxies, highlighting that on average with decreasing luminosity, also half-light radius and metallicity decrease (for references and numerical values, see table 4.2 on page 90). The correlation between luminosity and metallicity has been parametrised by Kirby et al. (2013) as $[\mathrm{Fe/H}] \approx -3.5 + 0.3 \times \log_{10}[L/\mathrm{L}_\odot]$ with a scatter of approximately 0.2 dex around the relation. Similarly, the luminosity-size relation of observed dwarf spheroidal galaxies follows approximately a power-law, however caution has to be taken as the relation may be driven by surface brightness selection effects: the dashed line in Figure 1.3 indicates the slope of constant surface brightness Σ, which results similar to the slope of the observed luminosity-size relation (see also McConnachie, 2012, figures 6 and 7).

Recent years have seen an increase in the number of known Milky Way dwarfs to a total of ~ 50 to date, driven by deep photometric and spectroscopic surveys, covering large areas of the sky (for dwarfs discovered in Sloan Digital Sky Survey (SDSS) data, see e.g. Belokurov et al. 2008, 2010; for discoveries in Dark Energy Survey (DES) data, see e.g. Bechtol et al. 2015; Drlica-Wagner et al. 2015; Koposov et al. 2015).

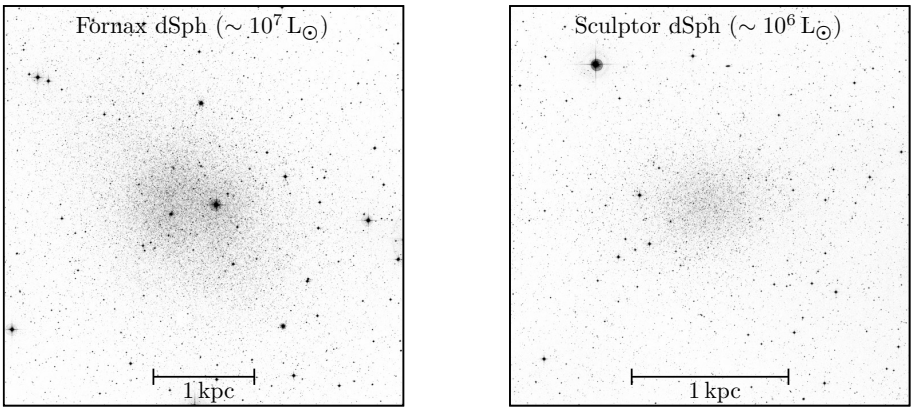

Figure 1.2: The Fornax and Sculptor dwarf spheroidal galaxies in the Milky Way. Each image covers an area of one square degree on the sky. A scale corresponding to 1 kpc at the respective distances of the dwarf galaxies is shown at the bottom of the frame. The scans of the original photographic plates were obtained from the ESO online archives of the DSS2-*red* catalogue, and correspond to 1 hour exposures taken with the UK Schmidt Telescope (1.24 m diameter) using a filter with wavelength coverage from 590 nm – 690 nm.

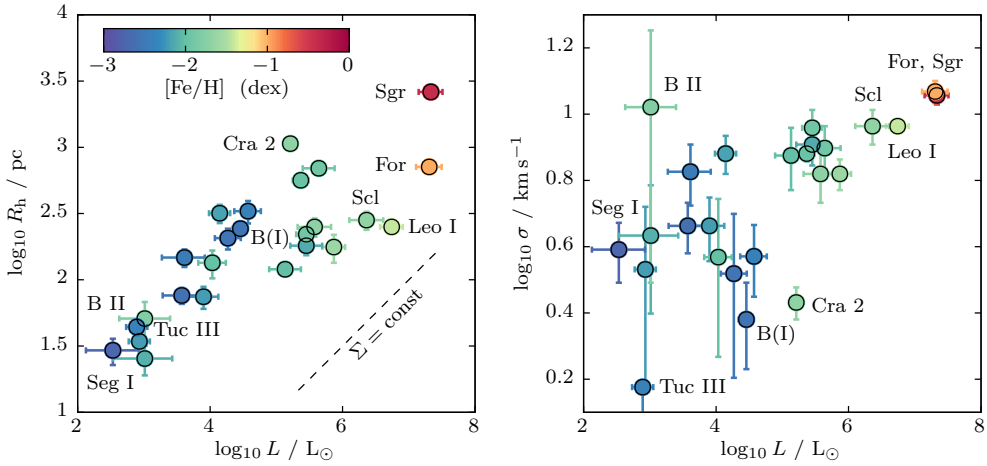

Figure 1.3: V-band luminosities L, half-light radii R_h and velocity dispersions σ for a sample of Milky Way dwarf galaxies. The metallicity [Fe/H] is colour-coded. Abbreviations refer to Bootes I+II (B), Crater 2 (Cra), Fornax (For), Sagittarius (Sgr), Sculptor (Scl), Segue I (Seg). For Tucana III (Tuc), the Simon et al. (2017) upper limit on the velocity dispersion is shown. References and numerical values are listed in table 4.2 on page 90. The slope of the dashed line corresponds to constant surface brightness Σ, indicating that the luminosity-size relation may be driven by selection effects.

With dynamical masses as low as $\sim 10^5\,\mathrm{M}_\odot$ (Tucana III dwarf, Simon et al., 2017) or $\sim 10^6\,\mathrm{M}_\odot$ (Crater II dwarf, Caldwell et al., 2017), these systems probe the scale of DM subhaloes.

Explaining abundances and structural properties of dSph galaxies in the framework of CDM is a compelling challenge as it ties some of the most fundamental properties of dark matter – its small-scale structure and dynamics – to observable systems in the local universe. Subsection 1.2.1 discusses some of the observed properties of dSphs in the light of CDM.

1.2.1 Confrontation with CDM predictions

Satellite abundances

See Bullock & Boylan-Kolchin (2017) and Strigari (2018) for a discussion of dwarf galaxies in the frame of CDM.

If CDM consists of WIMPS (*weakly interacting massive particles* with a mass of $\sim 100\,\mathrm{GeV/c^2}$), the smallest substructures it forms are of earth mass ($\sim 10^{-6}\,\mathrm{M}_\odot$), as determined by the free-streaming length. Simulations suggest that these substructures would survive tidal stripping in the Milky Way, resulting in a total of 10^{15} CDM subhaloes at redshift $z = 0$ (Diemand et al., 2005). On larger scales, extrapolating from simulations of galaxy clusters, Moore et al. (1999) predict around ~ 500 CDM substructures with bound masses $\gtrsim 10^8\,\mathrm{M}_\odot$ in a Milky Way-like halo, and indeed the Aquarius A2 halo (Springel et al., 2008) contains ~ 1000 subhaloes of this mass scale. These numbers are one order of magnitude larger than the number of known Milky Way dwarfs. As Klypin et al. (1999b) phrases it: *Where are the missing satellites?*

Solutions to this discrepancy can be found within CDM though baryonic physics: galaxy formation is suppressed in low-mass haloes due to i) inefficient cooling of gas during HI re-ionization (Bullock et al., 2000; Gnedin, 2000; Benson et al., 2002) and ii) supernova feedback (Dekel & Silk, 1986). Furthermore, the presence of a galactic disc increases the rate of tidal stripping compared to DM-only simulations (see e.g. D'Onghia et al. 2010, Peñarrubia et al. 2010 and chapter 3 of this thesis). All three processes can lead to DM haloes which do not contain any stars. Outside of classical CDM models, low-mass warm DM forms less substructures on galactic scales (Lovell et al., 2014).

Dark matter profiles

Dynamical masses of dSphs are generally estimated from combined measurements of their stellar half-light radii R_h and luminosity-averaged stellar velocity dispersions σ. Using Jeans analysis, Walker et al. (2009c) derived an estimator for the mass $M(< R_\mathrm{h})$ enclosed within the half-light radius for isotropic systems with flat velocity dispersion profiles $\sigma(R) = \mathrm{const}$:

$$M(< R_\mathrm{h}) \approx \frac{5\,R_\mathrm{h}\,\sigma^2}{2\,G}\ . \tag{1.6}$$

A similar relation was later proposed by Wolf et al. (2010), and chapter 4 of this thesis is dedicated to minimize the uncertainty on inferred masses originating from our ignorance on the underlying dark matter profile and the anisotropy of the stellar velocity dispersion.

Strigari et al. (2008) discuss a common mass scale for dSph galaxies of $\sim 10^7\,\mathrm{M}_\odot$ for the mass enclosed within their inner 300 pc. In this context, motivated by the correlation of half-light radii R_h and enclosed masses $M(< R_\mathrm{h})$, Walker et al. (2009c, see fig. 5) argue that within observational uncertainties, a (single) *universal* DM halo profile (e.g. a NFW profile with scale radius $r_s \approx 0.80\,\mathrm{kpc}$ and scale mass $M_s \approx 3.8 \times 10^7\,\mathrm{M}_\odot$ for all dSphs) is consistent with the Milky Way dSphs – though this simple model was later disfavoured with the availability of more data (see e.g. Collins et al., 2014, for Andromeda dSphs, and Figure 4.9 in this thesis for Milky Way dSphs).

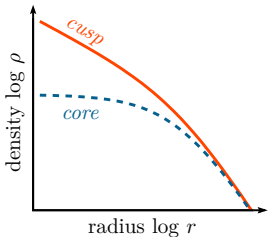

Fig. 1d: *Centrally divergent density profiles are dubbed* cuspy *in distinction to profiles with a constant-density* core.

Density slopes. Using estimates of enclosed masses for two distinct stellar populations, Walker & Peñarrubia (2011) computed the slope of the underlying DM density profiles for the Fornax and Sculptor dSph galaxies. Their findings suggest that both Fornax and Sculptor are embedded in DM haloes with constant-density cores, as opposed to centrally-divergent density cusps found in DM-only simulations (Fig. 1d). There is no consensus on the central slope of DM haloes in dwarf galaxies, Richardson & Fairbairn (2014) argue in favour of a cuspy DM profile for Sculptor, whereas Amorisco & Evans (2012) and Amorisco et al. (2013) argue in favour of DM cores in both Sculptor and Fornax.

Baryons might also in this context ease apparent tensions between CDM cusps and observed cores: gravitational heating through baryonic substructures (e.g. Nipoti & Binney, 2015) and supernova feedback (e.g. Navarro et al., 1996; Read & Gilmore, 2005; Pontzen & Governato, 2012; Di Cintio et al., 2014; Oñorbe et al., 2015) might dissolve central density cusps – though the efficiency of these processes has been challenged (see e.g. Laporte & White, 2015; Peñarrubia et al., 2012). Similarly, self-interacting DM (e.g. Spergel & Steinhardt, 2000) and DM models with sufficiently small particle mass (Tremaine & Gunn, 1979) may prevent DM cusps to form – though Macciò et al. (2012) finds that particle masses consistent with core sizes of $r_c \sim 1\,\mathrm{kpc}$ (as estimated for the Fornax dwarf in Amorisco et al., 2013) would prevent the formation of dwarf galaxies in the first place.

Mean densities. The central densities of the most massive subhaloes in DM-only simulations are too large to be compatible with the inferred mean densities of the brightest Milky Way dwarfs (Boylan-Kolchin et al., 2011). Fattahi et al. (2016) argue that underestimated observational uncertainties are the driving cause of the apparent discrepancy between simulated and measured mean densities. Taking the measured densities of Milky Way dwarfs at face value, a potential solution to the discrepancy with DM-only simulations is stellar feedback: using hydrodynamical simulations, Oñorbe et al. (2015) show that feedback can form DM cores in the

centres of subhaloes, lowering the DM densities sufficiently to be compatible with the observations. However, subhaloes in numerical simulations that include stellar feedback still have less scatter in their structural properties than observed for Milky Way dwarf galaxies (Oman et al., 2015).

Orbital distribution

Lynden-Bell (1976) noted that multiple Milky Way dSph galaxies (Sculptor, Draco and Ursa Minor) have orbits that lie approximately in the same polar plane. Kroupa et al. (2005) argue that such a planar configuration is incompatible with CDM halo accretion. In contrast, based on a more detailed model of subhalo orbital parameters derived from cosmological simulations, Zentner et al. (2005) find that the observed distribution is marginally compatible with their simulations. Libeskind et al. (2005) interpret the planar structure of orbits as a result of subhalo accretion along preferential directions determined by the filaments of the cosmic web.

A similar plane of co-rotating satellites is observed around the Andromeda galaxy (Ibata et al., 2013), and Ibata et al. (2014) argue that such orbital configurations occur in cosmological simulations only in about ~ 0.04 per cent of host haloes and are generally associated to group infall. More recently, Sawala et al. (2016) report orbital distributions akin to those of Milky Way and Andromeda dwarfs in the APOSTLE simulations which are tailored to match the statistical properties of the Local Group.

A different approach using orbital kinematics to confront CDM predictions and observations is taken by Cautun & Frenk (2017), who compare the distribution of radial and tangential systemic velocities of Milky Way dwarfs to those of cosmological simulations. They find that the sample of 10 studied Milky Way dwarfs has a tangentially biased systemic velocity dispersion compatible only at the ~ 3 per cent level with simulations. Using Gaia proper motions for 38 Milky Way satellites, Riley et al. (2019) show that their studied sample has tangentially biased systemic velocity dispersions in the central regions of the Milky Way, and radially biased dispersions around the virial radius – noting that such a distribution is not found in any of the Milky Way-like haloes of the APOSTLE simulations, but that similar trends are observed in simulations of higher-mass galaxies.

In this context, chapter 3 of this thesis details the tidal stripping of subhaloes due to the galactic disc, resulting in a depletion of subhaloes on orbits with pericentre distances that fall within the disc.

1.3 Tidal interaction

This thesis focuses on the tidal evolution of satellites in a larger host galaxy, be it dwarf galaxies or dark matter subhaloes. The following sections discuss the effects of the host potential on the satellite. This is done by means of simple analytical approximations, with the aim to develop an intuition for the dynamical processes studied in later chapters using simulations. Section 1.3.1 introduces dynamical friction which drives the orbital decay of massive satellites and thereby exposes them to the stronger tidal fields in the center of the Milky Way. Tidal stripping on (near) circular orbits is discussed in section 1.3.2, and disc shocking in the impulsive approximation in section 1.3.3. The adiabatic response of the central regions of satellites to tidal shocks is described in section 1.3.4.

1.3.1 Dynamical friction

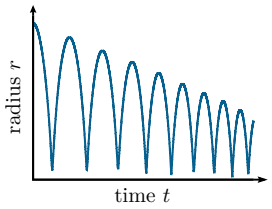

Fig. 1e: *Dynamical friction causes the radius of an orbit to decay.*

When an object of mass M moves within some background medium of density ρ consisting of smaller masses m, it experiences a drag force opposite to its direction of motion. This drag force causes a decrease of the orbital radius over time, and forces massive satellites to sink towards the centre of their host galaxies (Fig. 1e). An approximative analytical description for this effect was derived by Chandrasekhar (1943) for a mass M moving in a homogeneous background medium. For $M \gg m$ and under the assumption of an isotropic Maxwellian distribution of relative velocities with dispersion σ, the drag force reads (see BT87 eq. 7-18.):

$$\frac{\mathrm{d}\vec{v}}{\mathrm{d}t} = -\frac{4\pi \ln\Lambda G^2 M \rho(\vec{r})}{v^3}\left(\mathrm{erf}(x) - \frac{2x}{\sqrt{\pi}}\exp(-x^2)\right)\vec{v} \tag{1.7}$$

where $x = v/\left[\sigma(\vec{r})\sqrt{2}\right]$ and $\ln\Lambda = \ln(b_{\max}/b_{\min})$ is the Coulomb logarithm, $b_{\max}$ and $b_{\min}$ denoting the maximum and minimum impact parameter, respectively. The derivation of equation 1.7 involves similar steps as the estimate of relaxation times detailed in section 1.4, but allows for a hyperbolic orbit of the mass M relative to the background mass m. Chandrasekhar (1943) chooses as minimum impact parameter the smallest separation for a given relative velocity v so that the two masses remain gravitationally unbound, which for $M \gg m$ yields $b_{\min} = GM/v^2$. The choice of the upper limit on the impact parameter $b_{\max}$ is not well-defined, gravity being a force of long range. In this thesis, for models including dynamical friction, the value of $\ln\Lambda$ is therefore chosen empirically using simulations, as discussed in chapter 3.

1.3.2 Tidal stripping

This section follows the introduction in Renaud et al. (2011). Similar discussions can be found in BT87 chapter 7.3 and MD99 chapter 3.

An extended satellite moving in the host galaxy potential $\Phi_{\rm host}(\vec{r})$ feels a tidal force due to the change of the gravitational force $\vec{\nabla}\Phi_{\rm host}$ within the satellite. Generally two regimes of tidal interactions with the host can be distinguished: (i) gradual interactions for satellites on (near) circular orbits where the tidal force as seen in a co-rotating frame of reference does not evolve with time, and (ii) shocks where the satellite plunges into regions of strong tidal forces for short periods of time. Shocks are discussed in the next section, whereas this section focuses on the tidal force experienced by a satellite on a circular orbit.

Relative to a frame of reference co-rotating with the satellite (Fig. 1f) at an angular frequency ω around the centre of mass between host and satellite, the accelerations on a test particle are:

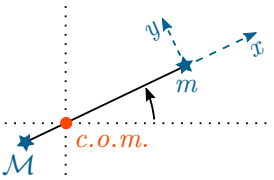

Fig. 1f: *Reference frame rotating with the masses $\mathcal{M}$ and m around the common centre of mass.*

$$\frac{\mathrm{d}^2\vec{r}}{\mathrm{d}t^2} = \underbrace{-\vec{\nabla}\Phi_{\rm sub}(\vec{r}) - \vec{\nabla}\Phi_{\rm host}(\vec{r})}_{\text{gravity}} \underbrace{\overbrace{-\vec{\omega}\times(\vec{\omega}\times\vec{r})}^{\text{centripetal}} \overbrace{-\frac{\mathrm{d}\vec{\omega}}{\mathrm{d}t}\times\vec{r}}^{\text{Euler}} \overbrace{-2\vec{\omega}\times\frac{\mathrm{d}\vec{r}}{\mathrm{d}t}}^{\text{Coriolis}}}_{\text{non-inertial frame}} , \quad (1.8)$$

where centripetal, Euler and Coriolis accelerations are a result of this choice of non-inertial frame of reference. For circular orbits, $\vec{\omega} = \text{const}$, and the Euler force vanishes. Furthermore the centripetal acceleration can be derived from a scalar potential, which motivates the definition of an effective potential

$$\Phi_{\rm eff}(\vec{r}) = \Phi_{\rm sub}(\vec{r}) \; + \; \underbrace{\Phi_{\rm host}(\vec{r}) - \frac{1}{2}\left|\vec{\omega}\times\vec{r}\right|^2}_{\text{tides}} \; = \Phi_{\rm sub}(\vec{r}) \; + \; \Phi_{\rm t}(\vec{r}), \quad (1.9)$$

where by $\Phi_{\rm t}(\vec{r})$ we denote the contribution by tidal forces. For the effective potential $\Phi_{\rm eff}(\vec{r})$, the Jacobi integral E_J is an integral of motion:

An integral of motion $E(\vec{r},\vec{v})$ is a function of the phase space coordinates so that along each orbit, $\mathrm{d}E(\vec{r}(t),\vec{v}(t))/\mathrm{d}t = 0$.
Note that the Coriolis force is perpendicular to $\vec{v}$ and does therefore not contribute to the kinetic or effective potential energy of a particle:
$\mathrm{d}E = (-2\vec{\omega}\times\vec{v})\cdot\mathrm{d}\vec{r} = 0$.

$$E_{\rm J} = \frac{1}{2}v^2 + \Phi_{\rm eff}(\vec{r}) = \text{const} \; . \quad (1.10)$$

The top panel of figure 1.4 shows $\Phi_{\rm eff}(x)$ for two point masses $\mathcal{M} = 1$ and $m = 1/5$ at unit distance $\Delta x = 1$. Along the axis x connecting the two point masses, $\Phi_{\rm eff}(x)$ has three stationary points, the Lagrange points L_1, L_2, L_3. These points separate regions in the co-moving frame where particles with a specific Jacobi integral $E_{\rm J}$ are bound either to the mass $\mathcal{M}$, to the mass m or to both. The bottom panel of figure 1.4 shows zero-velocity curves of $E_{\rm J}$. These are curves of constant $\Phi_{\rm eff}$ which a particle with $\vec{v} = 0$ cannot surpass. Coloured zero-velocity curves correspond to values of $\Phi_{\rm eff}(L_1)$, $\Phi_{\rm eff}(L_2)$, $\Phi_{\rm eff}(L_3)$ (separatrices).

Consider now a satellite galaxy of mass m on a circular orbit around a host galaxy of mass $\mathcal{M}$. Particles originally belonging to the satellite with Jacobi integrals E_J larger than $\Phi_{\rm eff}(L_1)$ or $\Phi_{\rm eff}(L_2)$ are tidally stripped from the satellite. Particles which

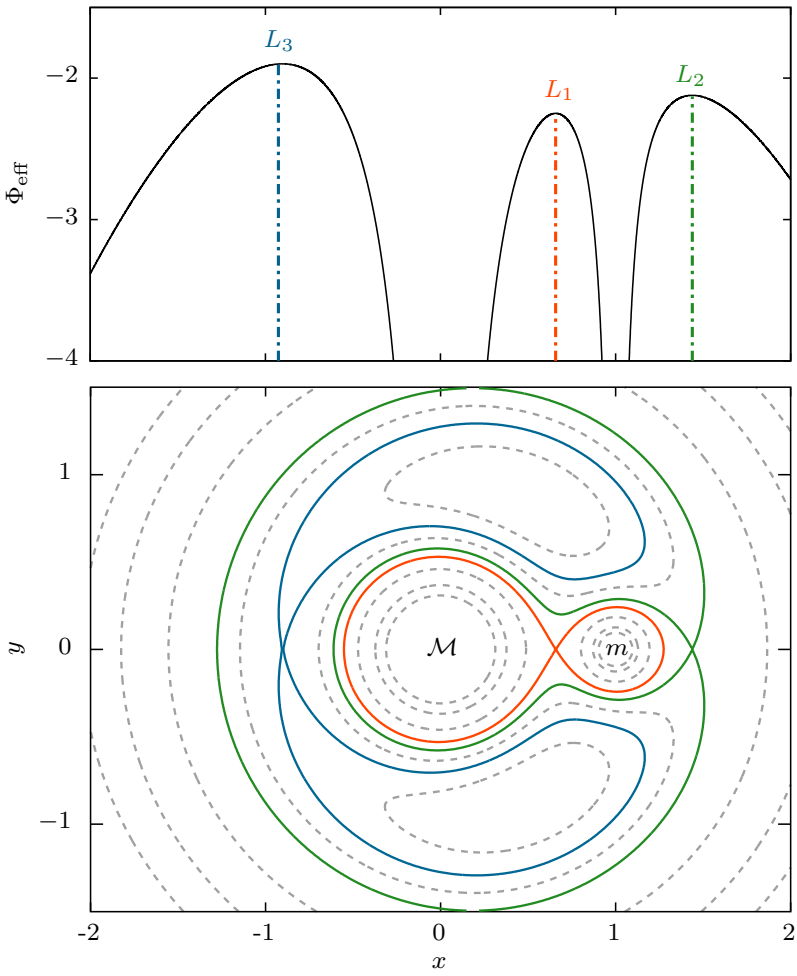

Figure 1.4: Top panel: effective potential $\Phi_{\rm eff}$ in a co-rotating frame of reference for two point masses $\mathcal{M} = 1$ and $m = 1/5$ at unit distance $\Delta x = 1$, showing three stationary Lagrange points L_1, L_2, L_3. Bottom panel: zero-velocity curves for selected values of constant $\Phi_{\rm eff}$. Separatrices corresponding to $\Phi_{\rm eff}(L_1)$, $\Phi_{\rm eff}(L_2)$, $\Phi_{\rm eff}(L_3)$ are shown in colour. In the context of a satellite (mass m) on an orbit in a more massive host galaxy (mass $\mathcal{M}$), particles with Jacobi integrals larger than either $\Phi_{\rm eff}(L_1)$ or $\Phi_{\rm eff}(L_2)$ can escape the potential well of the satellite. Particles escaping through L_1 (passing the orange separatrix towards $\mathcal{M}$) form the leading tidal stream, whereas particles escaping through L_2 form the trailing tidal stream (passing the green separatrix outwards).

escape through L_1 form the leading tidal stream with orbital periods in the host halo smaller than the orbital period of the satellite. Similarly particles that escape through L_2 form the trailing tidal stream with orbital periods longer than the orbital period of the satellite.

The distance of L_1 and L_2 to the centre of the satellite may be estimated in linear approximation. For this purpose, the tidal acceleration of a test particle is approximated by Taylor expanding the net force $\vec{\nabla}\Phi_\mathrm{t}(\vec{r})$ resulting from the effective tidal potential $\Phi_\mathrm{t}(\vec{r})$. The first term of the expansion around the satellite centre is the effective tidal tensor (see Renaud et al., 2011):

$$T_{jk}(\vec{r}) = -\left.\frac{\partial^2\Phi_\mathrm{t}}{\partial r_j \partial r_k}\right|_{\vec{r}} = \mathrm{diag}(\lambda_1, \lambda_2, \lambda_3) \ , \tag{1.11}$$

where $\lambda_1 \geq \lambda_2 \geq \lambda_3$. In this linear approximation, the Lagrange points L_1 and L_2 lie at a distance

$$r_t = \left(\frac{Gm}{\lambda_1}\right)^{1/3} \tag{1.12}$$

to the satellite centre: the tidal radius. For a point-mass galaxy of mass $\mathcal{M}$ at a separation x to the satellite, $\{\lambda_1, \lambda_2, \lambda_3\} = G\mathcal{M}x^{-3}\{3, 0, -1\}$ and $r_t = x[m/(3\mathcal{M})]^{1/3}$.

1.3.3 Impulsive disc shocking

See e.g. S87 chapter 5.2 and BT87 chapter 7.2.

Strong tidal perturbations that act for a brief amount of time are referred to as tidal shocks. Satellites experience this type of interaction when passing through the galactic disc (disc shocking, see Ostriker et al., 1972) or when eccentric orbits bring them close to the centre of the host galaxy (bulge shocking, see Aguilar et al., 1988). In impulsive approximation the shock occurs on such a short time scale that the internal dynamics of the satellite are assumed to be frozen in time. Consider a satellite on a polar orbit with velocity $v_\perp$ plunging perpendicularly into the disc (Fig. 1g). Using cylindrical coordinates, let $\mathcal{Z}$ denote the coordinate orthogonal to the disc plane. In tidal tensor approximation (keeping only the largest component), the net change of vertical (internal) velocity v_z of a particle in the satellite after passing the disc equals:

$$\Delta v_z = -\int_{t_1}^{t_2} \frac{\partial^2\Phi}{\partial\mathcal{Z}^2}\, z\, \mathrm{d}t = -\frac{z}{v_\perp}\int_{-\mathcal{Z}}^{\mathcal{Z}} \frac{\partial^2\Phi}{\partial\mathcal{Z}^2}\, \mathrm{d}\mathcal{Z} \approx \frac{2z}{v_\perp}\left|\frac{\partial\Phi}{\partial\mathcal{Z}}\right|_{\mathcal{Z}} \ , \tag{1.13}$$

where $z = \mathrm{const}$ during the tidal shock. In this impulsive approximation, the average energy gain for a particle at vertical distance z to the satellite centre then becomes $\langle\Delta E\rangle_\mathrm{imp} = \langle v_z\Delta v_z\rangle + \langle\Delta v_z^2\rangle/2 \approx \langle\Delta v_z^2\rangle/2$, as $\langle\Delta v_z\rangle = 0$ (see S87 chapter 5.2). If this energy gain is sufficiently large, the particle can escape the satellite through the Lagrange points L_1 or L_2.

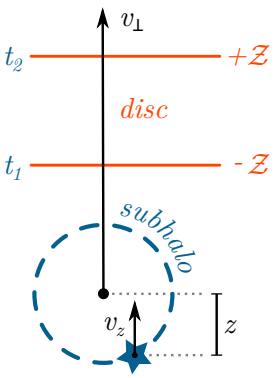

Fig. 1g: *Disc shocking: a subhalo moving through the disc experiences a strong tidal field for a brief interval in time.*

1.3.4 Adiabatic regime

This section follows closely the derivation in S87 chapter 5.2. Some simple applications of adiabatic invariants can also be found in BT87 chapter 3.6.

Not all particles in a subhalo react in the same way to tidal perturbations: for a subhalo particle with an (internal) orbital period τ that is much shorter than the time scale $\mathcal{T}$ of the tidal interaction, the net energy gain due to the perturbation may be negligible. If the tidal force is *turned on and off slowly* relative to the (internal) orbital period τ, the perturbation is said to be *adiabatic*. Quantities that do not change significantly after an adiabatic perturbation are named adiabatic invariants. For the case of a perturbed simple harmonic oscillator, the energy integral E is such an invariant. To gain some intuition, this is shown following the basic one-dimensional example given in S87 chapter 5.2.

Consider a particle in a subhalo with harmonic potential $\Phi_{\rm sub} \propto r^2$, experiencing a disc shock as introduced in the previous subsection. The unperturbed equation of motion of a particle reads $\mathrm{d}z^2/\mathrm{d}t^2 + \omega^2 z = 0$, where z is its distance to the subhalo centre and $\omega = 2\pi/\tau$ its orbital frequency within the subhalo. S87 proposes to write the perturbed equation of motion in the form

$$\frac{\mathrm{d}^2 z}{\mathrm{d}t^2} + \omega^2 z \;=\; \underbrace{-\frac{\partial^2 \Phi}{\partial \mathcal{Z}^2}\, z}_{\text{tidal force}} \;=\; \underbrace{-\,4\pi G \rho_d(\mathcal{Z})}_{\text{Poisson}}\; z \;=\; \lambda \omega z F(t), \tag{1.14}$$

where λ is dimensionless and $F(t)$ determines the time dependence of the perturbation. Then, expanding up to second order $z = z_0 + \lambda z_1 + \lambda^2 z_2 + \mathcal{O}(\lambda^3)$ with $z_n = A_n(t)\cos\omega t + B_n(t)\sin\omega t$, the average energy gain $\langle \Delta E \rangle$ for particles with mean square (distance) deviation $\langle z^2 \rangle$ can be computed as averages of trigonometric functions (S87, eq. 5-18 – 5-22). Assuming a Gaussian vertical disc density profile $\rho_d(z)$ with scale length $\mathcal{Z}$, the time dependence becomes $F(t) = v_\perp \pi^{-1/2} \mathcal{Z}^{-1} \exp(-v_\perp^2 t^2/\mathcal{Z}^2)$: the perturbation is slowly being *turned on and off* as $F(t) \to 0$ for $t \to \pm\infty$. From there, $\lambda = -g/(\omega v_\perp)$ with $g = 8\pi^{3/2} G \rho_d(0) \mathcal{Z}$, which has dimensions of a force. In this notation,

$$\langle \Delta E \rangle \approx \frac{\langle z^2 \rangle\, g^2}{v_\perp^2}\; \exp\left(-\frac{\mathcal{T}^2}{2\,\tau^2}\right) \text{, i.e.} \tag{1.15}$$

the average energy gain after tidal perturbation decreases exponentially with the ratio of tidal interaction time scale $\mathcal{T}$ and (internal) orbital period $\tau = 2\pi/\omega$. This is referred to as adiabatic response: after the tidal interaction ends, there is an arbitrarily small energy gain for particles with $\tau \ll \mathcal{T}$. Such particles will therefore be rather reluctant to be tidally stripped from the satellite. A detailed study of adiabatic response to tidal perturbations is given in the series Weinberg (1994a,b,c), which also discusses how orbital resonances weaken the adiabatic protection provided by small internal periods τ. In chapter 2 of this thesis, adiabatic response of the inner regions of cuspy DM subhaloes will be used to argue in favour of their resilience to be fully disrupted by tides.

1.4 Collisionless dynamics

The following section introduces the concept of collisionless dynamics, which is the framework in which the tidal evolution of dwarf galaxies and subhaloes will be studied in this thesis.

The derivation up to equation 1.18 follows the steps outlined in BT87 chapter 4. A more detailed derivation, avoiding the straight-line approximation used here, can be found in S87 chapter 2.1. See also Power et al. (2003) for a discussion on conditions for convergence of numerical simulations in the context of two-body relaxation.

Consider a DM subhalo, consisting of N smaller clumps of DM. These clumps could be the smallest collapsed structures formed by WIMPs or other DM particles, or potentially primordial black holes. A clump within the subhalo will feel the combined (smooth) force of all other clumps as well as single kicks due to gravitational encounters with nearby substructures. Which of these two forces will be the dominant one in determining the orbit of the clump? Answering this question has a very practical motivation: modelling kicks by nearby substructures is computationally expensive, neglecting them would (and will!) simplify all future calculations in this thesis. The goal of the following order of magnitude estimate is to determine the smallest subhalo mass for which the assumption of *collisionless* evolution, i.e. evolution governed by the smooth net force, holds.

In point mass approximation, a dark matter clump, moving with velocity v along a straight line and passing another clump at a distance b (Fig. 1h) experiences a velocity change in the direction perpendicular to its motion of

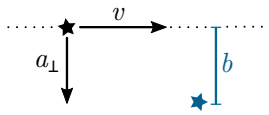

Fig. 1h: *Gravitational encounter between two point masses with relative velocity v and impact parameter b.*

$$\Delta v_\perp = \int_{-\infty}^{+\infty} a_\perp \mathrm{d}t = \int_{-\infty}^{+\infty} \frac{G\,m\,b}{(b^2+v^2t^2)^{3/2}}\,\mathrm{d}t = \frac{2Gm}{bv}\ . \tag{1.16}$$

Assuming a random distribution of DM clumps along the orbit, positive and negative contributions of $\Delta v_\perp$ cancel on average, but similar to a random walk, the square deviation $\langle \Delta v_\perp^2 \rangle$ increases with time. Integrating equation 1.16 over a range of impact parameters between $b_{\min}$ and $b_{\max}$ for one orbit, setting $v^2 = GNm/R$, one finds $\langle \Delta v_\perp^2 \rangle / v^2 = 8 \ln \Lambda \,/N$ where $\Lambda = b_{\max}/b_{\min}$. There is no satisfying answer on how to compute $b_{\min}$ and $b_{\max}$ for point masses, however for this order of magnitude estimate, the following approximations shall suffice: for $b_{\max}$ we choose the subhalo radius R, and for $b_{\min}$ the separation below which the two masses with relative velocity v would become gravitationally bound, $b_{\min} \approx Gm/v^2$, which conveniently yields $\Lambda \approx N$. Over a number of n_{relax} orbits, $\langle \Delta v_\perp^2 \rangle$ reaches a value of the same order as v^2, so

$$n_{\mathrm{relax}} \approx \frac{N}{8 \ln N}\ . \tag{1.17}$$

This happens over a time interval of

$$t_{\mathrm{relax}} \approx n_{\mathrm{relax}}\ t_{\mathrm{cross}}\ , \tag{1.18}$$

where $t_{\mathrm{cross}} = R/v$. One can now confront t_{relax} against the age of the universe: if t_{relax} results larger than said age, approximating the dynamics of the subhalo as collisionless is justified. For an analytical approximation, expanding the logarithm of equation 1.17

around a number of $N_0 = 10^{10}$ of clumps gives $n_{\rm relax} \approx cN^{\lambda}$, with $\lambda = 1 - 1/\ln N_0$ and $c = \exp(1)/(8 \ln N_0)$. Using an order-of-magnitude mass-size relation for subhaloes, $R/\mathrm{kpc} \approx [M/(10^8\,\mathrm{M}_\odot)]^{0.4}$ (see Eq. 1.5 for the functional form and Fig. 4.6 for numerical values), in combination with the constraint that $t_{\rm relax} \gtrsim 10^1$ Gyrs, one finds:

$$M/\mathrm{M}_\odot \gtrsim 10^4 \times (m/\mathrm{M}_\odot)^{0.9} \quad . \tag{1.19}$$

If DM consists of WIMPS (at particle masses of $\sim 100\,\mathrm{Gev/c^2}$), the smallest clumps it forms are of earth-mass, $m = 10^{-6}\,\mathrm{M}_\odot$, and subhaloes with masses larger than $M \gtrsim 10^{-2}\,\mathrm{M}_\odot$ can be approximated as collisionless systems. If DM consists of primordial black holes, larger clump masses are possible: if $m = 1\,\mathrm{M}_\odot$, the mass for collisionless subhaloes increases to $M \gtrsim 10^4\,\mathrm{M}_\odot$.

All calculations carried out in this thesis treat DM subhaloes as collisionless systems. When applying the results to systems with masses smaller than the threshold estimated by equation 1.19, caution needs to be taken to ensure that the system is substantially younger than the age of the universe, so that the summed effect of close encounters is still negligible.

1.4.1 Collisionless Boltzmann Equation

This summary follows BT87 chapters 4.1 and 4.4.

The following three subsections briefly summarize conditions and properties of equilibrium configurations for collisionless systems with the aim to introduce the notation and terminology used throughout the thesis. This subsection in specific discusses constraints on the flow of particles in phase space which will be used at a later stage for the generation of equilibrium N-body models. As the motion of particles in collisionless systems is governed by the underlying mean gravitational potential, this discussion holds both for the case of massless tracer particles and those particles which source the underlying potential. Whenever distinction is necessary, $\nu(r)$ denotes the tracer (number) density, and $\rho(\vec{r})$ denotes mass density which sources the potential $\Phi(\vec{r})$.

The position and velocity of a particle determine its state vector $\vec{\Omega}(t) = [\vec{r}(t), \vec{v}(t)]$ in phase space. The number of particles per phase space volume element $\mathrm{d}\Omega = \mathrm{d}^3\vec{r}\,\mathrm{d}^3\vec{v}$ is referred to as the distribution function (hereafter short DF) of the system,

$$f(\vec{r}, \vec{v}, t) = \left.\frac{\mathrm{d}N}{\mathrm{d}\Omega}\right|_{\vec{r},\vec{v},t} \quad . \tag{1.20}$$

All structural and kinematic properties of a system of particles can be obtained from its DF. As an example, the number density in configuration space can be obtained by integrating the DF over all velocities, $\nu(\vec{r}, t) = \int f(\vec{r}, \vec{v}, t)\,\mathrm{d}^3\vec{v}$. Similarly, the mean square velocity of particles at position $\vec{r}$ can be computed as $\overline{v^2}(\vec{r}, t) = \int f(\vec{r}, \vec{v}, t)\,\vec{v}\cdot\vec{v}\,\mathrm{d}^3\vec{v}/\nu(\vec{r}, t)$.

As particles (be it stars in the potential of a dwarf galaxy, or dark matter clumps forming a subhalo) do move smoothly, i.e. without discontinuous jumps, both in

position and in velocity, one may write the flow of particles in phase space akin to the spatial flow of particles in fluid dynamics, governed by the continuity equation:

$$\frac{\partial \rho}{\partial t} + \vec{\nabla} \cdot (\rho \vec{v}) = 0 \ . \tag{1.21}$$

In the same way, the flow of particles with density $f(\vec{r}, \vec{v}, t)$ in phase space reads

$$\frac{\partial f}{\partial t} + \vec{\nabla} \cdot (f \vec{v}) + \frac{\partial}{\partial \vec{v}} \cdot (f \vec{a}) = 0 \quad \text{where} \quad \vec{a} = -\vec{\nabla}\Phi \ . \tag{1.22}$$

We denote the gradient by $\vec{\nabla} = (\partial/\partial x, \partial/\partial y, \partial/\partial z)^\intercal$, and write symbolically for velocity derivatives $\partial/\partial \vec{v} = (\partial/\partial v_x, \partial/\partial v_y, \partial/\partial v_z)^\intercal$.

Writing the divergence terms explicitly and noting that $\vec{\nabla} \cdot \vec{v} = 0$ as $\vec{x}$ and $\vec{v}$ are independent coordinates in phase space, and $(\partial/\partial \vec{v}) \cdot (-\vec{\nabla}\Phi) = 0$ as $\Phi(\vec{r})$ does not depend on velocities, one obtains the collisionless Boltzmann equation (CBE)

$$\frac{\partial f}{\partial t} + \vec{v} \cdot \vec{\nabla} f - \vec{\nabla}\Phi \cdot \frac{\partial f}{\partial \vec{v}} = 0 \ . \tag{1.23}$$

Functions $f(\vec{r}, \vec{v}, t)$ that are solutions to the CBE are physically possible DF for collisionless gravitating systems. For steady state configurations, we need $\partial f/\partial t = 0$. Interestingly, this condition is identical to requiring that the DF is a function of the phase space coordinates only through integrals of motion: $f(\vec{r}, \vec{v}) = f(E(\vec{r}, \vec{v}))$, where along each orbit

$$\frac{\mathrm{d}}{\mathrm{d}t} E\big(\vec{r}(t), \vec{v}(t)\big) = 0 \ . \tag{1.24}$$

Inserting the above expression in the equations of motion,

$$\begin{cases} \mathrm{d}\vec{r}/\mathrm{d}t = \vec{v} \\ \mathrm{d}\vec{v}/\mathrm{d}t = -\vec{\nabla}\Phi(\vec{r}) \end{cases} \tag{1.25}$$

one obtains

$$\vec{v} \cdot \vec{\nabla} E - \vec{\nabla}\Phi \cdot \frac{\partial E}{\partial \vec{v}} = 0 \ , \tag{1.26}$$

formally identical to the CBE for the steady state case $\partial f/\partial t = 0$. In this thesis, all distribution functions $f(E)$ of equilibrium N-body models are functions of the energy integral $E(\vec{r}, \vec{v})$ only.

1.4.2 Jeans equations

This section covers the Jeans equation for spherical, dispersion-supported systems, following BT87 chapter 4.2.

The Jeans equations relate the velocity moments σ_{jk}^2 of an equilibrium collisionless system to its spatial coordinates $\vec{r}$. This is particularly handy for collisionless systems containing an observable (e.g. stellar) tracer population, as it allows some constraints on properties of the system which are not directly accessible to observation such as the potential. The Jeans equations are obtained by multiplying the collisionless Boltzmann

equation by a velocity component v_j and subsequently integrating over all velocities $\vec{v}$, assuming a system for which the DF satisfies $f(\vec{r},\vec{v}) \to 0$ separately for $r \to \infty$ (i.e. the system is spatially finite) and $v \to \infty$ (i.e. particles have finite velocities).

In the following, we only consider spherical, dispersion supported (non-rotating) systems with $\overline{v_\theta^2} = \overline{v_\phi^2}$, where $\{r,\theta,\phi\}$ are spherical (non-projected) coordinates, and the average of the squared velocity components v_i^2 of all particles located at radius r is denoted by $\overline{v_i^2}$. In this notation, introducing the velocity anisotropy function

The velocity dispersion is isotropic at radii r where $\beta(r) = 0$, radially biased for $\beta(r) > 0$ ($\beta = 1$ for purely radial orbits), and tangentially biased at radii where $\beta(r) < 0$.

$$\beta(r) = 1 - \frac{\overline{v_\theta^2} + \overline{v_\phi^2}}{2\overline{v_r^2}} \ , \tag{1.27}$$

the Jeans equation reads

$$\frac{1}{\nu}\frac{\mathrm{d}(\nu v_r^2)}{\mathrm{d}r} + \frac{2\beta(r)\overline{v_r^2}}{r} = -\frac{\mathrm{d}\Phi}{\mathrm{d}r} \ . \tag{1.28}$$

This equation may be rewritten in a way that relates the mass enclosed within a spherical radius r to the radial velocity dispersion $\overline{v_r^2}(r)$, the tracer density $\nu(r)$ and the velocity anisotropy $\beta(r)$:

$$M(<r) = -\frac{r\,\overline{v_r^2}}{G}\left(\frac{\mathrm{d}\ln\nu}{\mathrm{d}\ln r} + \frac{\mathrm{d}\ln\overline{v_r^2}}{\mathrm{d}\ln r} + 2\beta(r)\right) \ . \tag{1.29}$$

The above equation gives rise to the infamous mass-anisotropy degeneracy, as the mass enclosed within a radius r is dependent on the (generally unknown) velocity anisotropy function $\beta(r)$.

1.4.3 Virial theorem

While this section generally follows BT87 chapter 4.3, the notation has been adapted to allow to distinguish between the (stellar) tracer density, and the (dark matter) mass density sourcing the potential.

The virial theorem relates averages of kinetic and potential energy of a collisionless system. It will be used in this thesis to ascertain whether a subhalo is in dynamical equilibrium, and for dynamical estimates of enclosed masses in dwarf galaxies. The theorem can be derived by multiplying the collisionless Boltzmann equation by both a velocity component v_j and a position component r_k and subsequently integrating over all velocities and positions. The resulting equation is the tensor virial theorem:

$$2\underbrace{K_{jk}}_{\text{kinetic}} + \underbrace{W_{jk}}_{\text{potential}} = \frac{1}{2}\frac{\mathrm{d}^2}{\mathrm{d}t^2}\underbrace{I_{jk}}_{\text{inertia}} \ . \tag{1.30}$$

For dispersion supported systems without ordered motion (all velocity components average to $\overline{v_j} = 0$), equation 1.30 relates the kinetic energy tensor

$$K_{jk} = \frac{1}{2}\int \nu(\vec{r})\,\sigma_{jk}^2\,\mathrm{d}^3\vec{r} \quad \text{where} \quad \sigma_{jk}^2 = \overline{v_j v_k} \ , \tag{1.31}$$

to the potential energy tensor

$$W_{jk} = -\int \nu(\vec{r}) x_j \frac{\partial \Phi(\vec{r})}{\partial x_k} \, \mathrm{d}^3\vec{r} \tag{1.32}$$

and the time derivative of the moment of inertia tensor

$$I_{jk} = \int \nu(\vec{r}) \, r_j r_k \, \mathrm{d}^3\vec{r} \; . \tag{1.33}$$

For a system in steady state, $\mathrm{d}^2 I_{jk}/\mathrm{d}t^2 = 0$ for all j, k. Denoting the trace of the kinetic energy tensor by $\sum_j K_{jj} = K$ and similarly the trace of the potential energy tensor by $\sum_j W_{jj} = W$, one obtains the scalar virial theorem:

$$2K + W = 0 \; . \tag{1.34}$$

For spherical systems, W_{jk} is diagonal, and the components are equal to one another, $W_{jj} = W/3$ for all j. As a consequence, in steady state, also K_{jk} must be diagonal, and $2K_{jj} + W_{jj} = 0$. If we now choose a co-ordinate system so that the j-axis coincides with our line-of-sight, then $2K_{\mathrm{los}} + W_{\mathrm{los}} = 0$, which forms the basis of chapter 4 of this thesis.

1.5 Numerical setup

Lacking a general theory for the orbital motion resulting from the gravitational interaction of $N > 2$ particles, in this thesis, the equations of motion of N interacting particles are solved numerically. The direct summation of forces involves a sum over $N-1$ particles for each of the N particles and consequently scales as $\mathcal{O}(N^2)$. For subhaloes that behave like collisionless systems, i.e. systems where the motion of particles is governed by the smooth net potential, the use of an approximative force calculation is well motivated. The particle mesh method, applied in the simulations of chapters 2, 3 and 4 to compute net gravitational forces, is discussed in subsection 1.5.1, whereas subsection 1.5.2 briefly summarizes the integrator used to solve the resulting equations of motion. The models adopted for the host galaxy potential and for subhalo density profiles are described in sections 1.5.3 and 1.5.4.

1.5.1 Particle mesh codes

The gravitational potential $\Phi(\vec{r})$ is sourced by the matter density $\rho(\vec{r})$ as descried by the Poisson equation,

$$\nabla^2 \Phi\left(\vec{r}\right) = 4\pi G \rho\left(\vec{r}\right) \ . \tag{1.35}$$

If L is a linear differential operator and $Lf(x)=g(x)$, the Green's function $H(x)$ satisfies $LH(x)=\delta(x)$. The solution then reads $f(x) = H(x) * g(x)$, with $*$ denoting a convolution.

The general solution to this partial differential equation may be written as a convolution:

$$\Phi\left(\vec{r}\right) = 4\pi G \ H\left(\vec{r}\right) * \rho\left(\vec{r}\right) \tag{1.36}$$

denoting by H the Green's function

$$H\left(\vec{r}\right) = -\frac{1}{4\pi r} \quad \text{where} \quad r = |\vec{r}| \ . \tag{1.37}$$

The discussion of solving the Poisson equation on a density grid as well as the numerical differentiation of the potential follows closely the steps outlined in Fellhauer et al. (2000). A general discussion of the particle mesh method can be found in HE88 chapter 5.

The particle mesh method involves sampling the matter density $\rho(\vec{r})$ discretely on a three-dimensional grid, and solving the Poisson equation for this discrete density grid. For the density grid, equation 1.36 becomes

$$\Phi_{\vec{j}} = 4\pi G \sum_{\vec{k}} H_{\vec{k}-\vec{j}} \ \rho_{\vec{k}} \tag{1.38}$$

where $\vec{k} = (k_1, k_2, k_3)^\intercal$, $k_i \in \{1, \ldots, n\}$ identifies the position of a cell, denoting by n the number of grid cells per dimension. The Green's function for the grid reads

$$H_{\vec{k},\vec{k}\neq\vec{0}} = -\frac{1}{4\pi k} \quad \text{where} \quad k = |\vec{k}| \ . \tag{1.39}$$

The value of $H_{\vec{0}}$ determines the potential sourced by particles within the same cell. The computationally expensive part in the determination of $\Phi_{\vec{j}}$ is the (discrete) convolution in equation 1.38: computing $\Phi_{\vec{j}}$ for all $\mathcal{N} = n^3$ grid cells of the density grid requires

$\mathcal{O}(\mathcal{N}^2)$ summations. In Fourier space however, the convolution reduces to a simple multiplication,

$$\hat{\Phi}_{\vec{k}} = 4\pi G \; \hat{H}_{\vec{k}} \; \hat{\rho}_{\vec{k}} \; . \tag{1.40}$$

The Fast Fourier Transform (FFT) algorithm allows to transform to Fourier space scaling with $\mathcal{O}(\mathcal{N} \ln \mathcal{N})$ (see HE88, chapter A-1-3), which for large $\mathcal{N}$ brings a convenient reduction in necessary computations compared to the $\mathcal{O}(\mathcal{N}^2)$ convolution in configuration space. The potential transformed back from Fourier space to configuration space reads

$$\Phi_{\vec{j}} = \frac{4\pi G}{n^3} \sum_{\vec{k}} \hat{H}_{\vec{k}} \; \hat{\rho}_{\vec{k}} \; \exp\left(\frac{2\pi i}{n} \; \vec{k} \cdot \vec{j}\right) \; , \tag{1.41}$$

where only the density grid $\rho_{\vec{k}}$ needs to be updated each time step as the spacing of the Fourier and configuration space grids remains constant, and so does $\hat{H}_{\vec{k}}$. In the simulations of chapters 2 and 3, the particle mesh code SUPERBOX (Fellhauer et al., 2000) is used. This code employs three grids to resolve the particle density, each of width x_i and spatial resolution $\Delta x = x_i/n$ per dimension. The two grids of highest resolution (of width $x_1 < x_2$) are co-moving with the satellite, centred on its densest region, whereas the lowest-resolving grid (of width x_3) is fixed in space. This is shown schematically in figure 1.5.

The accelerations on each particle are computed from the grid potential by numerically differentiating to quadratic order in Δx, taking into account the displacement $\vec{\epsilon}$ of a particle from the grid centre. Only directly adjacent grid cells are used for the numerical differentiation. In one dimension (i.e. omitting mixed terms for simplicity), the acceleration at a distance ϵ to the cell centre reads (Fellhauer et al., 2000, section

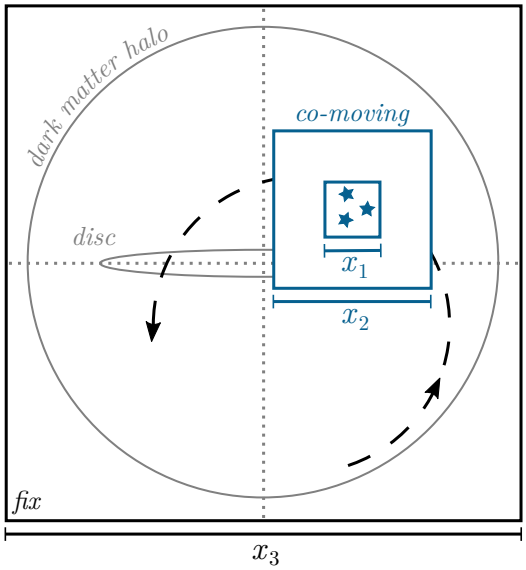

Figure 1.5: The particle mesh code SUPERBOX (Fellhauer et al., 2000) uses three grids to map the density of N-body particles. The two highest resolving grids (x_1, x_2) are co-moving with the satellite, whereas the lowest-resolving grid (x_3) is fixed in space.

2.2):

$$a_x(x+\epsilon) \approx -\left.\frac{\partial\Phi}{\partial x}\right|_x - \left.\frac{\partial^2\Phi}{\partial x^2}\right|_x \epsilon \tag{1.42}$$

$$\approx -\frac{\Phi_{j+1}-\Phi_{j-1}}{2\Delta x} - \frac{\Phi_{j+1}+\Phi_{j-1}-2\Phi_j}{(\Delta x)^2}\,\epsilon\ . \tag{1.43}$$

This interpolation methods resembles a Nearest Grid Point (NGP) scheme as it only involves evaluations of Φ at adjacent grid cells, but differs from the classical NGP approach in considering the displacement ϵ of a particle within the box by differentiating to quadratic order in Δx.

1.5.2 Leapfrog integration

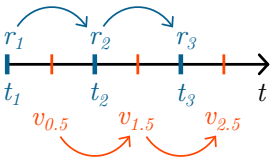

Fig. 1i: *Leapfrog scheme: positions r and velocities v are updated iteratively, offset by half a step.*

Once potential and accelerations are determined using the particle mesh method and subsequent numerical differentiation, the equations of motion for each particle (see equation 1.25) can be solved numerically. The code SUPERBOX uses Leapfrog integration for this purpose, where velocities and positions are updated iteratively (Fig. 1i):

$$\begin{cases} \vec{v}(t+\Delta t/2) = \vec{v}(t-\Delta t/2) + \vec{a}(t)\ \Delta t \\ \quad \vec{r}(t+\Delta t) = \vec{r}(t) + \vec{v}(t+\Delta t/2)\ \Delta t \quad . \end{cases} \tag{1.44}$$

Note that while the Leapfrog method generally conserves the total energy of a gravitating system, this does not hold when using numerically approximated potentials as obtained using the particle mesh method.

1.5.3 Host galaxy model

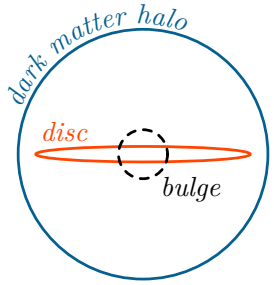

Fig. 1j: *Three-component model of the host potential.*

The host galaxy potential in the numerical simulations of chapters 2, 3 and 4 is an analytical model consisting of three main components: a spherical bulge, an axisymmetric galactic disc, and a spherical DM halo (Fig. 1j). While the specific parameters and implementations will be detailed in each chapter, to set the stage, the general properties will be discussed in the following.

Bulge. The bulge is modelled as a spherical Hernquist (1990) potential with scale radius a_b and total mass M_b:

$$\Phi_{\rm bulge}(r) = -\frac{GM_b}{r+a_b}\ . \tag{1.45}$$

Disc. The disc is an axisymmetric Miyamoto & Nagai (1975) potential with radial scale length a_d, vertical scale height b_d and total mass M_d:

$$\Phi_{\rm disc}(R,z) = -GM_d\left[R^2 + (a_d + \sqrt{b_d^2+z^2})^2\right]^{-1/2}\ . \tag{1.46}$$

In chapter 2 thick and thin disc are modelled separately, whereas in chapter 3 only one disc component is included in the simulation.

Halo. The dark matter halo is modelled as a Navarro et al. (1997) profile with scale mass M_s and scale radius r_s. The potential reads:

$$\Phi_{\rm halo}(r) = -\frac{GM_s}{r}\ \frac{1}{\ln(2)-\frac{1}{2}}\ \ln\left(1+\frac{r}{r_s}\right)\ . \tag{1.47}$$

Consequently the total host potential becomes

$$\Phi_{\rm host}(R,z) = \Phi_{\rm bulge}(r) + \Phi_{\rm disc}(R,z) + \Phi_{\rm halo}(r)\ . \tag{1.48}$$

Figure 1.6 shows the resulting rotation curve $v_{\rm c} = (-r\partial\Phi_{\rm host}/\partial r)^{1/2}$ at redshift $z = 0$ in the plane of the galactic disc, using the parameters of chapter 2 and summing $\Phi_{\rm disc} = \Phi_{\rm disc,thin} + \Phi_{\rm disc,thick}$.

The evolution of the host galaxy components with redshift z is modelled using the Buist & Helmi (2014) recipe where for the halo

$$M_s(z) \ \propto\ \exp(-2a_g z) \quad \text{and} \tag{1.49}$$

$$r_s(z) \ \propto\ \exp(-2a_g z/\gamma_g) \quad . \tag{1.50}$$

In the above equations, γ_g and a_g are constants regulating the halo growth rate. The numerical values for these parameters are listed with the specific implementations in each chapter.

Cosmology. The cosmology adopted in this thesis assumes a flat ΛCDM universe with the Planck cosmological parameters (Planck Collaboration et al., 2018) for models of chapter 2, and the parameters used in the Aquarius simulations (Springel et al., 2008) for the models of chapters 3 and 4. Figure 1.7 shows the redshift - time relation for these cosmological models together with the relevant cosmological parameters. Note that the simulations described in this thesis cover scales smaller than 1 Mpc, where the dynamics are governed by the local gravitational potential of the Milky Way and are decoupled from the Hubble flow. The simulations therefore do not explicitly model cosmic expansion – however, the initial conditions of accreted substructures and the evolution of the Milky Way potential are taken from full cosmological simulations, as described in chapter 3.

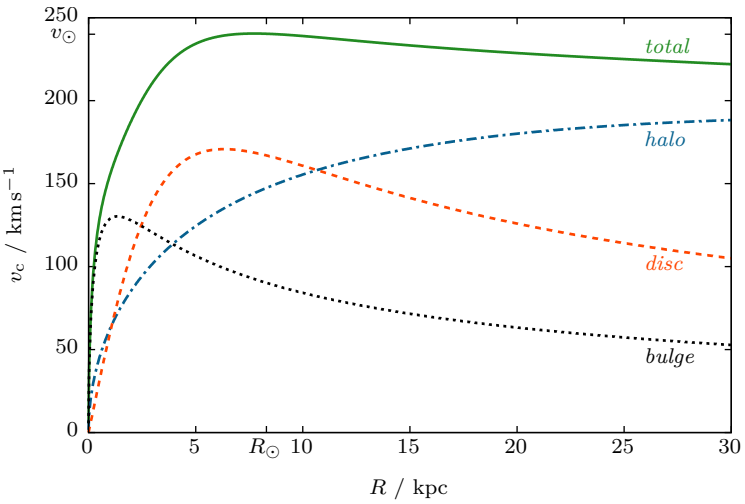

Figure 1.6: Rotation curve $v_c = (-r\partial\Phi_{host}/\partial r)^{1/2}$ of the Milky Way-like galaxy model consisting of a Hernquist (1990) bulge, a Miyamoto & Nagai (1975) disc and a Navarro et al. (1997) dark matter halo. The rotation curve is plotted as a function of the cylindrical radius R within the disc plane at redshift $z = 0$. The parameters for this plot correspond to the simulations of chapter 2, summing $\Phi_{disc} = \Phi_{disc,thin} + \Phi_{disc,thck}$.

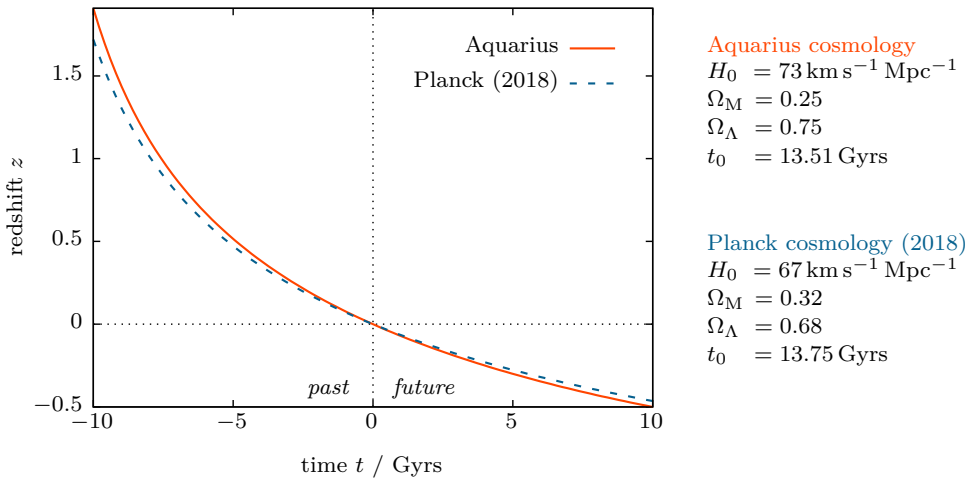

Figure 1.7: Redshift z as a function of time t, where $t = 0$ corresponds to the present and $t > 0$ lie in the future. The parameters H_0, Ω_M, Ω_Λ, and t_0 denote the present Hubble parameter, mass density parameter, dark energy density parameter, and the age of the universe, respectively. The relation is shown for the Planck cosmological parameters (Planck Collaboration et al., 2018), adopted in chapter 2, as well as for the parameters used in the Aquarius simulation (Springel et al., 2008), adopted in chapters 3 and 4.

1.5.4 Subhalo model

Subhaloes in the tidal field of the host halo have an outer density slope $\beta = -\partial \ln \rho / \partial \ln r$ ($r \to \infty$) that is steeper than the NFW slope of $\beta = 3$ (see Peñarrubia et al., 2010). Furthermore, chapters 3 and 4 focus on the distinct evolution of subhaloes with cuspy and cored density profiles. This requires a flexible parametrization of the density profile. Subhaloes in chapter 3 are modelled as generalised Hernquist profiles with core size r_c,

$$\rho(r) = \frac{\rho_s \, r_s^4}{(r + r_c)\,(r + r_s)^3} \ , \tag{1.51}$$

whereas tidally stripped subhaloes are approximated in chapter 4 using a profile with outer slope $\beta = 5$ and variable inner slope $\gamma = -\partial \ln \rho / \partial \ln r$ ($r \to 0$),

$$\rho(r) = \frac{\rho_s \, r_s^5}{r^\gamma \, (1 + r)^{5-\gamma}} \qquad \text{(i.e. } \{\alpha, \beta, \gamma\} = \{1, 5, \gamma\} \text{ in Eq. 2.1).} \tag{1.52}$$

Figure 1.8 shows these two profiles for different choices of the parameters r_c and γ. Section 2.3.1 details the generation of equilibrium N-body models from a given density profile, and section 2.5 describes the distribution-function based approach used in this thesis to model stellar populations embedded in DM subhaloes.

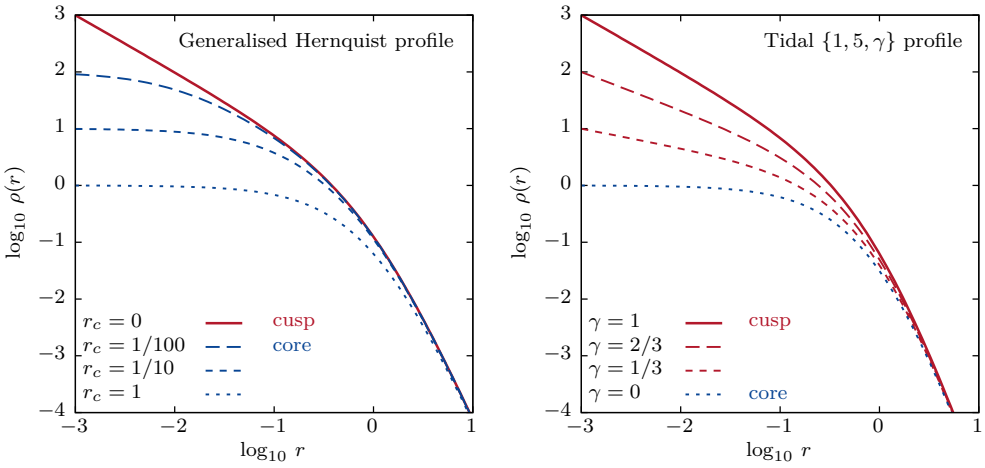

Figure 1.8: Density profiles for subhaloes. The left panel shows a generalised Hernquist profile (equation 1.51 with $\rho_s = 1, r_s = 1$) that allows for density cores of size r_c as used in chapter 3. For $r_c = 0$ this profile is identical to the classical (cuspy) Hernquist profile. The right panel shows the density profile of equation 1.52 (with $\rho_s = 1, r_s = 1$) for different values of the parameter γ, determining the inner density slope $\gamma = -\partial \ln \rho / \partial \ln r$ ($r \to 0$). Models with $\gamma > 0$ are cuspy. This profile is used in chapter 4 to model tidally stripped subhaloes.

Chapter 2

Tidal survival of substructures

Abstract

The clumpiness of dark matter on sub-kpc scales is highly sensitive to the tidal evolution and survival of subhaloes. In agreement with previous studies, we show that N-body realisations of cold dark matter subhaloes with centrally-divergent density cusps form artificial constant-density cores on the scale of the resolution limit of the simulation. These density cores drive the artificial tidal disruption of subhaloes. We run controlled simulations of the tidal evolution of a single subhalo where we repeatedly reconstruct the density cusp, preventing artificial disruption. This allows us to follow the evolution of the subhalo for arbitrarily large fractions of tidally stripped mass. Based on this numerical evidence in combination with simple dynamical arguments, we argue that cuspy dark matter subhaloes cannot be completely disrupted by smooth tidal fields. Modelling stars as collisionless tracers of the underlying potential, we furthermore study the tidal evolution of Milky Way dwarf spheroidal galaxies. Using a model of the Tucana III dwarf as an example, we show that tides can strip dwarf galaxies down to sub-solar luminosities. The remnant *micro-galaxies* would appear as co-moving groups of metal-poor, low-mass stars of similar age, embedded in sub-kpc dark matter subhaloes.

This chapter has been submitted for publication in MNRAS (RE, J. Peñarrubia: Can tides disrupt cold dark matter subhaloes? arXiv:1906.01642). Figures 2.3, 2.4, 2.5, 2.9 and Appendix 2.A were added in the context of this thesis for clarity.

2.1 Introduction

The hierarchical clustering of dark matter (DM) is a remarkably successful framework to explain structure formation on large galactic scales. However on kpc scales and smaller, the clustering properties of DM are subject of controversy and debate. It is on these scales that potential DM particle properties (e.g. Tremaine & Gunn, 1979; Vogelsberger et al., 2012) as well as baryonic effects (e.g. Navarro et al., 1996; Pontzen & Governato, 2012; Read et al., 2016) leave their imprints on the DM distribution. While DM-only cosmological simulations predict a universal density profile with a cusp of central slope $\gamma = -\mathrm{d}\ln\rho/\mathrm{d}\ln r = 1$ (Navarro et al., 1997), kinematic studies of stars in DM dominated Milky Way dwarf galaxies did not yield conclusive evidence whether potential underlying DM profiles have centrally-divergent density cusps (e.g. Richardson & Fairbairn, 2014), or constant-density cores (e.g. Walker & Peñarrubia,

2011; Amorisco et al., 2013), see chapter 1.2.1. The number of known Milky Way dwarf galaxies has increased dramatically over recent years, with deep photometric and spectroscopic surveys revealing subsequently fainter and less massive satellites (e.g. Drlica-Wagner et al., 2015; Koposov et al., 2015; Torrealba et al., 2016). Nevertheless, their abundance can be matched to the vast number of subhaloes in cosmological simulations only by either facilitating the tidal disruption of subhaloes before redshift $z = 0$, or by suppressing star formation in low-mass subhaloes. This can be achieved by involving baryonic processes (see Bullock et al. 2000; Benson et al. 2002; more recently e.g. Chan et al. 2015; Schaye et al. 2015; Despali & Vegetti 2017), or DM recipes departing from the classical cold dark matter (CDM) model (e.g. Lovell et al., 2014). Several methods have been proposed in recent years to detect also subhaloes devoid of stars, indirectly through their effects on tidal streams (e.g. Ibata et al., 2002; Erkal & Belokurov, 2015), or more directly through strong gravitational lensing (e.g. Vegetti & Koopmans, 2009) – though clear signatures of such dark subhaloes are yet to be discovered.

The presence of self-bound subhaloes within larger DM haloes as relics of their accretion history was noted as soon as cosmological simulations had sufficient resolution to probe the scales in question (resolving main haloes with $\sim 10^4$ particles, e.g. Tormen et al., 1997; Moore et al., 1998), see chapter 1.1. It was soon understood that insufficient resolution depletes subhaloes artificially (which was originally dubbed *overmerging*, e.g. Klypin et al., 1999a). Current DM-only simulations of Milky Way-like haloes resolve DM subhaloes of masses down to $\sim 10^5\,\mathrm{M}_\odot$ at an N-body particle mass of $10^3 - 10^4\,\mathrm{M}_\odot$ (resolving main haloes with $10^8 - 10^9$ particles, e.g. Springel et al., 2008; Griffen et al., 2016). Recent studies raise suspicion whether the predictions on abundance and structural parameters of subhaloes at these mass scales can be trusted: van den Bosch et al. (2018) argues that up to 80 per cent of subhaloes that disrupt in cosmological simulations do so because of numerical issues. This is also supported by the results of controlled simulations which suggest that DM subhaloes with centrally-divergent density cusps cannot be fully disrupted by tides (Kazantzidis et al., 2004; Goerdt et al., 2007; Peñarrubia et al., 2010; van den Bosch & Ogiya, 2018) – although also in these simulations, subhaloes do disrupt eventually due to limited resolution and finite particle number.

In this chapter, we study the tidal evolution of a single cuspy DM subhalo under the assumption that tides do not alter the central slope of $\gamma = 1$, as suggested by the results of controlled simulations (Hayashi et al., 2003; Peñarrubia et al., 2010). Our choice of $\gamma = 1$ is motivated by the Navarro et al. (1997) density profile for DM haloes. While other authors find slightly steeper (Diemand et al., 2008, for subhaloes) or slightly shallower slopes (e.g. Navarro et al., 2010; Ludlow et al., 2013), within the resolution limits, density profiles in DM-only simulations are cuspy, i.e. centrally-divergent. We follow the tidal evolution of our example cuspy subhalo in an evolving, analytical host potential, periodically reconstructing the density cusp. This cusp reconstruction

prevents artificial disruption and allows us to study the tidal evolution over arbitrarily large fractions of stripped mass.

The apparent *indestructibility* of cuspy subhaloes also has implications for dwarf galaxies embedded in such haloes: As an illustration, we follow the tidal evolution of a dwarf galaxy embedded in a cuspy DM halo using an N-body model tailored to match the ultra-faint Tucana III dwarf galaxy (Drlica-Wagner et al., 2015). We chose the Tuc III dwarf as an example as several of its measured structural and kinematic properties indicate strong past tidal interactions: Tuc III is on a very radial orbit with a pericentre distance of $\sim 3\,\mathrm{kpc}$, passing through the galactic disc, and has an associated stellar tidal stream (Li et al., 2018; Shipp et al., 2018). The luminosity $L \sim 10^3\,\mathrm{L}_\odot$ and line-of-sight velocity dispersion $\sigma < 1.5\,\mathrm{km\,s^{-1}}$ of the dwarf are particularly low (Simon et al., 2017), suggesting that Tuc III might be the remnant of a more massive and more luminous progenitor. In this work, we model the tidal stripping of Tuc III down to sub-solar luminosities: Interestingly, the remnant *micro-galaxy* would appear as a co-moving group of metal-poor stars of similar age, embedded in a sub-kpc DM halo.

The chapter is structured as follows: In section 2.2, we present simple dynamical arguments for the distinct tidal evolution and survival of DM substructures with density cusps and cores. Following the lead of van den Bosch et al. (2018), we show in section 2.3 how limited resolution in numerical simulations causes the artificial formation of density cores at the centres of DM subhaloes. Section 2.4 details our numerical experiments of the tidal evolution of a single subhalo, where we periodically reconstruct the density cusp. To model the evolution of Milky Way dwarf spheroidal galaxies, in section 2.5 we embed stars in a DM subhalo using a distribution function based approach and study the tidal stripping of dwarf galaxies down to sub-solar luminosities. In section 2.6 we summarize and discuss our findings in the context of detectability of low-mass subhaloes and highly stripped dwarf galaxies.

2.2 Tidal evolution of dynamical times

Consider a subhalo on an eccentric orbit of period T_orb within the main halo. Moving towards pericentre, tidal forces on the subhalo increase. *Under which conditions does a subhalo retain some fraction of bound particles after pericentre passage?* We address this question by contemplating the response of particles within the subhalo to the tidal field of the main halo. For this purpose, we compare the periods of circular orbits $t_\mathrm{c}(r)$ within cuspy and cored subhaloes, and study how $t_\mathrm{c}(r)$ evolves while the subhaloes structurally change due to tidal mass loss. We will show that for cuspy subhaloes, there is always a fraction of particles that react adiabatically to the tidal perturbation, and that this fraction increases during the tidal evolution of the subhalo.

We model the subhalo as a Dehnen (1993) profile with total mass M, scale radius a and scale density $\rho_s = (3-\gamma)M/4\pi a^3$, which can be written in terms of the general

$\{\alpha, \beta, \gamma\}$ profile,

$$\rho(r) = \rho_s \left(\frac{r}{a}\right)^{-\gamma} \left[1 + \left(\frac{r}{a}\right)^{\alpha}\right]^{(\gamma-\beta)/\alpha} , \tag{2.1}$$

with $\alpha = 1$, outer slope $\beta \equiv -\mathrm{d}\ln\rho/\mathrm{d}\ln r \ (r \to \infty) = 4$ and inner slope $\gamma \equiv -\mathrm{d}\ln\rho/\mathrm{d}\ln r \ (r \to 0)$. The period of a circular orbit of radius r then becomes

$$t_\mathrm{c}(r) = 2\pi \left[\frac{(r+a)^{3-\gamma}}{GM\, r^{-\gamma}}\right]^{1/2} . \tag{2.2}$$

Figure 2.1 shows $t_\mathrm{c}(r)$ for cuspy ($\gamma = 1$) and cored ($\gamma = 0$) subhaloes for an initial mass $M_0 = 10^8\,\mathrm{M}_\odot$ and initial scale radius $a_0 = 0.5\,\mathrm{kpc}$ (solid lines). For the cuspy model, as $r \to 0$, also $t_\mathrm{c}(r) \to 0$, i.e. there is always a subset of radii for which $t_\mathrm{c}(r) \ll T_\mathrm{orb}$. As the strongest tidal interaction happens on a timescale of some fraction of the orbital period T_orb, we can assume that for particles with $t_\mathrm{c}(r) \ll T_\mathrm{orb}$, the tidal interaction is perceived as a mere adiabatic perturbation. Furthermore, the same particles have $T_\mathrm{orb}/t_\mathrm{c} \gg 1$ revolutions within the subhalo to reach dynamical equilibrium before the next strong tidal interaction. On the other hand, for the cored model, $t_\mathrm{c}(r) \to \mathrm{const} > 0$ as $r \to 0$: inside the density core, all orbits have the same orbital period. Whether there is a subset of particles that react adiabatically to the perturbation depends on the specific values of $t_\mathrm{c}(r)$ and T_orb. Similarly, the number of revolutions $T_\mathrm{orb}/t_\mathrm{c}$ available to particles in cored subhaloes to relax before the next strong tidal interaction depends on the specific values of $t_\mathrm{c}(r)$ and T_orb.

How does $t_\mathrm{c}(r)$ evolve during tidal stripping? Subhalo mass M, scale radius a and the shape of the density profile $\rho(r)$ all evolve due to tidal mass loss. For simplicity, in the following discussion of orbital periods $t_\mathrm{c}(r)$ we will assume self-similar evolution of the subhalo density profile and only consider the change of subhalo mass M and scale radius a during tidal stripping. This assumption is well motivated for particles with $r \ll a$, as the central regions of subhaloes are shown to evolve in a self-similar manner in controlled simulations (Hayashi et al., 2003; Peñarrubia et al., 2010). We make use of tidal evolutionary tracks (originally introduced by Peñarrubia et al., 2008b) to parametrize the evolution of equilibrium halo structural parameters as a function of the fraction M/M_0 of remnant bound mass. In specific, we use the tracks discussed in chapter 4.A of this thesis for the evolution of the DM scale radius for cuspy and cored subhaloes. As shown with dashed (dotted) lines in Figure 2.1 for remnant bound masses of $M/M_0 = 1/10$ (1/50), at a fixed relative radius r/a, for cuspy models, the period $t_\mathrm{c}(r/a)$ decreases during tidal stripping[1]. Consequently, the region within the subhalo for which the tidal interaction is adiabatic increases during tidal evolution, and so does the number of revolutions $t_\mathrm{c}(r/a)$ available for the subhalo to reach dynamical equilibrium within the (constant) orbital period T_orb: this suggests that tides cannot fully disrupt cuspy subhaloes[2]. For cored models however, $t_\mathrm{c}(r/a)$ increases during tidal stripping at fixed r/a: the region that reacts adiabatically to tides shrinks, and

[1] *Note that while for cuspy subhaloes $t_\mathrm{c}(r/a)$ at a fixed fraction r/a of the instantaneous scale radius a decreases with tidal mass loss, $t_\mathrm{c}(r)$ at a fixed value of r increases. In the central regions of the cuspy subhalo however, $t_\mathrm{c}(r)$ is only weakly effected by tidal mass loss: Assuming self-similar evolution and using the tidal evolutionary tracks of appendix 4.A ($a \propto M^{0.48}$), equation 2.2 gives $t_\mathrm{c}(r) \propto r^{0.5} M^{-0.02}$ for $r \ll a$.*

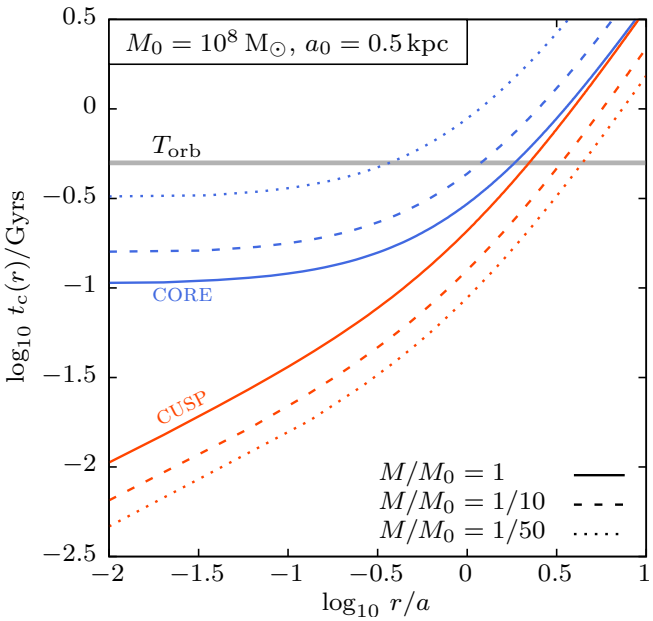

Figure 2.1: The internal period $t_\mathrm{c}(r)$ of a circular orbit of radius r in cuspy ($\gamma = 1$) Dehnen (1993) profiles tends towards zero for $r \to 0$, whereas for cored ($\gamma = 0$) profiles, it approaches a constant, non-zero value. This is shown for subhaloes of initial mass $M_0 = 10^8\,\mathrm{M}_\odot$ and scale radius $a_0 = 0.5\,\mathrm{kpc}$ (solid lines). For cuspy (cored) profiles, tidal stripping decreases (increases) $t_\mathrm{c}(r)$ at fixed fractions r/a of the scale radius: dashed (dotted) lines are computed using the tidal tracks discussed in chapter 4.A and show $t_\mathrm{c}(r)$ when the subhalo has been tidally stripped to a remnant mass fraction of $M/M_0 = 1/10$ (1/50). As a consequence, for cuspy profiles, the fraction of particles which react adiabatically to a tidal perturbation increases with tidal stripping. An orbital period of $T_\mathrm{orb} = 0.5\,\mathrm{Gyrs}$ within the host halo is shown as guidance for the time available for the subhalo to reach dynamical equilibrium between two pericentre passages.

it becomes increasingly difficult for the subhalo to reach dynamical equilibrium within T_orb. This drives the eventual tidal disruption of the cored subhalo. In this context, the term *artificial* disruption has been coined by van den Bosch et al. (2018) for the disruption of subhaloes in cosmological simulations caused by numerical issues.

2.3 Core formation in numerical simulations

In the spirit of van den Bosch et al. (2018), in this section, we perform a numerical experiment to demonstrate how density cores form artificially due to insufficient numerical resolution. For this purpose, we generate an equilibrium N-body realisation of a cuspy DM halo (with the general method described in chapter 2.3.1) and evolve it in isolation (chapter 2.3.2) using the particle-mesh code SUPERBOX (Fellhauer et al. 2000, see thesis chapter 1.5.1).

[2] *The apparent indestructibility of cuspy subhaloes is consistent also with their tidal radius r_t: For a subhalo with pericentre distance r_peri, the tidal radius can be approximated as the radius r_t for which $\langle\rho(<r_\mathrm{t})\rangle = 3\langle\rho_\mathrm{host}(<r_\mathrm{peri})\rangle$ (see e.g. Peñarrubia et al., 2008b), where by $\langle\rho(<r_\mathrm{t})\rangle$ we denote the mean density of the subhalo averaged within r_t, and equivalently by $\langle\rho_\mathrm{host}(<r_\mathrm{peri})\rangle$ the mean density of the host halo averaged within r_peri. The diverging central density of a cuspy subhalo, $\rho(r) \to \infty$ for $r \to 0$, guarantees the existence of a finite and non-zero tidal radius r_t, and therefore suggests that a fraction of particles will remain bound to the subhalo after tidal interaction.*

2.3.1 Generation of equilibrium models

Throughout this thesis, we make use of spherical equilibrium N-body models with isotropic velocity dispersion, and summarise in this subsection the procedure to generate such models. We aim to generate an N-body model of (tracer) density $\nu(r) = \mathrm{d}N/\mathrm{d}^3r$ which is in dynamical equilibrium in a spherical potential $\Phi(r)$. The distribution function (hereafter DF) $f(E) = dN/d\Omega$ which determines the number N of particles of energy E per phase space volume element $\mathrm{d}\Omega = \mathrm{d}^3r\,\mathrm{d}^3v$ (Fig. 2a) can be obtained from $\nu(r)$ and $\Phi(r)$ using Eddington inversion (see e.g. chapter 4.4 in BT87):

$$f(E) = \frac{1}{\sqrt{8}\pi^2} \int_E^0 \frac{\mathrm{d}^2\nu}{\mathrm{d}^2\Phi} (\Phi - E)^{-1/2}\,\mathrm{d}\Phi\ , \tag{2.3}$$

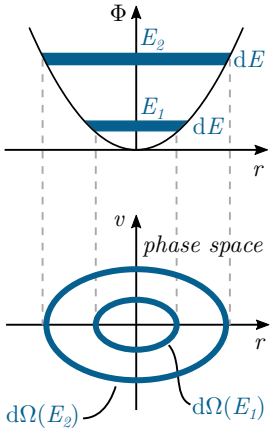

Fig. 2a: *Particles with a range of energies dE centred on E have access to a phase space volume* $\mathrm{d}\Omega(E)$.

which holds in this form if for $r \to \infty$ both $\Phi \to 0$ and $\mathrm{d}\nu/\mathrm{d}\Phi \to 0$. In equation 2.3, the tracer density $\nu(r)$ is normalised so that $N = 4\pi \int_0^\infty r^2\nu(r)\mathrm{d}r$. For the case of self-gravitating models, the potential $\Phi(r)$ is sourced by the mass density $\rho(r) = m\nu(r)$, where by m we denote the mass of a single particle. Following the notation of ch. 2.2 in S87, each particle of energy E has access to a differential phase space volume of $\mathrm{d}\Omega/\mathrm{d}E = (4\pi)^2 p(E)$, where

$$p(E) = \int_0^{r_{\mathrm{apo}}(E)} \{2\,[E - \Phi(r)]\}^{1/2}\, r^2\,\mathrm{d}r\ . \tag{2.4}$$

The integration limits correspond to the minimum and maximum radii r accessible to a particle with energy E in the potential $\Phi(r)$. The differential energy distribution $n(E) = \mathrm{d}N/\mathrm{d}E$ then becomes

$$n(E) = (4\pi)^2 p(E) f(E)\ . \tag{2.5}$$

We deduce from equations 2.4 and 2.5 that at given radius r, the likelihood of a particle to have energy E is $\mathcal{L}(E|r) \propto \{2\,[E - \Phi(r)]\}^{1/2} r^2 f(E)$. This allows us to generate equilibrium N-body models using a two-step procedure: we first draw radii r through inverse transform sampling of the tracer density $\nu(r)$ (Fig. 2b), and subsequently energies E through rejection-sampling with the likelihood $\mathcal{L}(E|r)$ (Fig. 2c). For isotropic systems, energies and radii uniquely determine the velocities of the N-body particles. A basic implementation of this method is made available online[1].

[1] github.com/rerrani/nbopy

2.3.2 Numerical experiment for core formation

To illustrate the artificial formation of density cores in *collisionless* N-body models of originally cuspy subhaloes, we evolve a Dehnen (1993) model of $N = 10^7$ particles, total mass $M = 10^8\,\mathrm{M}_\odot$ and scale radius $a = 0.5\,\mathrm{kpc}$ in isolation using SUPERBOX (Fellhauer et al. 2000, see thesis chapter 1.5.1). This particle-mesh code employs co-moving grids centred on the densest region in the halo. We choose a low grid

resolution of $\Delta x = 20a/64 = 0.16\,\mathrm{kpc}$ for the highest-resolving grid to highlight the effect of artificial core formation. While this experiment is run in isolation, i.e. in absence of an external potential, we will show in section 2.4.2 that the scale radius a of a subhalo experiencing tidal mass loss decreases over time. Consequently, also the ratio $a/\Delta x$ decreases and can easily reach values as extreme as in our experimental setup. We chose a time step of $\Delta t = t_\mathrm{c}(a)/400 = 0.5\,\mathrm{Myrs}$. Note that the applied particle mesh code is collisionless and does not suffer from artificial self-heating driven by two-body relaxation.

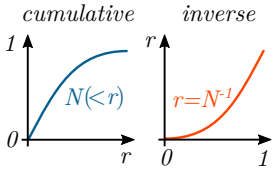

Fig. 2b: *Inverse transform sampling: The differential number of tracers in a shell of radius r equals $n(r)=4\pi r^2\nu(r)$. Let $N(<r)$ be the corresponding cumulative distribution, normalised so that $N(<\infty)=1$, with inverse N^{-1}. Drawing $N_i \in [0,1]$ with uniform distribution, the corresponding radii $\{r_i=N^{-1}(N_i)\}$ follow a distribution with probability density function $n(r)$ (see ch. 7.2 in P+92).*

Figure 2.2 compares the analytical model and unevolved ($t = 0$) collisionless N-body realisation against a model evolved for a time of $4t_\mathrm{c}(a)$. A density core forms on the scale of the resolution Δx of the highest-resolving grid. Energies E, differential energy distribution $n(E)$ and DF $f(E)$ are calculated for the N-body models using positions and velocities provided by SUPERBOX. We assume spherical symmetry and that both $f(E)$ and $p(E)$ are functions of energy alone, which allows $p(E)$ to be computed from equation 2.4, and $f(E) = (4\pi)^{-2}\, n(E)\, p^{-1}(E)$, where the differential energy distribution $n(E)$ is measured directly from the N-body particles. The differential energy distribution $n(E)$ of the evolved N-body model has fewer particles at the highest binding energies than the unevolved model and analytical counterpart, but at less-bound energies, both $n(E)$ and the DF of the evolved N-body model follow closely the analytical form.

2.4 Reconstruction of the cusp

We now explore how to reconstruct the density cusp with the aim to follow the tidal evolution of a single subhalo in a Milky Way-like host potential for arbitrarily large fractions of tidally stripped mass, avoiding artificial disruption. In section 2.4.1 we describe the analytical, evolving host potential as well as the initial conditions for the subhalo used in our controlled simulations. The cusp reconstruction method is introduced and then applied to follow the tidal evolution of a subhalo in section 2.4.2.

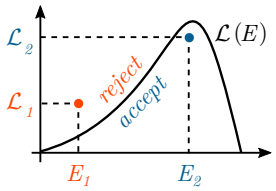

Fig. 2c: *Rejection method: Drawing $\mathcal{L}_i \in [0, \max(\mathcal{L})]$ and $E_i \in [\min(E), 0]$ with uniform distribution, and rejecting all E_i for which $\mathcal{L}(E_i) > \mathcal{L}_i$, the remaining set of $\{E_i\}$ follows a distribution with probability density function $\mathcal{L}(E)$ (see ch. 7.3 in P+92).*

2.4.1 Numerical setup

Host. The parameters of the analytical, time-evolving host potential at redshift $z = 0$ are motivated by the McMillan (2011) Milky Way model with a circular velocity of $v_c = 240\,\mathrm{km\,s^{-1}}$ at a solar radius of $R_0 = 8.29\,\mathrm{kpc}$. We model the Milky Way disc as an axisymmetric two-component model consisting of a thin and thick Miyamoto & Nagai (1975) disc with $M = 7.3 \times 10^{10}\,\mathrm{M}_\odot$, $a_d = 3.9\,\mathrm{kpc}$, $b_d = 0.31\,\mathrm{kpc}$ ($M = 2.0 \times 10^{10}\,\mathrm{M}_\odot$, $a_d = 4.4\,\mathrm{kpc}$, $b_d = 0.92\,\mathrm{kpc}$) for the thin (thick) disc, respectively. The Bulge is modelled as a Hernquist (1990) sphere with $M = 2.1 \times 10^{10}\,\mathrm{M}_\odot$, $a = 1.3\,\mathrm{kpc}$, and the DM halo as a spherical Navarro et al. (1997) profile with scale mass $M_s = 1.53 \times 10^{11}\,\mathrm{M}_\odot$, scale radius $r_s = 20.2\,\mathrm{kpc}$ and concentration $c = 9.49$, which results

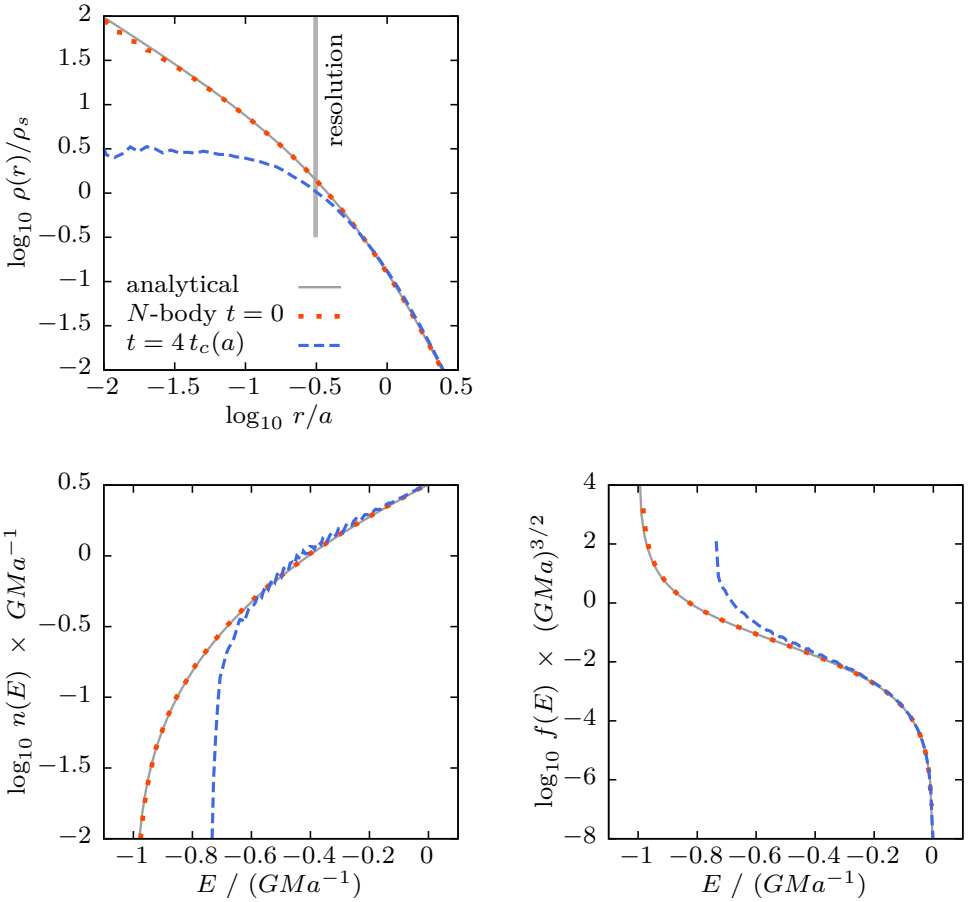

Figure 2.2: A cuspy Dehnen (1993) model ($\{\alpha, \beta, \gamma\} = \{1, 4, 1\}$) of mass M and scale radius a evolved in isolation using a particle-mesh code with a spatial resolution of $\Delta x = 20a/64 = 0.16\,\mathrm{kpc}$ forms a density core ($\mathrm{d}\ln\rho/\mathrm{d}\ln r \to 0$ for $r \to 0$) on the scale of the spatial resolution of the simulation (top panel). The differential energy distribution $n(E)$ reveals that the evolved N-body models is missing particles with the most-negative energies compared to the analytical and unevolved model (bottom-left panel). The distribution function for less-bound energies follows closely the analytical model (bottom-right panel).

in a virial mass of $M(< cr_s) = 1.40 \times 10^{12}\,\mathrm{M}_\odot$. The scale mass evolves with redshift, $M_s(z) \propto \exp(-2a_g z)$, whereas $r_s(z) \propto \exp(-2a_g z/\gamma_g)$, following the model by Buist & Helmi (2014) with parameters $\gamma_g = 2$ for strict inside-out growth and $a_g = 0.2$, motivated as a rough mean of the values found for the Aquarius (Springel et al., 2008) simulations. We use the same recipe for the evolution of disc and bulge. As cosmology, we adopt $\Omega_\mathrm{m} = 0.32$, $\Omega_\Lambda = 0.68$, $H_0 = 67\,\mathrm{km\,s^{-1}\,Mpc^{-1}}$ (Planck Collaboration et al., 2018).

Subhalo. We model the subhalo at infall as an equilibrium Dehnen (1993) profile with 10^8 particles, total mass $M = 10^8\,\mathrm{M}_\odot$ and scale radius $a = 0.5\,\mathrm{kpc}$ using the method described in section 2.3.1. These structural parameters are chosen to be compatible with a progenitor of the ultra-faint Tucana III dwarf galaxy, as will be detailed in section 2.5, and correspond to a maximum circular velocity $v_\mathrm{max} = 15\,\mathrm{km\,s^{-1}}$ at a radius $r_\mathrm{max} = a = 0.5\,\mathrm{kpc}$. These values lie within one standard deviation from the mean r_max-v_max relation for subhaloes found in the Aquarius simulations (Springel et al., 2008, figure 26). The model is placed on an orbit constrained from the radial velocity (Simon et al., 2017) and proper motion measurements (Simon, 2018) of Tuc III. While recently the radial systemic velocity measurement has been refined (Li et al., 2018), the peri- and apocentre of our model, $r_\mathrm{peri} \approx 2.5\,\mathrm{kpc}$ and $r_\mathrm{apo} \approx 42\,\mathrm{kpc}$, are roughly consistent with those tailored to match the stream (Erkal et al., 2018) and given the example nature of our numerical experiments an exact match of the orbit should not be of concern. The ratio $r_\mathrm{peri}/r_\mathrm{apo} \sim 0.06$ is consistent with values derived from cosmological simulations of Milky Way-like haloes: for the 50 most massive satellites at $z = 0$ in the *Via Lactea* simulation (Diemand et al., 2007), Lux et al. (2010) find an average value of $r_\mathrm{peri}/r_\mathrm{apo} \sim 0.2 \pm 0.1$. Both peri- and apocentre distance of the Tucana III orbit lie approximately one standard deviation below the average values determined by Lux et al. (2010). We generate initial conditions by rewinding the orbit for 7 past pericentre passages. For our choice of host halo and subhalo structural parameters, this results in a tidally stripped subhalo at $z = 0$ with a velocity dispersion that is compatible with Tuc III (see section 2.5).

PM-code. The numerical integration of the subhalo evolution is carried out using the particle-mesh code SUPERBOX (Fellhauer et al. 2000, see thesis chapter 1.5.1). This code employs two grids co-moving with the subhalo of resolution $\Delta x = 2a/128$ and $20a/128$, centred on the density maximum, as well as a fixed grid of resolution $1\,\mathrm{Mpc}/128$. We choose a time-step of $\Delta t = t_\mathrm{c}(a)/400$. For the initial simulation run, this gives $\Delta x = 8\,\mathrm{pc}$ and $\Delta t = 0.5\,\mathrm{Myrs}$. For convergence tests, we also run models with $N = 10^7$ at a resolution of $2a/256$ and $2a/128$.

Initial simulation

Figure 2.3 shows simulation snapshots taken at the 1st, 2nd, 4th and 6th apocentre after infall, corresponding to 1, 2, 4 and 6 preceding pericentre passages. The subhalo loses mass through tidal stripping, and the stripped particles form a tidal stream,

which due to the high eccentricity of the orbit spreads out as concentric shells in the galactic halo.

The evolution of the subhalo density profile is shown in Figure 2.4. In agreement with previous studies (e.g. Hayashi et al., 2003; Peñarrubia et al., 2008b), the subhalo central density decreases during tidal stripping, the scale radius shrinks, and the outer slope of the density profile steepens (see also Peñarrubia et al., 2010).

During this tidal evolution, the velocity dispersion of the subhalo decreases. The central regions of the subhalo maintain an isotropic velocity dispersion ($\beta(r) \approx 0$) whereas at outer radii, motions are tangentially biased ($\beta < 0$), see Figure 2.5.

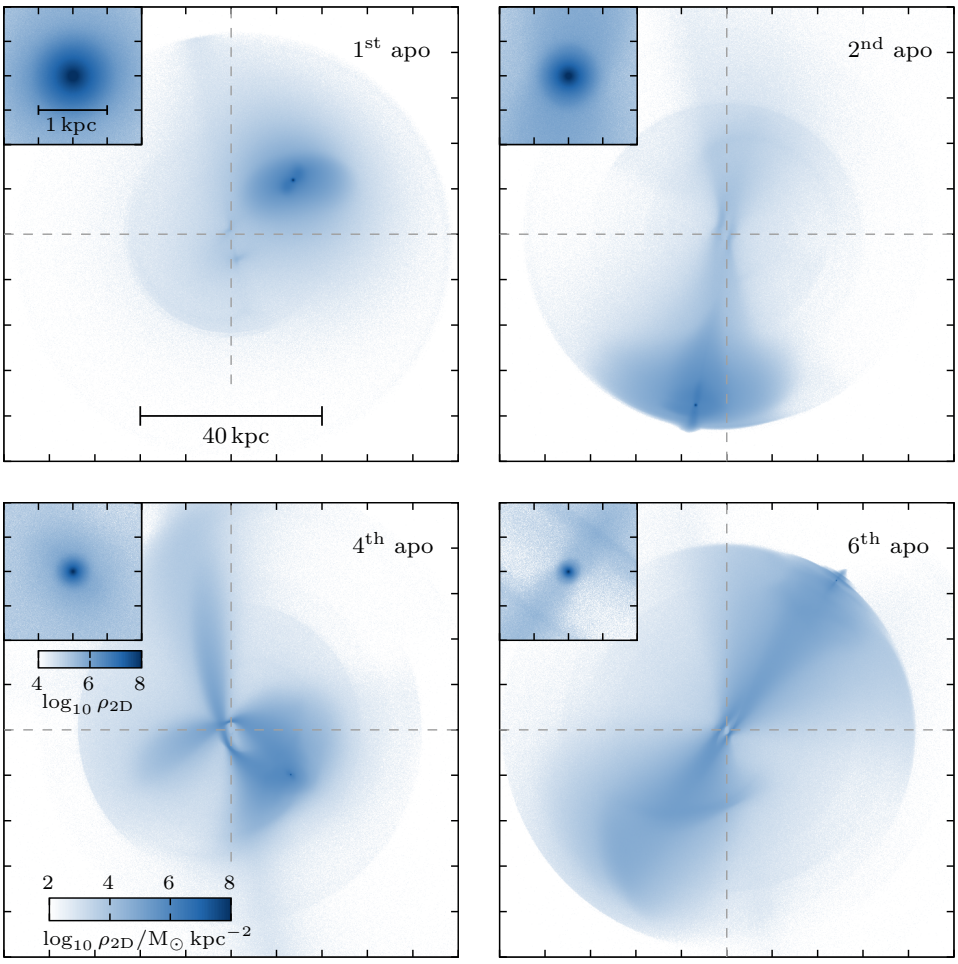

Figure 2.3: Apocentre snapshots of the controlled simulations of a cuspy DM halo in a Milky Way-like potential. The subhalo is on an eccentric orbit with a pericentre distance of 2.5 kpc. Tidal stripping of the subhalo leads to the formation of a tidal stream which spreads out as concentric shells. Each of the four displayed frames covers an area in the (x, y)-plane of $(100\,\mathrm{kpc})^2$. The smaller frames are centred on the subhalo and cover an area of $(2\,\mathrm{kpc})^2$. The colour-coding shows the (projected) DM density ρ_{2D}, integrated along the z-axis.

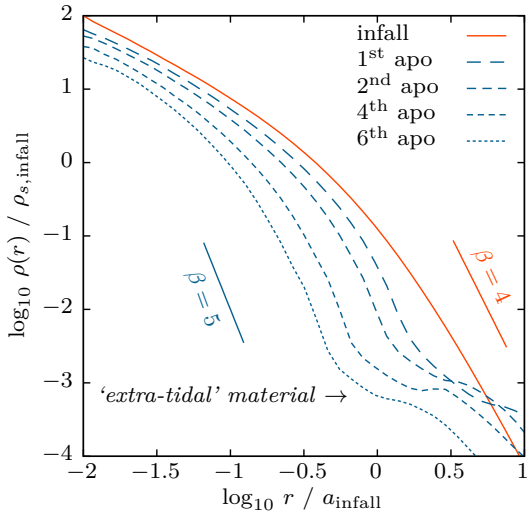

Figure 2.4: Subhalo density profile $\rho(r)$ measured from the controlled simulation with $N = 10^8$ particles at infall (solid curve) and subsequent apocentres (dashed curves). Radius r and density $\rho(r)$ are normalised by the scale radius a and scale density ρ_s of the subhalo at infall. The outer slope β steepens during the tidal evolution.

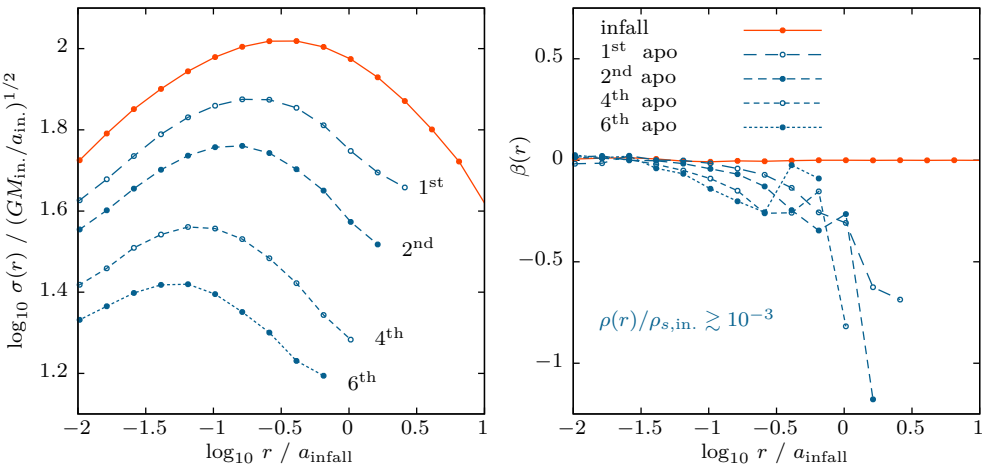

Figure 2.5: Subhalo velocity dispersion profile $\sigma(r)$ (left panel) and anisotropy parameter $\beta(r)$ (right panel) for the same apocentre snapshots as shown in Figure 2.4. The subhalo cools down during tidal evolution and maintains an isotropic centre, while at outer radii, the motions are tangentially biased. The dispersions are calculated from bound particles only and are shown for radii r where $\rho(r)/\rho_{s,\mathrm{infall}} \gtrsim 10^{-3}$ to limit the impact of extra-tidal features.

2.4.2 Controlled simulation

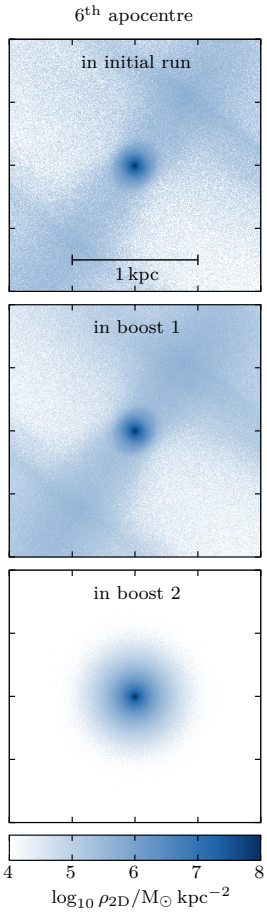

Fig. 2d: *Subhalo snapshots corresponding to the 6th apocentre after infall. The top panel shows the evolved model in the initial simulation with 10^8 particles. The middle panel shows the evolved model in the first cusp reconstruction run (boost 1). This snapshot is subsequently used to generate the unevolved model for the second cusp reconstruction (boost 2), shown in the bottom panel.*

We now aim to reconstruct the density cusp during the simulation. This reconstruction is based on the assumptions that

(i) the DM density profile at apocentre can be approximated by an $\{\alpha, \beta, \gamma\}$ profile,

(ii) the central slope of that profile equals $\gamma = -\mathrm{d}\ln\rho/\mathrm{d}\ln r = 1$.

The cusp reconstruction (*boost*) then involves the following steps:

(i) At apocentre, we fit an $\{\alpha, \beta, \gamma\}$-profile to the bound particles of the subhalo, fixing $\alpha = 1$, $\gamma = 1$ and matching $r_{\max}$ and $M_{\max} = M(< r_{\max})$ of the simulated subhalo, where by $r_{\max}$ we denote the radius of maximum circular velocity.

(ii) We then generate an equilibrium N-body realisation of $N = 10^7$ particles of the fitted density profile as described in section 2.3.1, and place it on the orbit of the simulated subhalo (Fig. 2d).

(iii) The spatial resolution Δx of the particle-mesh code and time step Δt of the integration routine are re-scaled with the fitted $r_{\max}$ and mass $M_{\max}$ so that $\Delta x = 2r_{\max}/128$ and $\Delta t = t_{\mathrm{c}}(r_{\max})/400$, i.e. we preserve the numerical resolution relative to properties of the evolved subhalo.

We decide to reconstruct the cusp when the mass fraction within the innermost grid cell – assuming a cuspy profile – equals roughly 0.5 per cent of the current total subhalo mass. We have chosen this mass scale after performing convergence tests to verify that at these scales the unresolved centre of the cusp does not alter the tidal evolution of the subhalo. For a simulation with initial spatial resolution of $\Delta x = 2r_{\max}/128$, under the assumption of Dehnen (1993) density profiles (where $r_{\max} = a$), this corresponds to a halo scale radius that has decreased by a factor of ~ 4 due to tidal stripping. For the simulated subhalo, this means re-constructing the density cusp approximately every three pericentre passages. Initial structural parameters of the cusp reconstructions are listed in Table 2.1.

Figure 2.6 illustrates the 3rd cusp reconstruction (*boost*) of our simulation, performed at the 10th apocentre, i.e. after 9 pericentre passages. The left-hand panel shows the mass per radial shell $dM/dr \propto r^2\rho(r)$ as a function of radius r. The fitted $\{\alpha, \beta, \gamma\}$-profile matches the evolved N-body model (corresponding to the last apocentre snapshot of the simulation starting from the 2nd cusp reconstruction) well at the radii where most particles are located, i.e. around the radius r_{-2} where $\mathrm{d}\ln\rho/\mathrm{d}\ln r|_{r_{-2}} = -2$ and the $r^2\rho(r)$ curve peaks. For $r < \Delta x$, the fitted profile re-constructs the density cusp. At apocentre, the subhalo is surrounded by *extra-tidal* material with energies close to zero as a result of past pericentre passages (e.g. Peñarrubia et al., 2009). For the evolved N-body model in Figure 2.6, this extra-tidal material is visible for radii larger than a few scale radii. The extra-tidal material is not in equilibrium with the subhalo. To compare the differential energy distribution $n(E)$ and DF of our

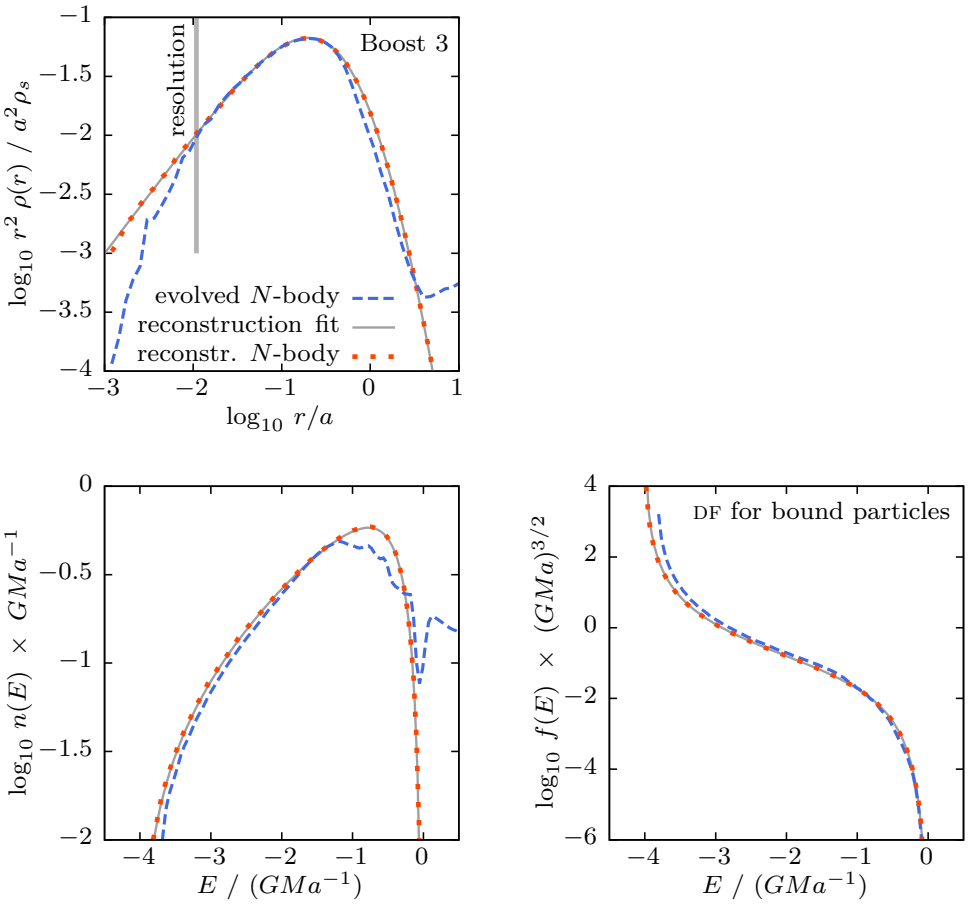

Figure 2.6: The top panel shows an $\{\alpha, \beta, \gamma\} = \{1, 7, 1\}$ fit to bound N-body particles of a tidally stripped subhalo (*evolved N-body*), reconstructing the density cusp with central slope $\gamma = 1$. The reconstructed N-body model corresponds to the third cusp reconstruction (*boost 3*) in Figures 2.7 and 2.8, whereas the *evolved N-body* model corresponds to the last apocentre snapshot of the simulation starting from the second cusp reconstruction (*boost 2*). The fit matches the N-body model best for those radial shells which contain the largest number of particles, i.e. around r_{-2}, where the $r^2\rho(r)$ curve peaks. The outer profile is matched with less accuracy, which can also be seen from the differential energy distribution $n(E)$ (bottom-left panel). Convergence tests however demonstrate that the tidal evolution is insensitive to an exact match of the outer density profile.

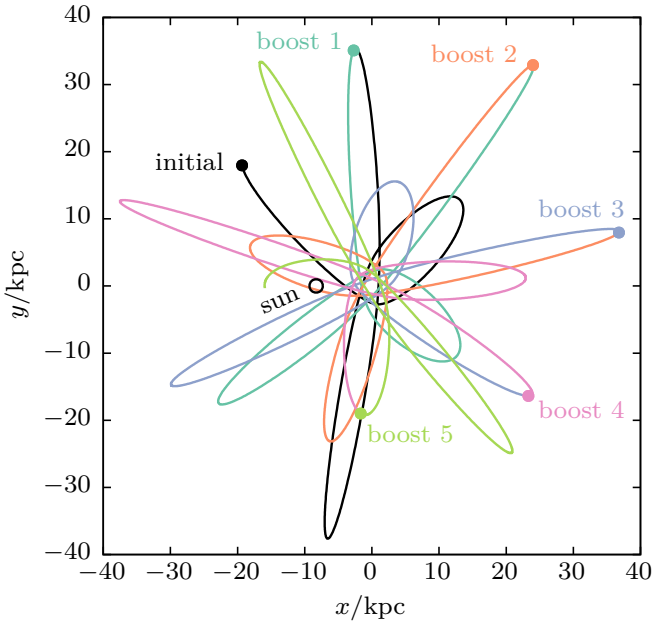

Figure 2.7: Projection of the subhalo orbit on the galactic plane, with orbital parameters chosen to approximate those of the Tucana III dwarf galaxy ($r_{\rm peri} \approx 2.5\,$kpc, $r_{\rm apo} \approx 42\,$kpc). We periodically reconstruct the central density cusp of the subhalo and adapt the resolution of the simulation to the subhalo structural parameters. These *boosts* are shown using different colours, with the corresponding first apocentre indicated by a filled circle. The current ($t = 0$) position of the sun $(x_\odot, y_\odot) = (-8.29\,{\rm kpc}, 0)$ is marked by an open circle.

reconstruction to the evolved N-body model, we allow the evolved N-body model to relax in isolation for 4 dynamical times. Both the differential energy distribution $n(E)$ and DF of this relaxed model are well matched by the reconstruction except for energies close to zero. Cusp reconstructions consequently do not conserve the total mass or total energy of the subhalo. To give a numerical example, while $M_{\rm max}$ differs between the final snapshot of the simulation starting from the $2^{\rm nd}$ cusp reconstruction and the first snapshot of the $3^{\rm rd}$ cusp reconstruction by $\approx 1\,$per cent, the total binding energy between the snapshots differs by $\approx 10\,$per cent - driven by the large fraction of mass at energies close to zero, where the fit matches the N-body model less accurately. Our convergence tests however show that the tidal evolution is insensitive to a precise match at these energies, or similarly, to a precise match of the subhalo outer profile.

The orbit of the simulated subhalo is shown in Figure 2.7, and the apocentres – where we reconstruct the density cusp, adapt spatial resolution Δx and time step Δt to the evolved structural parameters, and re-start the simulation (*boosts*) – are marked by filled points. Figure 2.8 shows the tidal evolution of $M_{\rm max} = M(< r_{\rm max})$ and $r_{\rm max}$ of the subhalo, measured at subsequent apocentres: by periodically reconstructing the density cusp, we can follow the tidal evolution of the subhalo for arbitrarily large fractions of tidally stripped mass. We choose to show $\{M_{\rm max}, r_{\rm max}\}$ instead of

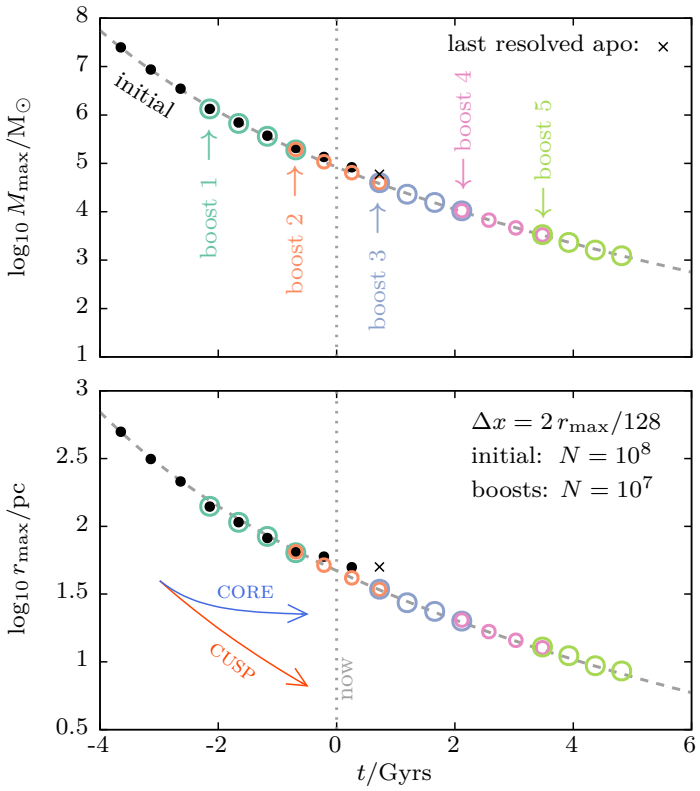

Figure 2.8: Evolution of $M_{\max} = M(< r_{\max})$ (top panel) and $r_{\max}$ (bottom panel) of a subhalo with initial total mass $M = 10^8 \mathrm{M}_\odot$ and scale $a = 0.5\,\mathrm{kpc}$. Each point corresponds to an apocentre passage of the subhalo. Black filled circles mark the simulation with highest resolution, a cross indicates the last apocentre before (artificial) disruption. Coloured circles are simulation runs (*boosts*) where the density cusp is reconstructed as detailed in section 2.4.2: by reconstructing the density cusp, the subhalo does not disrupt, and can be traced over many orders of magnitude in mass loss. The evolution of $r_{\max}$ is highly sensitive to the spatial resolution of the simulation and *artificially* flattens off once the simulation fails to resolve the subhalo peak circular velocity. Tidal evolutionary tracks (see section 4.A) for cuspy and cored subhaloes are shown as a reference. Dashed curves show fits of equation 2.6 to the mass evolution (top panel) and the predicted $r_{\max}$ evolution assuming power-law scaling $r_{\max} \propto M_{\max}^{\kappa}$ (bottom panel).

$\{M, a\}$ as the former can be computed directly from the N-body data without further assumptions about the DM profile shape. The *boosts* (with $N = 10^7$) follow closely the evolution of the highest-resolving *initial* simulation (with $N = 10^8$) for those apocentre snapshots with $r_{\rm max} \ll \Delta x$, where by Δx we denote the spatial resolution of the particle mesh.

The last apocentre snapshot of the highest-resolving *initial* simulation is indicated by a cross in Figure 2.8: beyond this snapshot, the radius of maximum circular velocity $r_{\rm max}$ is not resolved by the simulation. Power et al. (2003) argues that subhaloes are resolved for those radii r where the acceleration $a(r) = GM(<r)/r^2$ does not exceed a *characteristic* acceleration, which depends on the gravitational force softening length ϵ. Based on this idea, van den Bosch & Ogiya (2018) propose that a subhalo can be considered sufficiently resolved if $r_{\rm h}/\epsilon > 7^{+3}_{-2}$, where $r_{\rm h}$ indicates the half-mass radius of the subhalo. For Dehnen (1993) profiles, and assuming that $\epsilon \approx \Delta x = 2r_{\rm max,0}/128$, this translates to $r_{\rm max,0}/r_{\rm max} < 22^{+8}_{-6}$, where by $r_{\rm max,0}$ we denote the radius of maximum circular velocity at the beginning of the simulation. The upper limit of this criterion when applied to the highest-resolving *initial* simulation corresponds to $\log_{10}(r_{\rm max}/{\rm pc}) \approx 1.5$, of the same order as the value measured for the last resolved snapshot, $\log_{10}(r_{\rm max}/{\rm pc}) \approx 1.7$.

The mass evolution is well fitted using the model of van den Bosch et al. (2005) who postulate an orbit-averaged mass loss rate of ${\rm d}M/{\rm d}t = -M\psi^\zeta/\tau$, where M denotes the subhalo mass, $\psi = M/M_{\rm host}$ and ζ is a constant. In the following, we will use $M_{\rm max}$ as a proxy for subhalo mass, and the host halo scale mass as measure for $M_{\rm host}$. As our numerical experiment covers only a narrow range of redshifts, we will assume in the following a static host mass: during the simulated redshift interval of $\Delta z \approx 0.6$ between the first and the last snapshot shown in Figure 2.8, the host halo scale mass increases by a factor $\exp(2a_g\Delta z)$ (see section 2.4.1), i.e. by less than 30 per cent, whereas the subhalo mass decreases by more than four orders of magnitude. Integration yields

$$M_{\rm max}(t) = \begin{cases} M_{\rm max,0}\ \exp(-t/\tau) & \text{if } \zeta = 0 \\ M_{\rm max,0}\ \left[1 + \zeta\psi_0^\zeta (t/\tau)\right]^{-1/\zeta} & \text{if } \zeta \neq 0 \end{cases}, \tag{2.6}$$

where $M_{\rm max,0} = M_{\rm max}(t=0)$ and $\psi_0 = M_{\rm max,0}/M_{\rm host}$. A fit of equation 2.6 to the simulated data with $M_{\rm host} = M_{\rm s} = 1.53 \times 10^{11}\,{\rm M}_\odot$ (see section 2.4.1) results in a characteristic time $\tau = (160 \pm 5)\,{\rm Myrs}$ (i.e. $\tau/T_{\rm orb} \approx 0.34$), a power-law index for the dependence on host mass of $\zeta = 0.118 \pm 0.002$, and $M_{\rm max,0} = (8.4 \pm 0.1) \times 10^4\,{\rm M}_\odot$. The fit is shown using a dashed line in the top panel of Figure 2.8. Note that this fit serves to parametrize the mass loss of a specific subhalo, whereas average mass loss rates for the entire population of subhaloes of a given merger are generally lower (Giocoli et al., 2008; Jiang & van den Bosch, 2016).

The slight departure of the mass evolution from an exponential ($\zeta \neq 0$) may be tied to the non-self similar evolution of the subhalo, i.e. the steepening of the outer slope

β of the density profile during tidal evolution (see Figure 2.4). The rate $\mathrm{d}M_{\mathrm{max}}/\mathrm{d}t$ of tidal stripping is largest when the subhalo model is first injected in the host potential. We generate equilibrium realisations of N-body models in isolation, and in the case of the Dehnen (1993) profile with $\{\alpha, \beta, \gamma\} = \{1, 4, 1\}$, the differential energy distribution is a monotonously increasing function for $E \to 0$ (see bottom-left panel of Figure 2.2), i.e. there is a large fraction of particles at low binding energies. Those N-body particles at low binding energies are stripped once the subhalo is injected. With the steepening of the outer slope β during tidal stripping ($\beta = 4$ at infall, $\beta = 7$ after 9 pericentre passages, see Table 2.1), a smaller mass fraction of the subhalo is associated to low binding energies: for the $\{1, 7, 1\}$ profile, $n(E) \to 0$ for $E \to 0$ (bottom-left panel of Figure 2.6), and the subhalo becomes more resilient to tides. This observation may be inverted: as self-bound (sub)haloes in an external potential cannot have particles with energies arbitrarily close to zero, assuming profiles with isotropic velocity dispersion, their density must decrease more rapidly than $\mathcal{O}(r^{-4})$.

The radius r_{max} of maximum circular velocity decreases during tidal stripping, as shown in the bottom panel of Figure 2.8. Once r_{max} is of the same order as the resolution Δx, the evolution of r_{max} flattens off, i.e. $\mathrm{d}r_{\mathrm{max}}/\mathrm{d}t \to 0$. This behaviour is symptomatic of the formation of the artificial density core as it resembles that of cored DM subhaloes in controlled collisionless simulations (see section 4.A) – tidal evolutionary tracks for cuspy and cored systems are plotted with solid lines Figure 2.8, using the smooth mass evolution of equation 2.6.

Furthermore, we fit a power-law $r_{\mathrm{max}} \propto M_{\mathrm{max}}^{\kappa}$ to the subhalo mass-size evolution. The fitted slope $\kappa = 0.415 \pm 0.001$ is lower than the value found in chapter 4.A from an average of re-simulations of the Aquarius A2 merger tree ($\kappa \approx 0.48$). This may be related to strong disc shocking of our subhalo model experienced due to the particularly low pericentre distance ($r_{\mathrm{peri}} \approx 2.5\,\mathrm{kpc}$), potentially heating up the subhalo, affecting its mass-size evolution. The dashed line in the bottom panel of Figure 2.8 shows the size evolution as described through the power-law fit in combination with the mass evolution of equation 2.6.

In agreement with the cuspy model of section 2.2, the period $t_{\mathrm{c}}(r_{\mathrm{max}})$ of a circular orbit with radius r_{max} decreases during tidal stripping: assuming $r_{\mathrm{max}} \propto M_{\mathrm{max}}^{\kappa}$, for $\mathrm{d}M_{\mathrm{max}}/\mathrm{d}t < 0$, we find $\mathrm{d}t_{\mathrm{c}}(r_{\mathrm{max}})/\mathrm{d}t < 0$ if $\kappa > 1/3$. This is satisfied by the fitted value of κ for the simulated cuspy subhalo. The subhalo therefore has increasing multiples of its dynamical time to relax and reach equilibrium between subsequent tidal interactions. In contrast, $\kappa \to 0$ for cored subhaloes as the r_{max} evolution flattens off (see section 4.A), and $t_{\mathrm{c}}(r_{\mathrm{max}})$ increases during tidal stripping.

Table 2.1: Initial structural parameters of DM subhaloes and stellar populations used in the simulation runs (see sections 2.4.2 and 2.5). Simulations are started at time t, where times $t > 0$ lie in the future. The table lists the enclosed mass $M_{\max}$ within the radius of maximum circular velocity $r_{\max}$ and outer slope β for $\{\alpha, \beta, \gamma\} = \{1, \beta, 1\}$ DM profiles, as well as luminosity L, half-light radius $R_{\rm h}$ and dynamical mass-to-light ratio $\langle M/L \rangle$ (averaged within $R_{\rm h}$) for the embedded stellar Plummer spheres.

	$\frac{t}{\text{Gyrs}}$	$\frac{M_{\max}}{\text{M}_\odot}$	$\frac{r_{\max}}{\text{pc}}$	β	$\frac{L}{\text{L}_\odot}$	$\frac{R_{\rm h}}{\text{pc}}$	$\frac{\langle M/L \rangle}{\text{M}_\odot/\text{L}_\odot}$
initial	-3.6	2.5×10^7	500	4.0	3100	35	270
boost 1	-2.1	1.3×10^6	140	5.5	2600	44	220
boost 2	-0.7	1.9×10^5	64	6.0	1400	50	200
boost 3	0.7	4.0×10^4	34	7.0	230	41	410
boost 4	2.1	1.0×10^4	20	7.5	18	29	1600
boost 5	3.5	3.2×10^3	12	8.0	1.2	20	8200

2.5 Application to Milky Way dSphs: Tucana III

We now apply the method of reconstructing the density cusp to study the tidal evolution of dwarf galaxies embedded in cuspy DM subhaloes. This is of particular interest because of the recent discoveries of several faint, low-mass dwarf galaxies in the Milky Way (e.g. Drlica-Wagner et al., 2015; Koposov et al., 2015; Torrealba et al., 2016), some of them showing tidal features. Motivated by the large dynamical mass-to-light ratios inferred for Milky Way dwarf galaxies (e.g. Walker et al., 2007), the following analysis is carried out under the assumption that stars are mass-less tracers of the underlying DM potential. This allows us to model the evolution of the stellar component using the DF-based method introduced by Bullock & Johnston (2005): If both the stellar and DM density distributions are spherical, assuming isotropic velocity dispersion profiles, their DFs can be written as functions of energy E. Then, in the notation of equation 2.5, the probability of an N-body particle with energy E to represent a star is proportional to

$$\mathcal{P}_\star(E) \propto \frac{n_\star(E)}{n(E)} = \frac{f_\star(E)}{f(E)} \,, \tag{2.7}$$

as the potential is sourced by DM only and therefore the density of states $p_\star(E) = p(E)$ cancels (see Figure 2.9 for an example of a tagging probability distribution). We compute the probabilities $\mathcal{P}_\star(E)$ at infall, and re-compute them after each cusp reconstruction. Structural and kinematic properties of the stellar component can be inferred from the DM distribution by applying the individual $\mathcal{P}_\star(E)$ as weights. A basic implementation of this method is made available online together with code to generate equilibrium N-body models, see section 2.3.1.

Luminosity and projected half-light radius of the stellar component are chosen so that the evolved model approximately matches the Tucana III dwarf galaxy at redshift $z = 0$ (Fig. 2e): $L = 780^{+350}_{-240}\,\mathrm{L}_\odot$, $R_\mathrm{h} = (44 \pm 6)\,\mathrm{pc}$ (Drlica-Wagner et al., 2015), with an upper limit on the line-of-sight velocity dispersion of $\sigma < 1.5\,\mathrm{km\,s^{-1}}$ (Simon et al., 2017). Using the upper limit on σ, these authors find an upper limit on the mass enclosed within the half-light radius of $M(< R_\mathrm{h}) < 9 \times 10^4\,\mathrm{M}_\odot$ and an upper limit on the dynamical mass-to-light ratio averaged within R_h of $\langle M/L\rangle = 2M(< R_\mathrm{h})/L < 2.4 \times 10^2\,\mathrm{M}_\odot\mathrm{L}_\odot^{-1}$. We model the stellar density profile to closely resemble a Plummer sphere, i.e. $\{\alpha_\star, \beta_\star, \gamma_\star\} = \{2, 5, 0\}$ in the notation of equation 2.1. Note that a strictly cored ($\gamma_\star = 0$) stellar tracer profile cannot be embedded self-consistently in equilibrium in a cuspy ($\gamma = 1$) DM halo: Eddington inversion for such tracer - potential pairs results in DFs that do not satisfy $f(E) \geq 0$ for all energies E. In Appendix 2.B we compute the minimum central slope $\gamma_{\star,\mathrm{min}}$ of a collisionless stellar tracer embedded in a cuspy DM halo. Interestingly, the minimum slope $\gamma_{\star,\mathrm{min}}$ increases with the ratio between stellar and DM scale radius. As tidal stripping tends to increase this ratio, assuming that the stellar tracer remains spherical and isotropic, a consequence of tidal evolution is the formation of a shallow density cusp in the stellar tracer profile.

At each reconstruction of the DM density cusp, we fit a Plummer profile (allowing for a shallow density cusp, $\gamma_\star \lesssim 0.1$) to the stellar component and calculate the stellar probabilities $\mathcal{P}_\star(E)$ to match the fitted profile. Structural parameters for the embedded stellar profiles are listed in Table 2.1. Figure 2.10 shows the evolution of the stellar component for the same apocentre snapshots of the DM subhalo in Figure 2.8, distinguishing cusp reconstruction *boosts* using different colours. While initially the dwarf galaxy loses predominantly DM and its luminosity L decreases only marginally, once the stellar half-light radius R_h is of the same order as the subhalo r_max, stars get stripped efficiently. This is consistent with the findings of previous studies of the evolution of cored stellar tracers embedded in cuspy DM subhaloes using controlled

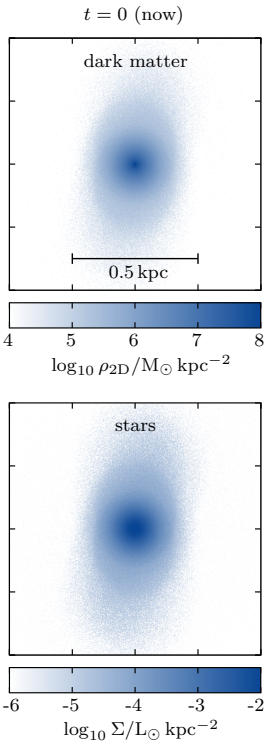

Fig. 2e: *Snapshot of the Tucana III model at $t = 0$ (now) showing the (x, y)-plane. The projected density ρ_{2D} of the dark matter distribution is colour-coded in the top panel, whereas the bottom panel shows stellar surface brightness Σ, obtained by applying the probability tagging of Eq. 2.7.*

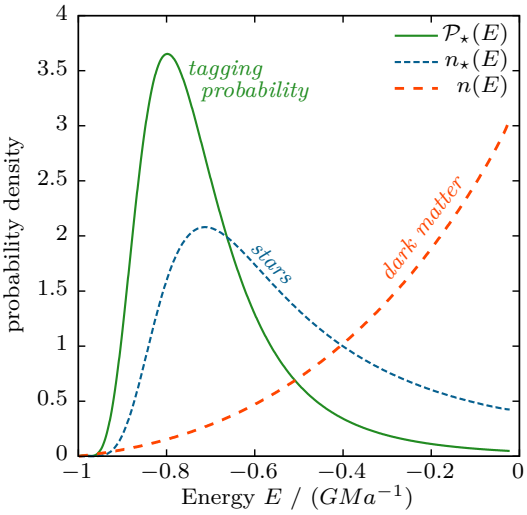

Figure 2.9: Probability $\mathcal{P}_\star(E)$ for an N-body DM particle with energy E to tag a star (equation 2.7). As an example, this is shown for differential energy distributions $n_\star(E)$ and $n(E)$ that correspond to stellar Plummer spheres and cuspy Dehnen dark matter profiles, respectively. All three functions are normalised so that their integrals over energy are equal to unity.

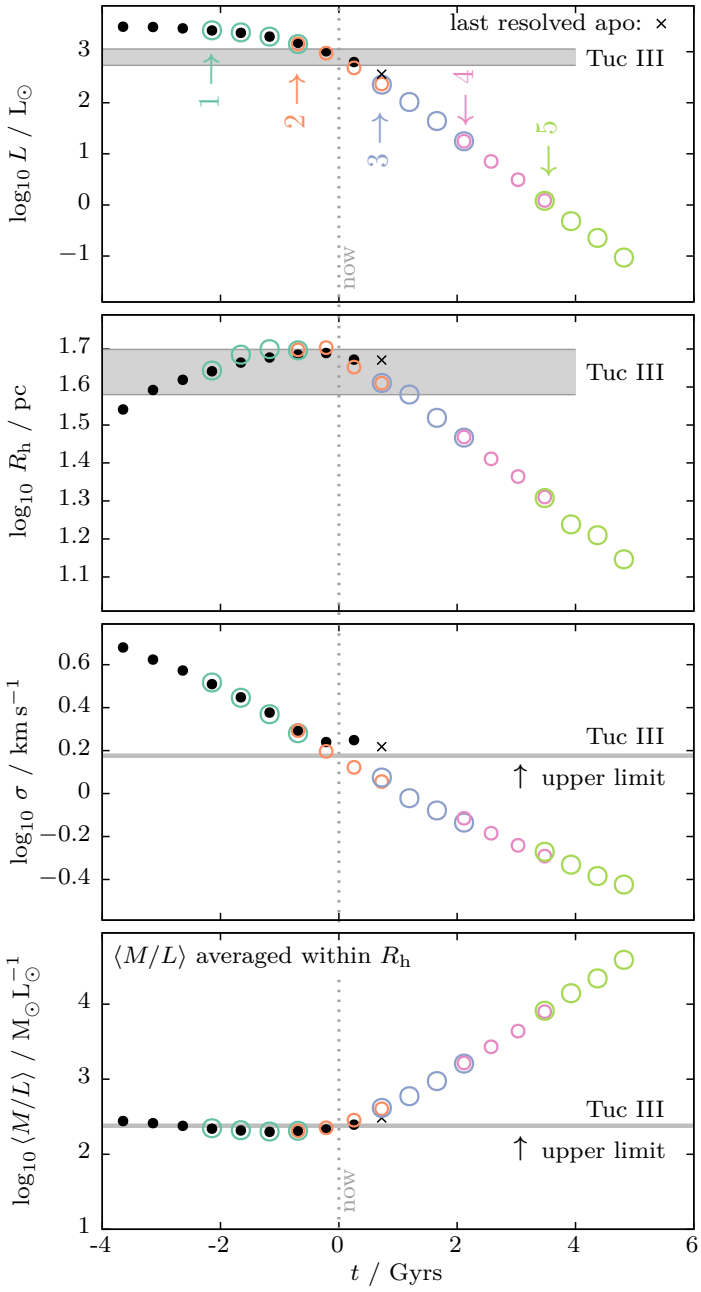

Figure 2.10: Evolution of luminosity L, half-light radius R_h, luminosity-averaged line-of-sight velocity dispersion σ and dynamical mass-to-light ratio $\langle M/L \rangle$ (averaged within R_h) of a dwarf spheroidal galaxy embedded in the cuspy DM subhalo with parameters as listed in section 2.4.1. The values of L, R_h and σ at $z = 0$ are chosen to approximate the observed properties of the Tucana III dwarf (grey bars). By periodically reconstructing the density cusp of the underlying DM subhalo, we can follow the evolution of the embedded dwarf galaxy down to sub-solar luminosities: the dwarf galaxy is not disrupted by tides. Different colours correspond to cusp reconstruction *boosts* as in Figure 2.8.

simulations with non-adaptive resolution (e.g. Peñarrubia et al., 2008b; Errani et al., 2015).

Grey shaded stripes in Figure 2.10 indicate the measured luminosity L and half-light radius $R_{\rm h}$ of the Tucana III dwarf respectively, whereas a grey solid line marks the upper limit on the measured velocity dispersion σ and dynamical mass-to-light ratio $\langle M/L\rangle$. Our N-body model is consistent with these observables at $z = 0$. Note that the dynamical mass-to-light ratio $\langle M/L\rangle$ increases during tidal evolution, reaching values as extreme as $\sim 10^4$: our assumption of stars being collisionless tracers of the underlying potential therefore holds for the modelled evolution of Tuc III. We follow the tidal evolution of the Tucana III model down to sub-solar luminosities and a luminosity-averaged line-of-sight velocity dispersion of $\sigma = \langle\sigma^2_{\rm los}\rangle^{1/2} < 0.5\,{\rm km\,s^{-1}}$. Similar to the evolution of the underlying DM subhalo, the embedded dwarf galaxy is not disrupted by tides. Abundance and detectability of such highly stripped dwarf galaxies will be discussed in the following section.

2.6 Summary and discussion

In this chapter, we argue that cold dark matter subhaloes with centrally-divergent density cusps cannot be disrupted by smooth tidal forces. There are two driving causes for the tidal survival of cuspy subhaloes:

(i) For circular orbits within cuspy subhaloes, the orbital period $t_{\rm c}(r) \to 0$ for $r \to 0$. As a consequence there is a fraction of particles within the subhalo that reacts adiabatically to perturbations by tides. Using empirical formulae for the tidal evolution of structural parameters of subhaloes obtained from controlled simulations, we show that the fraction of particles that react adiabatically increases during tidal evolution in cuspy haloes.

(ii) Furthermore with $t_{\rm c}(r)$ decreasing during tidal evolution, the cuspy subhalo has increasing multiples of its dynamical time to relax and reach equilibrium between subsequent tidal interactions.

On the other hand, for subhaloes with constant-density cores, $t_{\rm c}(r) \to {\rm const} > 0$ for $r \to 0$. Tidal evolution decreases the fraction of particles that react adiabatically to tidal perturbations in cored haloes, and with dynamical times increasing during tidal evolution, it becomes increasingly difficult for cored subhaloes to relax and reach equilibrium between subsequent tidal interactions. This facilitates the tidal disruption of cored subhaloes.

Using controlled simulations, in the spirit of van den Bosch et al. (2018), we show how insufficient numerical resolution causes the *artificial* formation of constant-density cores in numerical simulations of initially cuspy subhaloes. Under the assumption that tides do not alter the central slope $\gamma = -{\rm d}\ln\rho/{\rm d}\ln r = 1$ of cuspy subhaloes (e.g. Hayashi et al., 2003; Peñarrubia et al., 2010, and Figure 2.4 in this thesis), we

perform a numerical experiment where we periodically reconstruct the density cusp of a subhalo evolving in a Milky Way-like potential. This prevents the artificial disruption of the subhalo and allows us to follow its evolution for arbitrarily large fractions of tidally stripped mass. We furthermore study the evolution of dwarf galaxies embedded in cuspy DM haloes under the assumption that stars are collisionless tracers of the underlying potential. Using a model of the Tucana III dwarf as an example, we show that dwarf galaxies embedded in cuspy haloes can be stripped to sub-solar luminosity by tides.

2.6.1 Limitations of the model

Several aspects of our numerical experiments call for caution when drawing quantitative conclusions about the physical universe, though none of these limitations effect our main conclusion of the tidal survival of cuspy DM subhaloes.

(i) We modelled DM subhaloes as N-body realisation with isotropic velocity dispersion profiles. Cosmological simulations indicate that the central regions of DM haloes do have isotropic velocity dispersions (Navarro et al., 2010; Klypin et al., 2016), and we have verified that our tidally stripped subhalo models remain isotropic in the centre (see Figure 2.5).

(ii) When reconstructing the density cusp, we neglect the effect of extra-tidal material on the subsequent evolution of the subhalo. While extra tidal material has an effect of dynamical friction on the subhalo (Fujii et al., 2006; Fellhauer & Lin, 2007; van den Bosch & Ogiya, 2018), we find that extra tidal material does not alter the tidal evolution of the subhalo: reconstructions tailored to match the subhalo potential sourced by bound particles evolve in agreement with the original model. This is consistent with the results of controlled simulations by van den Bosch & Ogiya (2018), who find that for an initial ratio $M/M_{\rm host} \sim 1/1000$ of subhalo mass M and host mass $M_{\rm host}$, dynamical friction from tidally stripped material affects the orbital radius by a few per cent at most.

(iii) Our subhalo models are strictly collisionless. The importance of collisionality depends on the number of particles that make up the subhalo, and therefore on the mass of the smallest DM clumps, which may range from earth mass for neutralinos (e.g. Diemand et al., 2005) to the order of (multiple) solar masses for primordial black holes (e.g. Bird et al., 2016).

(iv) We furthermore model stars as massless tracers of the underlying potential. This assumption is well motivated by the large dynamical mass-to-light ratios of our models, $10^2 \lesssim \langle M/L\rangle/(M_\odot/L_\odot) \lesssim 10^4$ (averaged within the half-light radius, see Figure 2.10). Baryons embedded in DM haloes may also alter the DM halo profile through feedback (e.g. Pontzen & Governato, 2012), causing density cores

which can be tidally disrupted – though DM cusps may reform after baryonic feedback eases (Laporte & Peñarrubia, 2015).

(v) We only considered the effect of smooth tidal fields. Substructures present in the host halo, e.g. other DM subhaloes, giant molecular clouds and stars, may significantly heat up a subhalo and increase the rate of tidal stripping (Peñarrubia, 2019; Delos, 2019), although adiabatic response in inner regions may prevent full disruption (e.g. Weinberg, 1994a).

2.6.2 Detectability of stripped subhaloes and dwarf remnants

The survival of low-mass DM subhaloes has implications for potential detection through annihilation signals (e.g. Lavalle et al., 2007; Stref et al., 2019), strong gravitational lensing (e.g. Vegetti & Koopmans, 2009; Despali & Vegetti, 2017), pulsar-timing arrays (Kashiyama & Oguri, 2018; Dror et al., 2019), the number of gaps to be expected in stellar tidal streams (e.g. Ibata et al., 2002; Erkal & Belokurov, 2015), and the stochastic tidal heating of gravitating substructures (Peñarrubia, 2019).

A detailed estimate of the abundance of subhaloes stripped to sub-kpc scale lies beyond the reach of the numerical experiments discussed in the present work. However it is possible to estimate the abundance of potential progenitors to micro-galaxies with sub-solar luminosities from the re-simulations of the Aquarius A2 merger tree introduced in chapter 3. Those re-simulations follow the tidal evolution of the $\sim 10^3$ cuspy subhaloes which at the peak of their mass evolution reached a mass $M \geq 10^8\,\mathrm{M}_\odot$, sufficiently massive to allow star formation (Gnedin, 2000). In presence of a galactic disc, at redshift $z = 0$, of the order of ~ 200 subhaloes were stripped to masses below the resolution limit of the re-simulation $M \lesssim 5 \times 10^5\,\mathrm{M}_\odot$. In light of the results of this study, these subhaloes may host bound visible remnants, and may therefore constitute progenitors to micro-galaxies.

How can dwarf galaxy remnants be distinguished from other clusters of stars? The tidal evolution of our model of the Tucana III dwarf galaxy results in a co-moving group of stars of sub-solar total luminosity, embedded in a cuspy DM halo. Its structural properties evolve away from those of classical dwarf galaxies and globular clusters (see Figure 2.11). Neglecting effects of mass segregation, dwarf galaxy remnants with sub-solar luminosity will have been stripped of all their more massive (i.e. less numerous) stars, with most stars populating the low-luminosity tail of the main sequence. A PARSEC isochrone (Bressan et al., 2012) for a metallicity of $[\mathrm{Fe/H}] = -2.4\,\mathrm{dex}$ and an age of 10.9 Gyrs (Drlica-Wagner et al., 2015; Simon et al., 2017), approximating the stellar population of the Tuc III, is shown in Figure 2.12. The relative abundance of stars is colour-coded, highlighting that 90 per cent of stars are located below the main-sequence turnoff. At a mean luminosity per star of $\langle L_\star \rangle / \mathrm{L}_\odot \approx 0.25$, co-moving groups of total sub-solar luminosity may contain only a handful of stars.

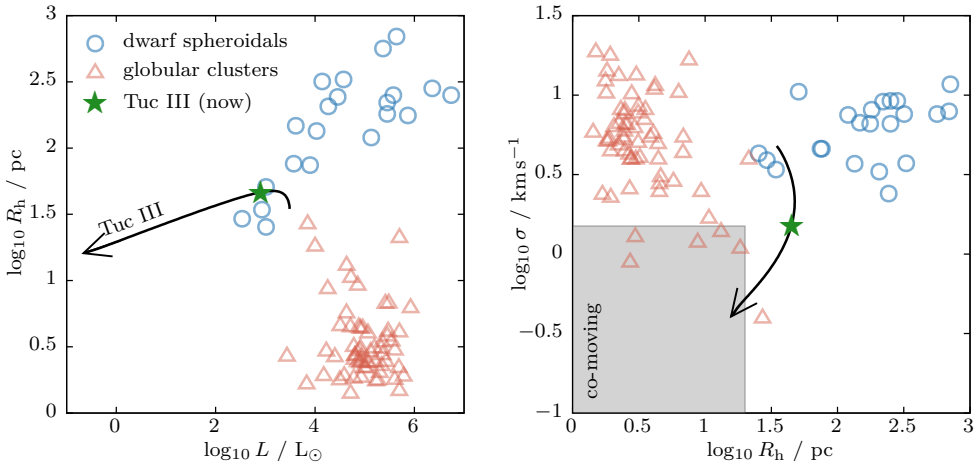

Figure 2.11: Evolution of the Tuc III model compared to luminosities L, half-light radii R_h and velocity dispersions σ of a sample of Milky Way dwarf galaxies (from McConnachie 2012 with the additions as listed in Table 4.2, p. 90) and globular clusters (from Harris, 1996, 2010 revision). An evolved dwarf remnant would appear as a co-moving group of stars with a half-light radius compatible with those of globular clusters but much lower luminosity and velocity dispersion. The grey shaded area in the right panel marks the range of stellar separations and dispersions of co-moving stellar pairs that are likely to have formed together (Kamdar et al., 2019).

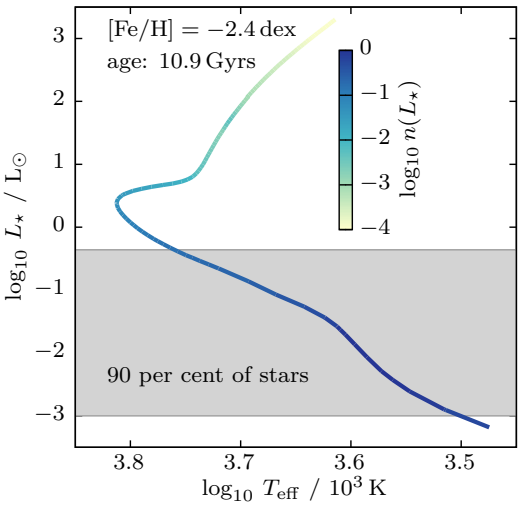

Figure 2.12: PARSEC isochrone (Bressan et al., 2012) for a metallicity of [Fe/H] = −2.4 dex and an age of 10.9 Gyrs, approximating the stellar population of the Tucana III dwarf (Drlica-Wagner et al., 2015; Simon et al., 2017). The relative abundance $n(L_\star)$ of stars with luminosity $L_\star$ is colour-coded, highlighting that 90 per cent of stars are located below the main-sequence turnoff.

Recently, Kamdar et al. (2019) have shown using simulations that (pairs of) stars with separations of $\Delta r < 20\,\mathrm{pc}$ and $\Delta v < 1.5\,\mathrm{km\,s^{-1}}$ are likely to have formed together, and identified 111 co-moving pairs using *Gaia* data. They conclude that co-moving stars originate preferentially from star clusters younger than 1 Gyr – such co-moving pairs should therefore have notably higher metallicities than dwarf galaxy remnants. With large dynamical mass-to-light ratios of $10^3 \sim 10^4\,\mathrm{M_\odot/L_\odot}$ predicted for dwarf galaxy remnants, accurate kinematics for such systems would allow to constrain the presence of a DM subhalo surrounding a co-moving group of stars. Given the predicted low velocity dispersions $\sigma \lesssim 1\,\mathrm{km\,s^{-1}}$, below the dispersion background caused by binaries (McConnachie & Côté, 2010), accurate velocity dispersions measurements may prove to be technically challenging. Seminal work by Koposov et al. (2011) however has demonstrated that accurate stellar kinematics can also be obtained for dwarf galaxies with velocity dispersions of the order of $\mathrm{km\,s^{-1}}$ by repeated measurements of single-star velocities, reducing single-star velocity errors to values as low as $0.2\,\mathrm{km\,s^{-1}}$. Furthermore on a statistical basis, the search for extended ($\sim 10^1$ pc) co-moving groups of stars with low metallicity and low velocity dispersion in the Milky Way halo may constitute a promising way to test the existence of *micro-galaxies* predicted by CDM.

Appendix to Chapter 2

2.A Sizes of artificial density cores

N-body realisations of cuspy density profiles form *artificial* constant-density cores in their centres when evolved in isolation using particle mesh codes (see section 2.3). In the following, we fit analytical density profiles to evolved N-body models to relate the spatial resolution Δx of the particle mesh code to the size r_c of the artificial density core. For this purpose, we generate an N-body realisation of a cuspy Dehnen (1993) profile ($\{\alpha, \beta, \gamma\} = \{1, 4, 1\}$ in Eq. 2.1) with $N = 10^7$ particles, total mass $M = 10^8\,\mathrm{M}_\odot$ and scale radius $r_s = 1\,\mathrm{kpc}$, using the technique described in section 2.3.1. This density profile can also be written in the functional form of a generalised Hernquist profile $\rho(r) = \rho_s\, r_s^4\, (r + r_c)^{-1}\, (r + r_s)^{-3}$ (equation 1.51, page 25) with core size $r_c = 0$. Using the particle mesh code SUPERBOX (Fellhauer et al., 2000) (described in section 1.5), we evolve the N-body model in isolation for 1 Gyr, with a time step of $\Delta t = 1\,\mathrm{Myr}$ and a particle mesh with 128^3 high-resolution grid cells. We run two simulations, with a grid cell size of $\Delta x = 0.2\, r_s$ and $0.1\, r_s$, respectively. Figure 2.A.1 below shows the evolved N-body models for the two simulations, as well as generalised Hernquist profiles with core sizes r_c chosen to match the evolved N-body models. A choice of $r_c \approx \Delta x / 2.5$ matches the evolved N-body models well for both simulations.

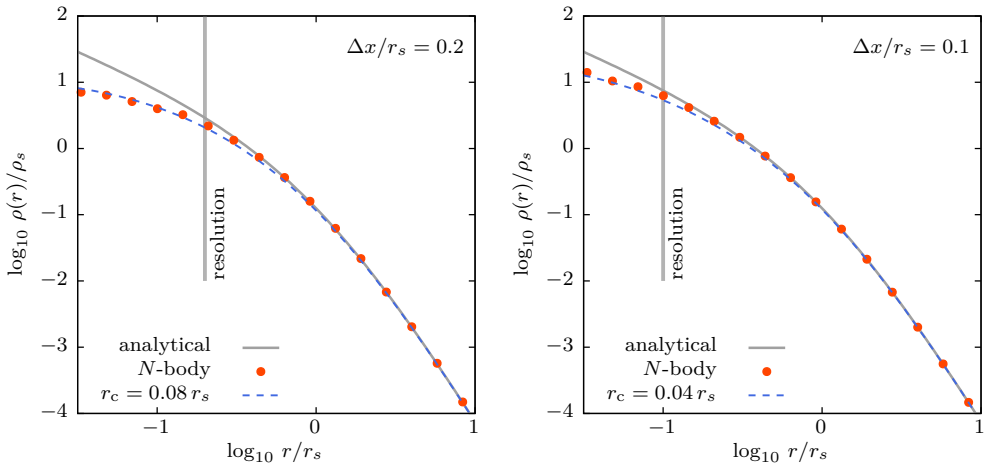

Figure 2.A.1: N-body realisations of Dehnen (1993) density profiles with scale radius r_s (solid grey curve) form artificial density cores when evolved in isolation using a particle mesh code of resolution Δx (filled red circles). Generalised Hernquist profiles (Eq. 1.51, p. 25) with core size $r_c \approx \Delta x / 2.5$ match the evolved N-body models well (blue dashed curve) for simulations with $\Delta x = 0.2\, r_s$ (left panel) and $\Delta x = 0.1\, r_s$ (right panel).

2.B Stellar density cusps in cuspy haloes

In the present study, we treat stars as collisionless tracers of the underlying dark matter potential. We consider potentials sourced by spherical cuspy density distributions, i.e. distributions for which $\gamma = -\mathrm{d}\ln\rho/\mathrm{d}\ln r > 0$ for $r \to 0$. We focus on the particular case of $\gamma = 1$, motivated by the Navarro et al. (1996) density distribution for dark matter haloes. Stellar density distributions are frequently approximated by a Plummer profile, $\{\alpha_\star, \beta_\star, \gamma_\star\} = \{2, 5, 0\}$ in the notation of equation 2.1. This is a cored density profile as $\mathrm{d}\ln\rho/\mathrm{d}\ln r \to 0$ for $r \to 0$. For systems with isotropic velocity dispersion, the distribution function $f(E)$ of such a (cored) stellar tracer embedded in a (cuspy) dark matter profile does not satisfy $f(E) \geq 0$ for all energies E: a cored stellar tracer embedded in cuspy dark matter profile cannot be realized as an equilibrium configuration. Allowing for a shallow density cusp $\gamma_\star$ in the tracer distribution alleviates this problem.

What is the minimum central slope $\gamma_\star$ of a stellar tracer embedded in a cuspy dark matter halo? We address this question for spherical tracer distributions with isotropic velocity dispersion. In particular, we compute the minimum central slope $\gamma_\star$ of a stellar tracer with $\{\alpha_\star, \beta_\star, \gamma_\star\} = \{2, 5, \gamma_\star\}$ density profile embedded in a dark matter halo with $\{\alpha, \beta, \gamma\} = \{1, \beta, 1\}$ density profile for different outer slopes β. For this purpose, we use Eddington inversion to calculate the distribution function $f(E)$ corresponding to a given tracer and dark matter density profile (see section 2.3.1). Physical distribution functions satisfy $f(E) \geq 0$ for all energies E.

Figure 2.B.1 shows the minimum central slope $\gamma_\star$ necessary to satisfy $f(E) \geq 0$ for all E of a stellar tracer embedded in a cuspy dark matter halo for different choices of the outer slope $\beta = (4, 5, 6)$. The minimum central stellar slope $\gamma_\star$ is plotted as a function of segregation $a_\star/a$, parametrising how deeply embedded the stellar tracer distribution is within the dark matter halo, expressed as the ratio of tracer scale radius $a_\star$ and dark matter scale radius a. As a point of reference, note that the projected half-light radius R_h of a Plummer profile is equal to the profile scale radius $a_\star$. The minimum slope $\gamma_\star$ increases with the ratio $a_\star/a$ between stellar and dark matter scale radius. As tidal stripping tends to increase this ratio (see Table 2.1), assuming that the stellar tracer remains spherical and isotropic, a consequence of tidal evolution is the formation of a shallow density cusp in the stellar tracer profile.

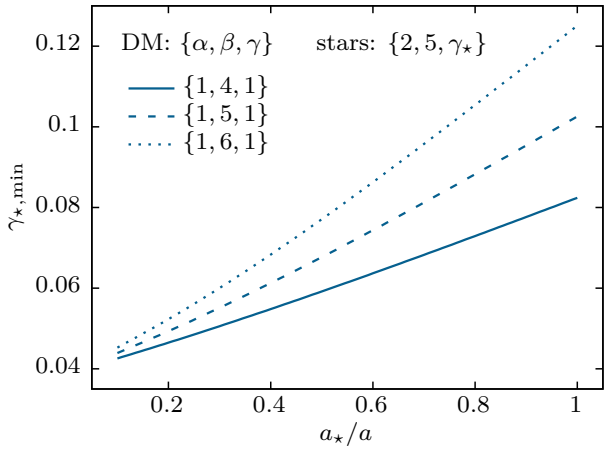

Figure 2.B.1: Minimum value $\gamma_{\star,\min}$ of the central slope $\gamma_\star = -\mathrm{d}\ln\rho_\star/\mathrm{d}\ln r$, $r \to 0$ for collisionless stellar tracers with $\{\alpha_\star, \beta_\star, \gamma_\star\} = \{2, 5, \gamma_\star\}$ profile embedded in equilibrium in cuspy $\{\alpha, \beta, \gamma\}$ DM haloes. The minimum slope is shown as a function of *stellar segregation*, expressed as the ratio of stellar scale radius $a_\star$ and dark matter scale radius a (in the notation of equation 2.1). For slopes shallower than $\gamma_{\star,\min}$, the distribution function for systems with isotropic velocity dispersion does not satisfy $f(E) \geq 0$ for all energies E.

Chapter 3

Depletion of substructures

Abstract

We use high-resolution N-body simulations to study the effect of a galactic disc on the dynamical evolution of dark matter subhaloes with orbits and structural parameters extracted from the Aquarius A-2 merger tree (Springel et al., 2008). Subhaloes are modelled as equilibrium N-body realizations of generalized Hernquist profiles with 2×10^6 particles and injected in the analytical evolving host potential at redshift $z_{\rm infall}$, defined by the peak of their mass evolution. We select all subhaloes from the A-2 merger tree with $M_{200}(z_{\rm infall}) \geq 10^8\,{\rm M}_\odot$ and first pericentric distances $r_p < r_{200}$. Motivated by observations of Milky Way dwarf spheroidal galaxies, we explore subhalo models with both cuspy and cored dark matter profiles with a relative core size of $r_c = 0.8\,a_s$, where a_s denotes the Hernquist scale radius. We find that cuspy models have twice as many resolved subhaloes at redshift $z = 0$ than their cored counterparts, and four times as many if we only consider those on orbits with $r_p \lesssim 0.1\,r_{200}$. For a given subhalo density profile, adding an evolving disc to the host potential reduces the number of substructures further by a factor of $\lesssim 2$ for subhaloes on orbits which penetrate the disc ($r_p \lesssim 20\,{\rm kpc}$). For large r_p, where tidal forces and the effect of the disc become negligible, the number of subhaloes per pericentre bin converges to similar values for all four models.

This chapter has been published in MNRAS 465, L59-L63 (2017) (RE, J. Peñarrubia, C.F.P. Laporte & F. Gómez: The effect of a disc on the population of cuspy and cored dark matter substructures in Milky Way-like galaxies, arXiv:1608.01849). Appendix 3.A has been added to this thesis as a more technical summary of the developed simulations.

3.1 Introduction

Despite the success in modelling dark matter (DM) structure formation on large scales, the clustering properties of DM on galactic scales are fiercely debated. The number of observed dwarf galaxies around the Milky Way (MW) is lower by many orders of magnitude than the number of *cold* dark matter (CDM) substructures predicted by cosmological simulations - e.g. Moore et al. (1999) predict a number of CDM substructures with bound mass $\gtrsim 10^8\,{\rm M}_\odot$ larger by a factor 50 than the number of observed MW satellites in this mass range, and Diemand et al. (2005) predict a total of 10^{15} surviving CDM subhaloes down to the mass determined by the free-streaming length ($\sim 10^{-6}\,{\rm M}_\odot$), see chapter 1.2.1 . Within the CDM paradigm this can be explained by a suppression of galaxy formation in low-mass DM haloes, through the

combined effect of inefficient cooling of gas during HI re-ionization by UV photo heating (Bullock et al., 2000; Gnedin, 2000; Benson et al., 2002) and supernova feedback (e.g. Dekel & Silk, 1986) leading to DM haloes that do not contain any stars. Alternatively DM particle properties, such as low-mass *warm* DM (e.g Lovell et al., 2014), can lead to a suppression of the small-scale power resulting in a reduction of substructures in galactic haloes. Likewise the presence of a galactic disc enhances the disruption rate of substructures (e.g. D'Onghia et al., 2010; Peñarrubia et al., 2010) and alters the amount of surviving substructures. Several methods have been proposed to detect dark matter substructures, including those that do not host stars, e.g. through surface brightness reconstruction of strong lensing arcs (Vegetti & Koopmans, 2009), the heating of tidal streams (e.g. Ibata et al., 2002), or the disruption of wide binaries in dSph galaxies (Peñarrubia et al., 2016b) - these efforts still remain unsuccessful to date.

The inner structure of DM haloes is strongly linked to the number of DM substructures lingering in MW-like galaxies. The efficiency of tidal stripping inside the host halo depends on the inner density distribution of the satellites. In particular, dwarf galaxies embedded within DM haloes with constant-density *cores* are less resilient to tidal disruption than those embedded within centrally-divergent *cuspy* haloes (see Peñarrubia et al. 2010, and thesis chapter 2). While the density profiles of haloes in DM-only simulations are well fit by the cuspy *NFW* profile (Navarro et al., 1997), contradicting results based on the observations of MW satellites have provoked a critical debate on whether dwarf galaxies are cuspy (Richardson & Fairbairn 2014), or cored (Walker & Peñarrubia 2011, Amorisco & Evans 2012, Amorisco et al. 2013), whereas dynamical modelling of local dwarf galaxies argues in favour of a range of cuspy and cored profiles (Oman et al., 2015). In addition, none of the observed bright MW satellites ($L_V > 10^5\,\mathrm{L}_\odot$) has an estimated mean density within the stellar half-light radius consistent with the most massive cuspy subhaloes predicted by cosmological simulations (Boylan-Kolchin et al., 2011). Different processes such as gravitational heating by baryonic clumps (e.g. Nipoti & Binney, 2015) and supernova feedback (e.g. Navarro et al., 1996; Read & Gilmore, 2005; Pontzen & Governato, 2012) have been proposed to remove the density cusp from the centres of dwarf galaxies, see chapter 1.2.1. However, recent studies taking into account the effects of tidal stripping on baryonic clumps show significantly milder changes to the central DM density slopes (Laporte & White, 2015). Similarly, simple analytic energy arguments suggest that supernova feedback only affects the brightest dwarfs (Peñarrubia et al., 2012), although stochastic star formation in low-mass haloes may help to ease the energetic constraints (Read et al., 2016). Furthermore, within CDM, erased cusps may still regrow through minor mergers (Laporte & Peñarrubia, 2015). Alternative DM particle models which allow for a large enough cross-section for self-interaction (e.g. Spergel & Steinhardt, 2000) or a small enough DM particle mass (e.g. Tremaine & Gunn, 1979) could prevent cusps to form. Yet, Macciò et al. (2012) argue that a particle mass small enough

to produce core sizes of $r_c \sim 1\,\mathrm{kpc}$, as measured e.g. for the Fornax dwarf galaxy (Amorisco et al., 2013), is in contradiction to the constraints set by the large scale structure and would prevent the dwarf galaxy to form in the first place. Other studies suggest that ultra-light axions may solve the missing satellites and cusp/core problems simultaneously (Hu et al., 2000).

In this chapter, we examine the tidal effect of an evolving galactic disc on the survival of DM substructures in MW-like haloes. We are particularly interested in the different dynamical evolution of satellites with respect to their internal DM density profile. Our contribution follows up the work of D'Onghia et al. (2010) who re-simulated the Aq-A-2 halo merger tree with an added analytical disc and found that the presence of a disc enhances the tidal disruption of substructures. More recent studies by Yurin & Springel (2015), who inserted N-body discs in the Aq-A-5 to H-5 haloes, and Zhu et al. (2016), who compared DM-only to full-hydrodynamical simulations of the Aq-C-4 main halo, show similar results. Motivated by the approach of Bullock & Johnston (2005), we perform controlled simulations which follow the evolution of individual satellites extracted from the Aquarius Aq-A-2 merger tree (Springel et al., 2008) in an analytical, evolving host halo, where we change single parameters at a time and quantify their effect on the surviving satellite population.

This chapter is structured as follows: Section 3.2 describes our re-simulation technique and the numerical models for the evolving host and satellite galaxies. We present the results of our controlled simulations in section 3.3, and finally discuss our findings in section 3.4.

3.2 Numerical Method

The controlled simulation setup used in this chapter is based on the merger history of the Aquarius A-2 run (Springel et al., 2008). The Aq-A-2 run uses a particle mass of $m_p = 1.37 \times 10^4\,\mathrm{M}_\odot$ and $\sim 5.32 \times 10^8$ high-resolution particles in total, with a gravitational softening length of $\epsilon = 65.8\,\mathrm{pc}$, and leads to the formation of a MW-like main halo of virial radius $r_{200} = 246\,\mathrm{kpc}$ and mass $M_{200} = 1.84 \times 10^{12}\,\mathrm{M}_\odot$.

Host galaxy: We model the DM halo of the host galaxy using a spherical Navarro et al. (1997) profile. The time evolution of the NFW halo follows the analytically motivated functions of Buist & Helmi (2014), fitted to the Aq-A-2 main halo. Assuming a Maxwellian distribution of velocities, we approximate the effect of dynamical friction through the Chandrasekhar (1943) model (see chapter 1.3.1). We compare the orbital decay induced by our semi-analytical model to the orbits of selected satellites in the Aq-A-2 simulation, and find that a Coulomb-logarithm of $\ln \Lambda = 2.2$ reproduces the Aquarius results well, consistent with the findings of Velazquez & White (1999). Models including a disc consist of an additional axisymmetric Miyamoto & Nagai (1975) profile, with radial and vertical scale lengths $a_d = 3.5\,\mathrm{kpc}$ and $b_d = 0.3\,\mathrm{kpc}$ and mass $M_d = 0.1\ M_{200}(z)$, where we denote by $M_{200}(z)$ the virial mass of the NFW

halo at redshift z. To model dynamical friction in the presence of a disc, for simplicity we require at every radius an isotropic distribution of velocities in a reference frame corotating with the disc, with dispersion and rotation velocity as in Nagai & Miyamoto (1976, equations 34 and 38) and use the same Maxwellian model of dynamical friction as for the halo. We keep the joint mass of the disc and halo equal to the Aq-A-2 halo mass at each redshift. This choice of adding a disc potential does not alter the distribution of galactocentric distances of the satellite's first pericentric passages (see green curves in Fig. 3.3). Subsequent pericentric distances are smaller in the models including a disc: orbits decay faster due to the increased dynamical friction inside the disc, and the re-distribution of orbital energy to tidally stripped material becomes more important with the increased mass loss in the models including a disc.

Accreted satellites: We extract positions, velocities and masses from the Aq-A-2 merger tree for all satellites with $M_{200} \geq 10^8\,\mathrm{M}_\odot$ (960 in total). About and below this mass scale, the heating of the intergalactic medium during HI re-ionization prevents gas from cooling, and no stars form (Gnedin, 2000). Substructures accreted in groups are modelled as individual satellites for simplicity. We use the median Prada et al. (2012) relation to estimate the scale radii of the accreted satellites as a function of their mass, which range from 0.6 kpc at $10^8\,\mathrm{M}_\odot$ to 8.8 kpc for the most massive satellite with $7.3 \times 10^{10}\,\mathrm{M}_\odot$. In the same spirit as Bullock & Johnston (2005), we model each satellite with a fixed number of 2×10^6 particles independent of its mass. This allows us to follow the stripping and dynamical evolution of lower mass substructures more reliably than achieved by simulations with fixed particle mass[3]. We create equilibrium N-body realizations drawn from a modified Hernquist (1990) profile with DM scale radius a_s and core size r_c:

$$\rho(x) = \frac{\rho_c}{(x+c)\,(x+1)^3}, \text{ where } c = \frac{r_c}{a_s}\ ,\ x = \frac{r}{a_s}\ . \tag{3.1}$$

We translate the scale radii of NFW profiles to cuspy Hernquist profiles ($c = 0$) noting that $\partial \ln \rho(x)/\partial \ln x = -2$ for $x = 1/2$. We choose a fixed relative core size of $r_c = 0.8\,a_s$, where the order of magnitude of this value is motivated by the estimates of DM scale radius $a_s \sim 1.4$ kpc (Peñarrubia et al., 2008b) and core size $r_c = 1^{+0.8}_{-0.4}$ kpc (Amorisco et al., 2013) for the Fornax dSph galaxy. Different DM particle and feedback models suggest a range of values of relative or absolute core size - for simplicity, we choose a constant ratio r_c/a_s for the entire satellite population (see discussion). The N-body models are injected into the host potential at z_{infall}, defined by the peak of their mass evolution, i.e. before they lose mass due to tidal stripping. The tidal interaction of the satellites with the host is simulated individually, i.e. encounters between satellites are neglected.

PM code: We follow the evolution of the N-body models in the tidal field of the host galaxy with the particle mesh code SUPERBOX (Fellhauer et al. 2000, see thesis chapter 1.5) which samples the density of each satellite to three cubic grids

[3] *This numerical setup was developed prior to the cusp-reconstruction method introduced in chapter 2 of this thesis. While the setup described here is tailored to resolve all subhaloes with the same relative resolution independent of their mass at infall, the simulations are still limited by the number of N-body particles resolving each subhalo, and by the spatial resolution of the particle mesh.*

with different resolution and performs a leapfrog integration to solve the equation of motion. The three grids help to account for the large dynamic range in density between the satellites and the tidally stripped material. Each grid consists of 64^3 cubic cells. Grids 1 and 2 move with the centre of density of each satellite, while grid 3 is centred on the host galaxy. Grid 1 (2, 3) resolves the core of the satellites with a resolution Δx of $2a_s/64$ ($20a_s/64$, 1 Mpc/64). For the least extended subhalo with scale radius $a_s = 0.6\,\mathrm{kpc}$ this translates to $\Delta x \approx 0.019\,\mathrm{kpc}$, whereas for the most extended subhalo with $a_s = 8.8\,\mathrm{kpc}$, $\Delta x \approx 0.28\,\mathrm{kpc}$. As the self-gravity of the stripped material is not significant for its evolution, the relatively low resolution of the outermost grid does not have any significant impact on our analysis. We use a time step of $\Delta t = \min(t_c(a_s)/400,\ 1\,\mathrm{Myr})$, where t_c is the period of a circular orbit at a_s. All models are run in isolation for 14 Gyrs in order to test the stability of our numerical set-up, and the profiles are stable within the resolution limits of grid 1. We adopt the same cosmological parameters as the Aquarius project, i.e. $\Omega_m = 0.25$, $\Omega_\Lambda = 0.75$ and $h = 0.73$.

3.3 Controlled simulations

In this section, we study the effect of an axisymmetric disc on the abundance of DM substructures at $z = 0$. We model the accretion on to the host halo separately for the case of satellites with cuspy and cored DM profiles. Fig. 3.1 shows the average squared DM density at $z = 0$ for a host galaxy consisting of a spherical NFW halo compared to a host galaxy with an added axisymmetric disc. Results obtained with a cuspy and a cored satellite population are shown in the left and right panels, respectively. The number of resolved substructures decreases for the models in the order *'cusp - no disc'*, *'cusp - disc'*, *'core - no disc'*, *'core - disc'*, and the difference between the models is more pronounced in the central regions of the galaxy.

To characterize the properties of the resolved satellites at redshift $z = 0$, we fit spherical Hernquist profiles to the particles of each individual satellite, about the centre of density as determined by SUPERBOX. We perform iterative fits, removing particles lying further out than twice the fitted scale radius to reduce the impact of tidally stripped material on the fit parameters, and leave the outer slope of the profile as a free parameter to account for a steeper drop in density induced by tidal stripping (see Peñarrubia et al., 2010, and Figure 2.4 in this thesis). Only those fitted profiles which have a central density larger than the background density are considered to be surviving substructures, and we only consider satellites which have a first pericentric radius $r_p < r_{200}(z = 0)$. We find that the satellite DM profiles are altered by tides predominantly in the outskirts, consistent with the findings of Peñarrubia et al. (2010). The evolution of the profile parameters follows *tidal tracks* (i.e. mono-parametric functions which only depend on the fraction of mass lost to tides) close to those of Peñarrubia et al. (2010).

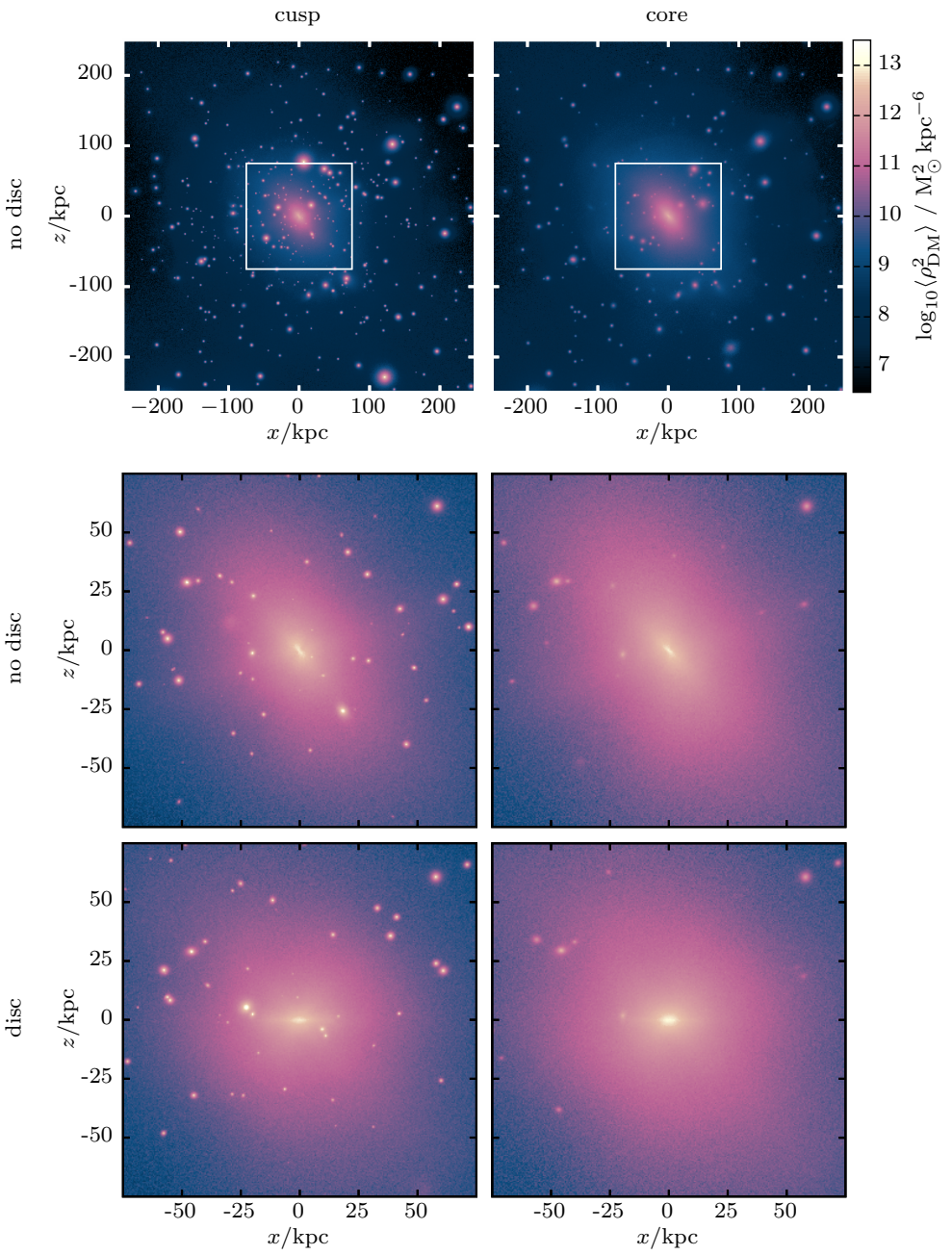

Figure 3.1: Average squared DM densities at $z = 0$ for re-simulations of the Aq-A-2 merger tree for cuspy (left) and cored (right) satellite models. The top (central) row shows panels of width 500 kpc (150 kpc) for a spherical host halo, while the bottom row shows (edge-on) simulations that include a galactic disc. The density is evaluated in cubic cells of width 1 kpc (0.5 kpc) for the 500 kpc (150 kpc) panels.

The top panel of Fig. 3.2 shows that the number $N(< M)$ of resolved substructures at $z = 0$ for each given mass M is larger for the cuspy models compared to the cored models, and larger for the models without disc compared to those with an added disc. Note that we do not identify any surviving cored substructures at $z = 0$ with $M \lesssim 2.5 \times 10^6\,\mathrm{M}_\odot$. Substructures with $M \lesssim 10^8\,\mathrm{M}_\odot$ at $z = 0$ predominantly originate from accreted satellites with masses of $10^8 \sim 10^9\,\mathrm{M}_\odot$ at z_infall on orbits with $r_p \lesssim 50\,\mathrm{kpc}$. Cored satellites, having a shallower gravitational potential at fixed M_{200}, are less resilient to tidal stripping and lose more mass for a fixed number of pericentric passages than their cuspy counterparts (see Peñarrubia et al., 2010, Fig. 3). For the models with added disc, the strong gradient in density perpendicular to the disc plane causes increased tidal forces on the satellites, which in turn get stripped more efficiently. In the bottom panel of Fig. 3.2, we show that for $M \gtrsim 10^7\,\mathrm{M}_\odot$, the shape of the mass spectrum $\mathrm{d}N/\mathrm{d}\log_{10}(M/\mathrm{M}_\odot)$ of the resolved substructures does not change between the models, but the normalization decreases, consistently with

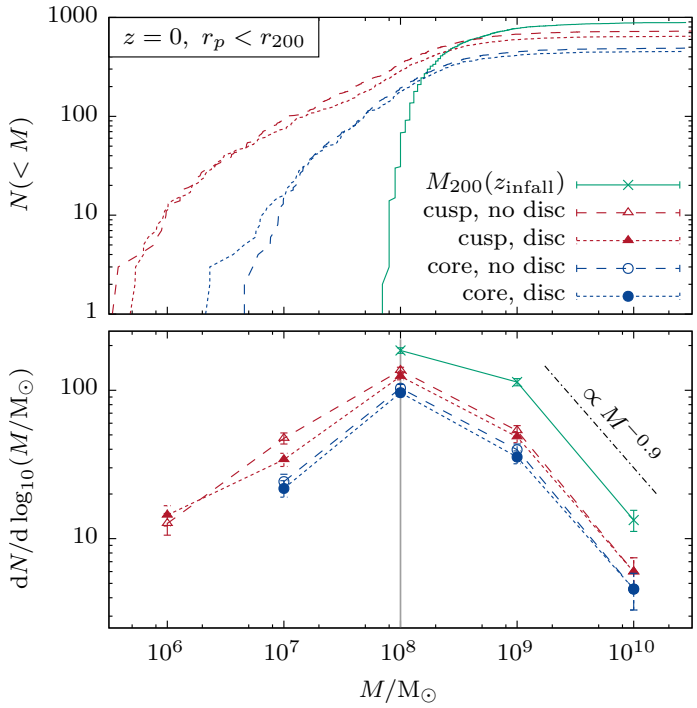

Figure 3.2: *Top panel:* number $N(< M)$ of resolved substructures with mass $< M$ at $z = 0$. The masses have been obtained by fitting iteratively Hernquist profiles to the particles of each individual satellite. The green solid line shows $N(< M_{200})$ at z_infall. *Bottom panel:* number $\mathrm{d}N/\mathrm{d}\log_{10}(M/\mathrm{M}_\odot)$ of substructures in five logarithmic mass bins, with Poisson errorbars. We do not show bins containing less than 1 per cent of the satellite galaxy population. Note the cut-off in the initial conditions for $M_{200} < 10^8\,\mathrm{M}_\odot$. The dash-dotted slope $\propto M^{-0.9}$ corresponds to the halo abundance found in DM-only simulations, $\mathrm{d}N/\mathrm{d}\log_{10} M \propto M\,\mathrm{d}N/\mathrm{d}M$ with $\mathrm{d}N/\mathrm{d}M \propto M^{-1.9}$ (see equation 1.1, page 3).

the visual impression of Fig. 3.1. Models with cored satellites have ~ 2 times less substructures than their cuspy counterparts, and models including a galactic disc have ~ 20 per cent less substructures on orbits with pericentre distances $r_{\rm p} < r_{200}$ compared to models without a disc.

To further examine the process driving the depletion of substructures, we study the abundance of substructures as a function of the galactocentric distance r_p of their first pericentric passage. The top panel of Fig. 3.3 shows that the number $N(< r_p)$ of resolved substructures at each given r_p is larger for the cuspy models compared to the cored models, and larger for the models without disc compared to those with an added disc. There are no cored substructures with $r_p \lesssim 8\,\mathrm{kpc}$. As the tidal forces increase towards the galactic centre, satellites with pericentric distances within a couple of disc scale radii a_d lose mass more efficiently. Adding to this, satellites with small r_p are generally accreted at earlier redshifts and went through more pericentre passages along their orbits. This explains the reduced number of substructures at small r_p, while satellites with large r_p went through fewer pericentric passages during which they experienced weaker tidal forces. The bottom panel of Fig. 3.3 shows

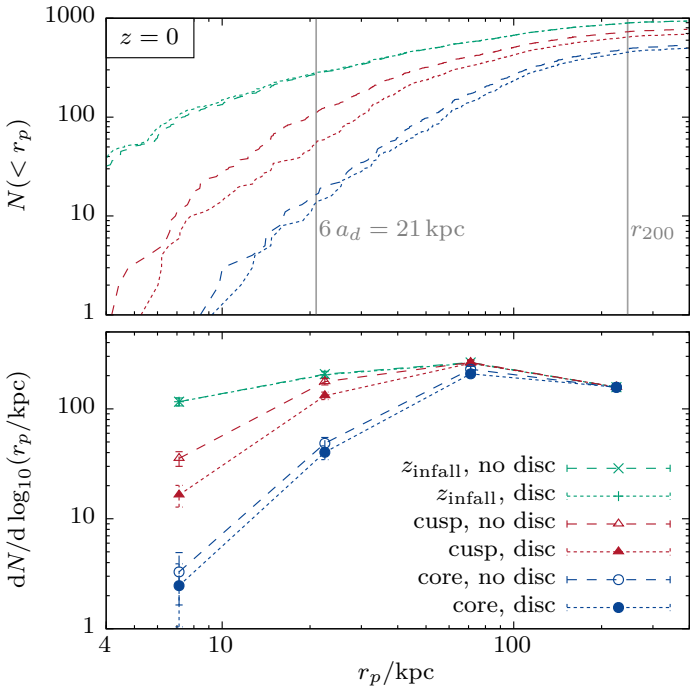

Figure 3.3: *Top panel:* number $N(< r_p)$ of resolved substructures with galactocentric distance of the first pericentre $< r_p$ at $z = 0$. The green curves show $N(< r_p)$ at $z_{\rm infall}$ for models with and without a disc, identical for cuspy and cored models. A radius of 21 kpc, equal to six times the horizontal disc scale length $a_d = 3.5\,\mathrm{kpc}$, and the virial radius $r_{200} = 246\,\mathrm{kpc}$ are denoted by solid vertical lines. *Bottom panel:* number $\mathrm{d}N/\mathrm{d}\lg(r_p/\mathrm{kpc})$ of substructures in four logarithmic pericentre bins, with Poisson errorbars.

the number $\mathrm{d}N/\mathrm{d}\lg(r_p/\mathrm{kpc})$ of resolved substructures in four logarithmic bins of pericentric distance r_p. For large r_p, where tidal forces and the effect of the disc become negligible, the number of satellites per pericentre bin converges to similar values for all four models. In contrast the difference between the models is largest for satellites on orbits which penetrate the disc, i.e. $r_p \lesssim 6\,a_d$ (factor ~ 4 between cuspy and cored models, factor $\lesssim 2$ between models with and without disc).

3.4 Summary and discussion

In this chapter, we studied the effect of a galactic disc on the abundance of cuspy and cored DM substructures in an evolving MW-like halo. We re-simulated the Aquarius Aq-A-2 merger tree by following the evolution of individual satellites, modelled as equilibrium N-body realizations of generalized Hernquist profiles with a fixed number of 2×10^6 particles and injected in the host potential at the peak of their mass evolution. We show that models with cuspy satellites have twice as many substructures at $z=0$ than their cored counterparts for pericentres $r_p < r_{200}$, and four times as many for $r_p < 0.1\,r_{200}$. Adding an evolving axisymmetric disc of mass $0.1\,M_{200}(z)$ and radial scale length $a_d = 3.5\,\mathrm{kpc}$ to the potential reduces the number of both cuspy and cored substructures further by a factor $\lesssim 2$ for satellites on orbits which penetrate the disc, and by ~ 20 per cent for the entire population. Remarkably, we find a factor ~ 8 depletion in the number of cored substructures which penetrate the disc with respect to their cuspy counterparts evolving in a DM-only halo without a disc. Our results on the depletion of substructures due to the disc are in good agreement with the findings of previous studies: D'Onghia et al. (2010, cf. Fig. 3) show a depletion by a factor of ~ 2 for satellites with $M \sim 10^9\,\mathrm{M}_\odot$ located at $z=0$ within the inner 30 kpc of a MW-like halo, whereas Yurin & Springel (2015, cf. Fig. 18) and Zhu et al. (2016, cf. Fig. 4) find a depletion of the order of ~ 30 per cent for the entire population. Later studies result consistent with our findings as well: Sawala et al. (2017) show that cosmological simulations including baryons have less substructures by a factor of ~ 2 compared to dark matter-only simulations, with substructure depletion increasing towards the galactic centre. Garrison-Kimmel et al. (2017) find a similar factor of ~ 2 for the depletion of substructures within the inner 100 kpc of the host halo, whereas Richings et al. (2018) find a depletion of ~ 20 per cent for the entire population of subhaloes, and a factor of ~ 2 in the central regions of the host halo.

Although the re-simulation technique is computationally highly efficient, several aspects of the set-up call for caution.

(i) Simulating the tidal interaction of individual satellites with the host halo does not account for the interaction between satellites observed in group infall. Also, satellites contain themselves sub-substructures, which we also model as individual satellites.

(ii) For simplicity, our current host DM halo is approximated by an evolving spherical potential, thus neglecting the impact of triaxiality. However, Gill et al. (2004) find that the destruction rate of substructures is nearly independent of the triaxiality of the host halo.

(iii) The disc is modelled with an isotropic velocity dispersion in the corotating frame, which leads to lower rotation velocities compared to the MW disc. Consequently the difference in efficiency of dynamical friction on satellites with pro- and retrograde orbits is attenuated.

(iv) Regarding the internal DM distribution of the satellites, in this chapter we consider a fixed ratio of DM scale radius a_s and core size $r_c = 0.8\,a_s$, while different DM particle and feedback models motivate many other choices for relative or absolute core sizes (Pontzen & Governato, 2012; Vogelsberger et al., 2012; Rocha et al., 2013; Di Cintio et al., 2014; Elbert et al., 2015).

In contrast to self-consistent cosmological simulations with fixed N-body particle mass and gravitational softening length, our re-simulation technique follows the dynamical evolution of accreted substructures with the same numerical resolution for systems spanning many orders of magnitude in mass and size. For comparison, the Aq-A-2 run has a fixed particle mass of $m_p = 1.37 \times 10^4\,\mathrm{M}_\odot$, consequently haloes with $M_{200} = 10^8\,\mathrm{M}_\odot$ consist of $\sim 10^4$ particles at infall. Tidal stripping then reduces the particle number further. The simulations adopted in the studies of D'Onghia et al. (2010), Yurin & Springel (2015) and Zhu et al. (2016) use even larger DM particle masses of $m_p > 10^5\,\mathrm{M}_\odot$. For haloes with a mass of $10^8\,\mathrm{M}_\odot$ at z_{infall}, our satellites contain ~ 2 orders of magnitude more particles than the Aq-A-2 subhaloes. Furthermore, modelling the cosmological evolution of the host halo and disc potential analytically achieves high-enough resolution at a modest computational cost, which allows us to perform controlled simulations where we change single parameters at a time and quantify their effect on the surviving satellite population.

In the light of the apparent *indestructability* of cuspy subhaloes discussed in chapter 2, while tailored to follow the tidal evolution of subhaloes with equal relative resolution independent of their mass at infall, the simulations introduced in the current chapter are limited by the (finite) number of N-body particles resolving each subhalo, and by the (finite) resolution of the particle mesh code. The simulations therefore do not fully prevent the artificial disruption of cuspy subhaloes: Figure 3.2 reveals that at redshift $z = 0$, approximately 200 cuspy subhaloes have been stripped down to masses below the resolution limit of the simulation. A (re-)simulation making use of the cusp-reconstruction procedure of section 2.4 would allow to study the tidal evolution also of these currently unresolved subhaloes, avoiding artificial disruption caused by insufficient numerical resolution.

Appendix to Chapter 3

3.A Re-simulations of Aquarius A-2

Motivated by the need to resolve low-mass dark matter substructures in simulations of Milky Way-like haloes, two different suites of high-resolution re-simulations of the Aquarius A-2 merger tree were developed: the *Cusp Core Comparison Project* (CCCP). Implementation and parameters for the CCCP-I suite (used in chapter 3) are summarised in section 3.2. The CCCP-II suite (used in chapter 4) has a numerical set-up similar to CCCP-I with differences as detailed in Table 3.A.1.

The simulations were run on Archer*, the UK national supercomputer. Single subhaloes were run in serial on individual processor cores, grouped as 40 nodes of 24 cores each, with a clock rate of* 2.7 Ghz*. For each of the* CCCP-I *models (i.e. for each choice of subhalo profile and host potential),* $\sim 2{\times}10^3$ *core hours were used, compared to* $\sim 4{\times}10^4$ *core hours for each of the* CCCP-II *models.*

Principal differences. While in CCCP-I each subhalo is modelled with $N = 2 \times 10^6$ particles and a particle mesh code with 64^3 cubic cells per grid is adopted (see section 1.5.1), in CCCP-II these numbers are increased to $N = 10^7$ and 128^3. Both suites model subhaloes at accretion as generalised Hernquist profiles with scale radius a and core size r_c (Eq. 3.1 - see also Fig. 1.8, p. 25). The NFW structural parameters of the Aquarius subhaloes are translated to cuspy ($r_c = 0$) Hernquist profiles by matching the virial mass M_{200} and the radius r_{-2} where $\mathrm{d}\ln\rho/\mathrm{d}\ln r = -2$. For cored models, the same relation is used in CCCP-I, whereas in CCCP-II, the radius r_{-2} is matched also for cored haloes. Furthermore the disc mass was reduced in CCCP-II to resemble more closely the McMillan (2011) estimates for the Milky Way disc mass, and the disc scale radii $\{a_\mathrm{d}, b_\mathrm{d}\}$ evolve in CCCP-II with redshift.

Table 3.A.1: Principal differences between the CCCP-I and CCCP-II simulations. Both suites re-simulate the $\sim 10^3$ subhaloes with $M \geq 10^8\,\mathrm{M}_\odot$ of the Aquarius A-2 merger tree, modelling their density profiles at infall as generalised Hernquist profiles (Eq. 3.1) with scale radius a and core size r_c.

	CCCP-I	CCCP-II
N per subhalo	2×10^6	10^7
grid cells	64^3	128^3
core sizes r_c/a	0, 0.1, 0.2, …, 1	0, 1
NFW $\leftrightarrow$ Eq. 3.1	$2\,r_{-2} = a$	$2\,r_{-2} = a$ if $r_c/a = 0$ $r_{-2} = a$ if $r_c/a = 1$
host disc model	(i) no disc (ii) evolving disc: $M_\mathrm{d}(z) = 0.1 \times M_{200}(z)$ $\{a_\mathrm{d}, b_\mathrm{d}\}$ = const	evolving disc: $M_\mathrm{d}(z) = 0.025 \times M_{200}(z)$ $\{a_\mathrm{d}(z), b_\mathrm{d}(z)\} \propto r_{200}(z)$
snapshots	$z = 0, 1, 2, \ldots$: all particles	(i) every 10 Myrs: 2×10^4 particles per subhalo (ii) $z = 0$: all particles

Redshift $z = 0$. Figure 3.A.1 shows the $z = 0$ snapshot of the (cuspy, $r_c = 0$) CCCP-II simulation, colour coding the projected mass- and N-body particle densities. Low-mass substructures are more evident in the N-body density panel, particularly in the central regions of the halo, while in the mass density panel they are overwhelmed by the diffuse background density. A sample of ten cuspy subhaloes extracted at redshift $z = 0$ from the CCCP-II simulation is shown in Figure 3.A.2, ranging from tidally stripped subhaloes with prominent tidal streams and shells to virtually unperturbed subhaloes accreted at later times.

Evolution with redshift. Snapshots of the CCCP-I simulation corresponding to redshifts $z = 0$, 1, 2, 3, 4 are shown in Figure 3.A.3. A dashed circle indicates the virial radius r_{200} of the main halo. Subhaloes are injected in the simulation at the peak of their mass evolution, and are subsequently tidally stripped in the potential of the host halo. The tidally stripped material forms the seemingly diffuse background density in Figure 3.A.3, though tracing back the origin of the stripped material to single progenitors reveals its intricate structure of streams and shells (Figure 3.A.2).

Artificial disruption. Both CCCP-I and CCCP-II resolve subhaloes with a finite number of N-body particles. In contrast to simulations with fixed particle mass, the numerical setup is tailored to follow the tidal evolution of subhaloes with equal relative resolution independent of the subhalo mass at infall. In the light of the apparent *indestructability* of cuspy subhaloes discussed in chapter 2, the CCCP setup does not fully prevent the artificial disruption of substructures (see section 3.4).

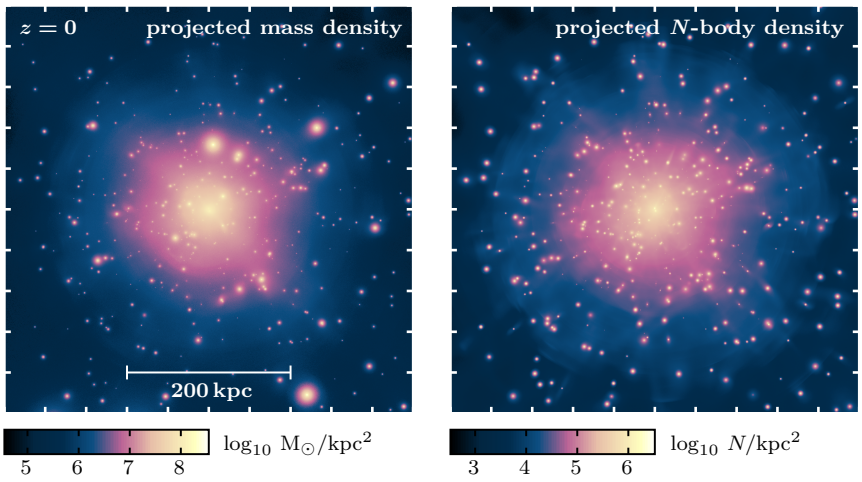

Figure 3.A.1: Projected mass density (left panel) and N-body particle density (right panel) at redshift $z = 0$ of the CCCP-II (re-)simulations. All subhaloes are modelled with 10^7 particles at infall independently of their mass, reaching N-body particle masses of $\sim 10\,\mathrm{M}_\odot$ for the least massive substructures. The above panels also visualise the resolution advantage of this re-simulation approach compared to N-body simulations with fixed particle mass: low-mass substructures emerge as overdense specks in the N-body particle density (right panel).

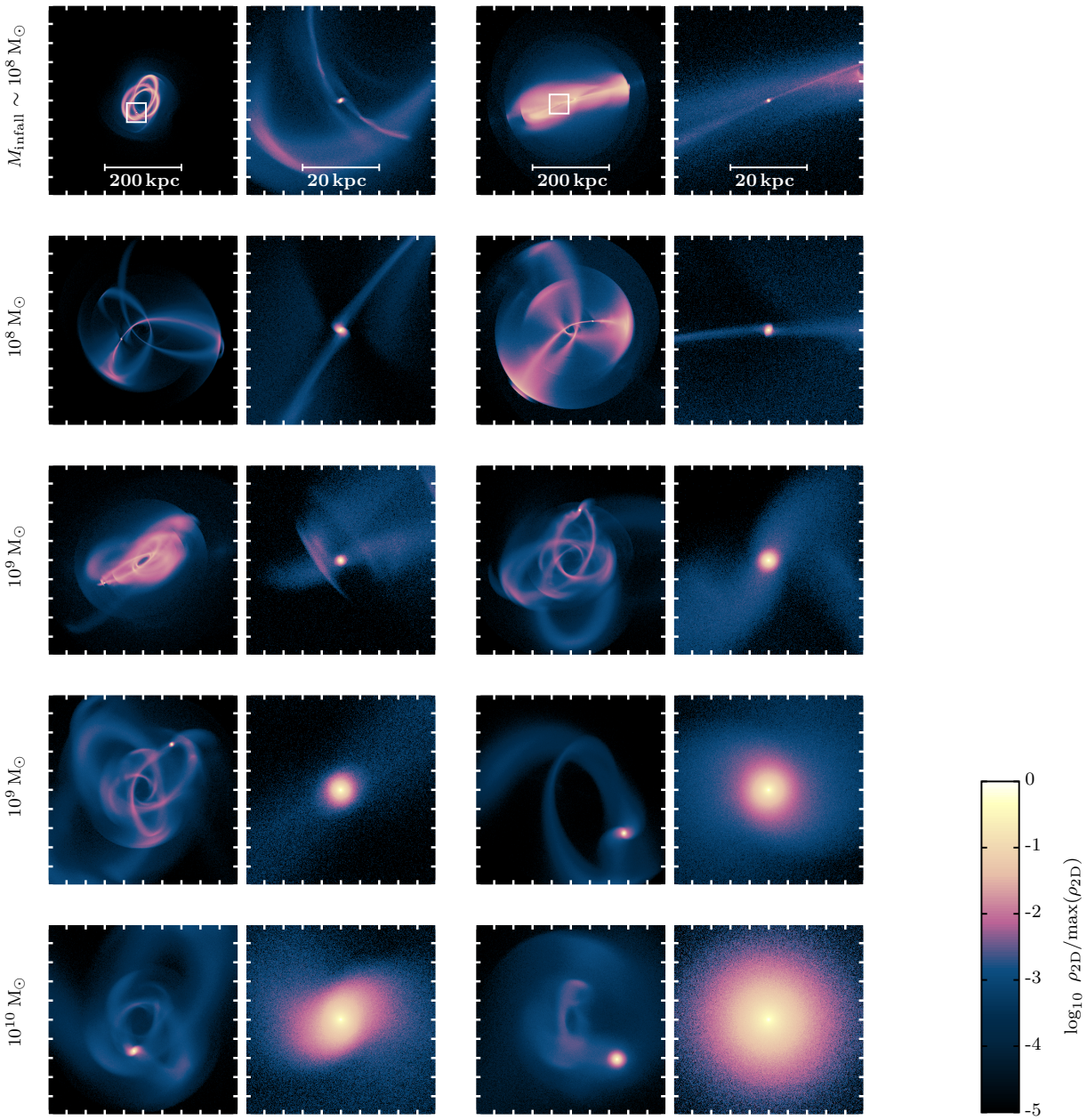

Figure 3.A.2: Selected single subhaloes at redshift $z = 0$ in the CCCP-II (re-)simulations. For each subhalo, an overview panel of $(500\,\mathrm{kpc})^2$ centred on the host halo as well as a detail view of $(50\,\mathrm{kpc})^2$ centred on the subhalo are shown. The projected density $\rho_{2\mathrm{D}}$ of the models is colour-coded, showing for each model five orders of magnitude in dynamic range.

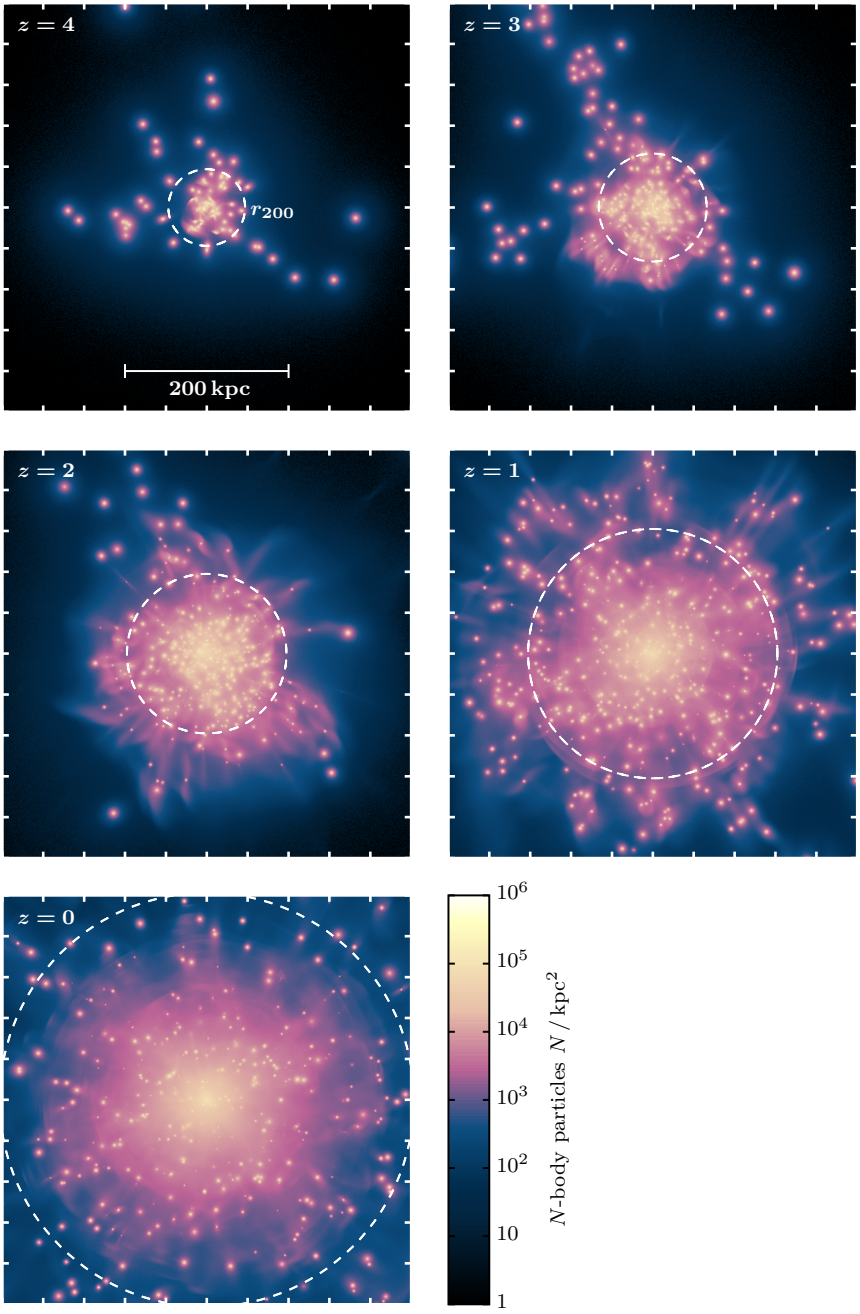

Figure 3.A.3: Redshift evolution of re-simulations of the Aquarius A2 merger tree (CCCP-I) for all subhaloes with $M \geq 10^8\,\mathrm{M}_\odot$ at accretion. The host model contains an axisymmetric disc (edge-on in the panels). Each subhalo is modelled as a cuspy Dehnen profile at accretion with $N = 10^6$ particles. The colour coding corresponds to the surface density of N-body particles, highlighting the smallest substructures. The dashed circle marks the virial radius $r_{200}(z)$ of the host halo.

Chapter 4

Dynamical mass estimates

Abstract

Mass estimators are a key tool to infer the dark matter content in pressure-supported systems like dwarf spheroidal galaxies (dSphs). We construct an estimator for enclosed masses based on the virial theorem which is insensitive to anisotropy in the velocity dispersion and tailored to yield masses with minimum uncertainty introduced by our ignorance on (i) the shape of the inner halo profile, and (ii) how deeply the stellar component is embedded within the halo: $M(< 1.8\,R_{\rm h}) \approx 3.5 \times 1.8\,R_{\rm h}\langle\sigma^2_{\rm los}\rangle G^{-1}$, where by $R_{\rm h}$ we denote the projected half-light radius and by $\langle\sigma^2_{\rm los}\rangle$ the luminosity-averaged squared line-of-sight velocity dispersion. Tests against controlled simulations show that this estimator provides unbiased enclosed masses with an accuracy of ~ 10 per cent. This confirms the robustness of similar previously proposed mass estimators. Application to published kinematic data of Milky Way dSphs reveals a tight correlation between enclosed mass and luminosity. Using N-body models we show that tidal stripping has little effect on this relation. Comparison against cuspy and cored dark matter haloes extracted from controlled re-simulations of the Aquarius A2 merger tree shows that the high mass densities of ultrafaint galaxies are not compatible with large dark matter cores, and that the (total) halo masses of the classical Milky Way dSphs span a remarkably narrow range ($8 \lesssim \log_{10}(M/{\rm M}_\odot) \lesssim 10$) at present, showing no clear trend with either galaxy size or luminosity.

This chapter has been published in MNRAS 481, 5073–5090 (2018) (RE, J. Peñarrubia, M. Walker: Systematics in virial mass estimators for pressure supported systems, arXiv:1805.00484).

4.1 Introduction

Understanding the distribution of dark matter (DM) on galactic scales is at the root of constraining DM particle properties and processes of galaxy formation like baryonic feedback, as discussed in chapter 1.2.1. Dwarf spheroidal galaxies (dSphs), lying at the faintest end of the galaxy luminosity function and reaching mass-to-light ratios of up to $\sim 10^3$ (see e.g. Walker et al., 2007; McConnachie, 2012) are promising candidates to study the DM distribution on kpc scales. But obtaining such constraints through kinematic data is a challenging task: the galaxies are observed in projection, and precise velocity measurements are feasible only along the line of sight - though recently

attempts have been made to constrain the 3D motion of stars in the Sculptor dwarf galaxy (Massari et al., 2018).

Having access only to velocities along the line of sight, the enclosed mass $M(< r_0)$ within a specific spherical radius r_0 may be obtained from the projected virial theorem for spherical systems (see e.g. Merrifield & Kent, 1990; Agnello & Evans, 2012, and section 1.4.3 in this thesis), relating the projected components of the pressure and potential energy tensors. For the case of self-gravitating systems and those where mass traces light with De Vaucouleurs luminosity profile, Illingworth (1976) describes how to infer the total mass ($r_0 \to \infty$) from the luminosity-averaged squared line-of-sight velocity dispersion $\langle \sigma^2_{\rm los} \rangle$. Merritt (1987) shows how lower limits on the enclosed mass $M(< r_0)$ can be obtained from the virial theorem for systems where mass and luminosity profile have different functional forms. Mass estimates from the virial theorem can be obtained also for dSphs consisting of a stellar tracer embedded in a DM halo (see section 4.2). Such estimates are based entirely on projected and averaged dispersion measurements, though including velocity components tangential to the line of sight is straightforward (see section 4.6). The method requires however to make assumptions on the DM halo shape and on how deeply the stellar component is embedded within the halo.

Alternatively, masses enclosed within a spherical radius r_0 can be obtained from the radial velocity dispersion $\sigma_{\rm r}(r)$ at a radius $r = r_0$ by means of the Jeans equations (see e.g. chapter 4.2 in BT87, and section 1.4.2 in this thesis). Both the radial velocity dispersion $\sigma_{\rm r}(r)$ at a spherical radius r and the observed line-of-sight velocity dispersion $\sigma_{\rm los}(R)$ measured at a projected radius R depend on the DM halo shape as well as the function $\beta(r) \equiv 1 - \sigma^2_\perp(r)/\sigma^2_r(r)$ which parametrizes the anisotropy of the velocity dispersion as a function of radius r, $\sigma^2_\perp(r)$ being the tangential component of the velocity dispersion (see e.g. Binney & Mamon, 1982). Current galaxy formation models do not yield clear predictions for the behaviour of $\beta(r)$. In principle, $\beta(r)$ does not need to be a monotonic function of r, and it might vary between different stellar populations within the same dwarf. Our ignorance of $\beta(r)$ gives rise to the infamous mass - anisotropy degeneracy.

Various mass estimators have been proposed which rely on the assumption that the enclosed mass is directly proportional to local or global averages of the observed line-of-sight velocity dispersion. Mass estimators of this type have been tested on cosmological simulations (Campbell et al., 2017; González-Samaniego et al., 2017) and proven to give accurate masses within a factor of unity. E.g. for the case of isotropic (i.e. $\beta(r) = 0$) King models embedded in Navarro et al. (1997) haloes, Peñarrubia et al. (2008a) show that measuring the mass $M(< r_0)$ enclosed within the projected King core radius $r_0 = R_{\rm c}$ minimizes the uncertainty introduced by how deeply the stellar component is segregated within the DM halo. Their estimator reads $M(< R_{\rm c}) \approx 1.44\, R_{\rm c}\, \sigma^2_{\rm los}(0) G^{-1}$, where $\sigma^2_{\rm los}(0)$ denotes the central line-of-sight velocity dispersion. Walker et al. (2009c) model the stellar tracer profiles as Plummer

spheres and assume flat velocity dispersion profiles to estimate the enclosed mass as $M(< R_\mathrm{h}) \approx 2.5\, R_\mathrm{h}\ \langle\sigma^2_\mathrm{los}\rangle G^{-1}$, showing numerically that the uncertainty introduced by a constant $\beta(r)$ is relatively small when measuring the enclosed mass at the projected half-light radius R_h. Wolf et al. (2010) reach a similar conclusion by analytical means, showing that the deprojected half-light radius approximately coincides with the radius where the anisotropy parameter $\beta(r)$ (modelled using a three-parameter function) has the smallest effect on the inferred enclosed mass. Their estimator reads $M(< r_\mathrm{h}) \approx 3.0\, r_\mathrm{h}\ \langle\sigma^2_\mathrm{los}\rangle G^{-1}$, where $r_\mathrm{h} \approx 4/3\ R_\mathrm{h}$ is the deprojected half-light radius. For the family of Michie-King distribution functions, Amorisco & Evans (2012) find that $M(< 1.7\, R_\mathrm{h}) \approx 5.8\, R_\mathrm{h}\ \sigma^2_\mathrm{los}(R_\mathrm{h}) G^{-1}$, where $\sigma^2_\mathrm{los}(R_\mathrm{h})$ is measured at the projected half-light radius R_h. By purely numerical means, Campbell et al. (2017) find $M(< 1.8\, R_\mathrm{h}) \approx 6.0\, R_\mathrm{h}\ \langle\sigma^2_\mathrm{los}(< 1.04\, R_\mathrm{h})\rangle G^{-1}$ from a dispersion-supported sample of galaxies of the APOSTLE simulation project (Sawala et al., 2016), averaging σ^2_los within $1.04\, R_\mathrm{h}$, denoting by R_h the projected half-light radius.

The mass - anisotropy degeneracy may be broken if kinematic measurements of several chemo-dynamically distinguishable stellar populations within the same dSph can be obtained as discussed e.g. by Saglia et al. (2000), Battaglia et al. (2008) and Amorisco & Evans (2012), whereas Diakogiannis et al. (2014) suggest to measure $\sigma_\mathrm{los}(R)$ at different projected radii R and to model $\beta(r)$ using splines. With access to proper motions tangentially to the line of sight for a subsample of tracer stars, stronger constraints on $\beta(r)$ can be obtained (see e.g. Strigari et al., 2007; Watkins et al., 2013). Łokas & Mamon (2003) show that a joint analysis of the velocity dispersion profile and higher order moments like the kurtosis may be used to break the mass - anisotropy degeneracy under specific assumptions for the form of $\beta(r)$. Breddels et al. (2013) model dSphs by Schwarzschildt orbit superposition to fit both the observed light distribution as well as the second- and forth-order velocity moments, and apply the method to a catalogue of 2000 stars of the Sculptor dSph. They show that with 2000 tracers, the central slope $\gamma = -\mathrm{d}\ln\varrho(r)/\mathrm{d}\ln r\ (r \to 0)$ of the DM density profile $\varrho(r)$ cannot be constrained to tell cuspy from cored profiles, and $\beta(r)$ cannot be constrained for radii smaller than 0.1 kpc - these authors conclude that to obtain unbiased estimates of the central slope γ, a larger number of tracer stars is necessary. Richardson & Fairbairn (2014) use virial shape parameters derived from the fourth-order virial equations to constrain DM density profiles compatible with the observed kinematics of embedded stellar tracers. Applied to the Sculptor dSph, the authors find that a cuspy DM halo is favoured if the stellar distribution is modelled as a Plummer profile. If the outer slope of the stellar profile however is allowed to vary, the available kinematic data do not allow to constrain the central DM profile slope. Using N-body mock data, Read & Steger (2017) show that with 10^4 tracer stars, no reliable $\beta(r)$ profile can be recovered from projected velocities and Jeans analysis alone. However, making use also of virial shape parameters or velocity measurements tangentially to the line of sight, using 10^3 tracer stars, both $\beta(r)$ and the underlying

mass profile can be constrained within a few multiples of the half-light radius. A different approach is discussed by Wang et al. (2015), who fit analytical distribution functions to observables extracted from stellar tracers embedded in DM haloes of the Aquarius (Springel et al., 2008) simulations. These authors find that the derived halo masses are biased (by up to 40 per cent) even when using not only line of sight but also tangential velocity measurements.

Mass estimators played a crucial role in identifying possible tensions between N-body simulations of Milky Way-like DM haloes and the observed population of satellite galaxies of the Milky Way: Boylan-Kolchin et al. (2011) made use of the Wolf et al. (2010) estimator to identify N-body subhaloes compatible with the mean densities of Milky Way dwarfs, finding that none of the bright Milky Way dwarfs are dense enough to be embedded in haloes similar to the most massive simulated N-body subhaloes of the Aquarius simulations (the *too big to fail problem*). Based on estimates of enclosed masses of two distinct stellar populations embedded in the same DM halo, Walker & Peñarrubia (2011) introduced a method to infer the slope $\Gamma \approx \Delta \ln M(< r)/\Delta \ln r\,(r \to \bar{R}_{\rm h})$ of the underlying DM halo at the average half-light radius $\bar{R}_{\rm h}$, finding that both the Fornax and the Sculptor dSph must be embedded in DM haloes with constant-density cores, in conflict with the centrally divergent density cusps of haloes in DM-only simulations (the *cusp/core problem*). Laporte et al. (2013) subsequently showed that also for triaxial DM haloes, the Walker & Peñarrubia (2011) method gives reliable lower limits on the slope Γ. Sawala et al. (2015) use halo masses derived by Peñarrubia et al. (2008a) for Milky Way dSphs using the Walker et al. (2009c) estimator to motivate their corrections to stellar mass - halo mass relations obtained from abundance matching based on DM-only simulations. More recently, Fattahi et al. (2018) make use of the Wolf et al. (2010) estimator to study the tidal evolution DM haloes of the APOSTLE simulations compatible with the observed kinematics of Milky Way dSphs.

In this chapter, we study a virial mass estimator which is minimally affected by our ignorance on two key parameters: (i) the shape of the inner DM halo profile, and (ii) the spatial segregation of the stellar tracers within the DM halo. The use of the projected spherical virial theorem has several advantages over Jeans analysis for the construction of mass estimators: The virial theorem does not contain any functional dependence on $\beta(r)$ and thereby avoids the mass-anisotropy degeneracy. Also systematic biases of inferred enclosed masses and slopes Γ follow directly from the assumptions made on the DM and stellar density profiles and are independent of sample size. Furthermore, the average squared velocity dispersion $\langle \sigma^2_{\rm los} \rangle$ is a sum over all stars and does not require any binning of data. This makes mass estimators based on the virial theorem applicable also to systems with only few stellar tracers - carefully factoring in the uncertainties due to sample size on the measured squared velocity dispersion as pointed out by Laporte et al. (2019).

This chapter is structured as follows: in section 4.2 we introduce the spherical virial theorem and discuss the systematics of mass estimators for dwarf galaxies consisting of a stellar tracer population embedded inside a DM halo. In section 4.3 we construct a mass estimator which is tailored to minimize the uncertainty introduced by our ignorance on the central slope of the underlying DM profile as well as on how deeply embedded the stellar component is within the DM halo. We do test this mass estimator on a catalogue of N-body mocks. Section 4.4 discusses how to obtain the total halo masses of dwarf galaxies, breaking the degeneracy between structural parameters constrained by use of the virial theorem with the help of controlled cosmological simulations. In section 4.5, we estimate the masses of Milky Way dwarf galaxies using the methods introduced in the previous sections, and discuss implications of the derived stellar mass - halo mass relation for satellite galaxies. Section 4.6 summarizes methods and main results.

4.2 Mass estimates from the virial theorem

With the aim of estimating masses of dwarf galaxies from their observed velocity dispersions while avoiding the infamous mass - anisotropy degeneracy, in the spirit of Agnello & Evans (2012), we construct a mass estimator based on the projected virial theorem for spherical systems,

$$2K_{\rm los} + W_{\rm los} = 0 \ . \tag{4.1}$$

We distinguish between the mass profile $M(<r)$ which sources the potential, and a mass-less tracer component of density $\nu_\star(r)$ embedded in this potential. The pressure term is given by the projected velocity dispersion of the tracer and can be measured directly:

$$2K_{\rm los} = 2\pi \int_0^\infty \Sigma_\star(R)\, \sigma^2_{\rm los}(R)\, R\, {\rm d}R \equiv \langle \sigma^2_{\rm los} \rangle \ , \tag{4.2}$$

where by $\Sigma_\star(R)$ and $\sigma^2_{\rm los}(R)$ we denote the surface density and line-of-sight velocity dispersion of the tracer at a projected (2D) radius R, respectively. The surface density is normalized so that $2\pi \int_0^\infty R\Sigma_\star(R){\rm d}R = 1$. The potential energy term

$$W_{\rm los} = -\frac{4\pi G}{3} \int_0^\infty r\nu_\star(r) M(<r) {\rm d}r \tag{4.3}$$

can be calculated for a given normalized tracer density profile $\nu_\star(r)$ and mass distribution $M(<r)$, where r is the spherical (3D) radius and the tracer density is normalized so that $4\pi \int_0^\infty r^2\nu_\star(r){\rm d}r = 1$. We will keep this notation for spherical (r) and projected (R) radii throughout this chapter. Equations 4.1 - 4.3 allow $\langle \sigma^2_{\rm los} \rangle = -W_{\rm los}$ to be calculated from the tracer and mass profiles alone. In contrast to the Jeans equations,

these virial equations and in specific the integral $\langle\sigma^2_{\rm los}\rangle$ are independent of anisotropies in the tracer velocity dispersion and thereby avoid the mass - anisotropy degeneracy.

The mass within a radius r_0 can be computed from the observed $\langle\sigma^2_{\rm los}\rangle$ as $M(<r_0) = \mu\ r_0\ \langle\sigma^2_{\rm los}\rangle/G$ where

$$\mu(r_0) = -\frac{G\ M(<r_0)}{r_0\ W_{\rm los}} \tag{4.4}$$

is a dimensionless function of the radius r_0 and the parameters describing the tracer density and mass distribution.

4.2.1 Self-gravitating systems

As a first example, consider the case of a spherical system where the tracer density equals the mass density. For Dehnen (1993) profiles of total mass $M_{\rm tot}$, scale radius a, scale density $\varrho_s = (3-\gamma)M_{\rm tot}/4\pi a^3$, outer slope $\beta \equiv -{\rm d}\ln\varrho/{\rm d}\ln r\ (r\to\infty) = 4$, inner slope $\gamma \equiv -{\rm d}\ln\varrho/{\rm d}\ln r\ (r\to 0)$ within the range $0 \le \gamma \le 1$, written in terms of the general $\{\alpha,\beta,\gamma\}$ profile with $\alpha = 1$,

$$\varrho(r) = \varrho_s \left(\frac{r}{a}\right)^{-\gamma} \left[1+\left(\frac{r}{a}\right)^{\alpha}\right]^{(\gamma-\beta)/\alpha}\ , \tag{4.5}$$

the potential energy term becomes

$$W_{\rm los} = -\frac{GM_{\rm tot}}{a}\frac{1}{6(5-2\gamma)} \tag{4.6}$$

and

$$\mu_\gamma(r_0/a) = \left(1+\frac{a}{r_0}\right)^{\gamma-3}\left(\frac{a}{r_0}\right) 6(5-2\gamma) \tag{4.7}$$

is a function of the radius r_0 and the scale radius a in the combination r_0/a alone. For a fixed r_0, μ_γ reduces to a number, e.g. for the deprojected half-light radius $r_{\rm h} = a/(2^{1/(3-\gamma)}-1)$, $\mu_1(r_{\rm h}) = 9(\sqrt{2}-1) \approx 3.7$, and $\mu_0(r_{\rm h}) = 15(2^{1/3}-1) \approx 3.9$.

Illingworth (1976) introduced an estimator based on the same approach for the total mass of self-gravitating elliptical galaxies which follow a De Vaucouleurs surface brightness profile, i.e. $\log\Sigma_\star(R)/\Sigma_\star(0) \propto R^{1/4}$. The estimator reads $M_{\rm tot} \approx 8.6\,R_{\rm h}\langle\sigma^2_{\rm los}\rangle/G$, denoting by $R_{\rm h}$ the projected half-light radius. In comparison, for our example of Dehnen (1993) density profiles, the projected half-light radius $R_{\rm h}$ equals $\approx 2.9a$ $(1.8a)$ for $\gamma = 0$ $(\gamma = 1)$, and we find $M_{\rm tot} \approx 10.3\,R_{\rm h}\langle\sigma^2_{\rm los}\rangle/G$ for $\gamma = 0$ and $M_{\rm tot} \approx 9.9\,R_{\rm h}\langle\sigma^2_{\rm los}\rangle/G$ for $\gamma = 1$. Using Schwarzschildt orbit modelling under the assumption that mass follows light, Cappellari et al. (2006) fit kinematics of 25 elliptical (E) and lenticular (S0) galaxies to obtain the total mass estimate $M_{\rm tot} \approx 5\,R_{\rm h}\langle\sigma^2_{\rm los}(<R_{\rm h})\rangle/G$, where $\langle\sigma^2_{\rm los}(<R_{\rm h})\rangle$ is averaged within the projected half-light radius $R_{\rm h}$. Note that this estimator is not independent of the anisotropy profile

$\beta(r)$ as only the virial average $\langle\sigma^2_{\rm los}\rangle$ over the entire system removes the dependence on $\beta(r)$. Agnello et al. (2014) argue that this global average can be challenging to compute for faint systems, and explore for systems with De Vaucouleurs luminosity profile and Ospikov-Meritt anisotropy profile $\beta(r) = r^2/(r^2 + r_a^2)$ how the coefficient $GM(< R)/R\langle\sigma^2_{\rm los}(< R)\rangle$ changes as a function of the radius R over which the velocity dispersion is averaged. For systems where mass traces light, they propose a mass estimator similar to Illingworth (1976).

4.2.2 Stellar tracer embedded in DM potential

For the case of dwarf galaxies with a stellar population embedded inside a DM halo, the mass profile which sources the potential is not accessible to direct observation. Let us assume that the projected half-light radius $R_{\rm h}$ and the luminosity-averaged squared velocity dispersion $\langle\sigma^2_{\rm los}\rangle$ are known quantities. This motivates a virial mass estimator for the enclosed mass $M(< r_0)$ with $r_0 = \lambda R_{\rm h}$ of the form (Amorisco & Evans, 2012):

$$M_{\rm est}(< \lambda R_{\rm h}) = \frac{\mu\ \lambda R_{\rm h}\ \langle\sigma^2_{\rm los}\rangle}{G}\ , \tag{4.8}$$

where λ and μ are dimensionless factors.

Using equation 4.8, we now aim to determine the mass enclosed within the spherical radius $r_0 = \lambda R_{\rm h}$. We treat stars as mass-less tracers of the underlying DM potential, consequently $M(< r)$ is determined by the DM profile alone. In the following, we assume that the stellar tracer distribution follows a spherical Plummer profile, $\{\alpha_\star, \beta_\star, \gamma_\star\} = \{2, 5, 0\}$. To develop some intuition for the range of values which μ can take, consider a (scale-free) power-law DM profile with $\varrho \propto r^{-\gamma}$, i.e. the asymptotic case $R_{\rm h}/r_{\rm max} \to 0$ of a stellar population deeply embedded inside the DM host halo. Then μ is a function of λ and γ alone,

$$\mu_\gamma(\lambda) \overset{R_{\rm h}\to 0}{=} \frac{2\lambda^{2-\gamma}}{\mathrm{B}\left(\gamma/2,\ (5-\gamma)/2\right)} \tag{4.9}$$

where by B we denote the Euler beta function. For $\gamma = 1$ this reduces to $\mu_1 = 3\lambda/2$, whereas for $\gamma \to 0$, $\mu_\gamma \to 0$ as $\langle\sigma^2_{\rm los}\rangle = -W_{\rm los}$ diverges. For scale-free cuspy DM haloes with $1 < \gamma < 3$, similar results are shown in Agnello et al. (2014, figures 2 & 3) computed from the Jeans equations for stellar tracers with De Vaucouleurs luminosity profile and Ospikov-Merritt anisotropy profile.

For non scale-free DM haloes, e.g. the density profile of equation 4.5 with scale radius a and two different asymptotic behaviours for $r \gg a$ and $r \ll a$, μ is not only a function of λ but also of the segregation parameter $R_{\rm h}/r_{\rm max}$ describing how deeply embedded the stars are within the DM halo. There, by $r_{\rm max}$ we denote the radius of maximum circular velocity $v_{\rm max} = \left(GM\left(< r_{\rm max}\right)/r_{\rm max}\right)^{1/2}$. Motivated by the result of controlled simulations that DM haloes undergoing tidal stripping have steeper outer slopes $\beta \equiv -\mathrm{d}\ln\varrho/\mathrm{d}\ln r\ (r \to \infty)$ than field haloes, i.e. $\beta \approx 5$ (see Peñarrubia et al.,

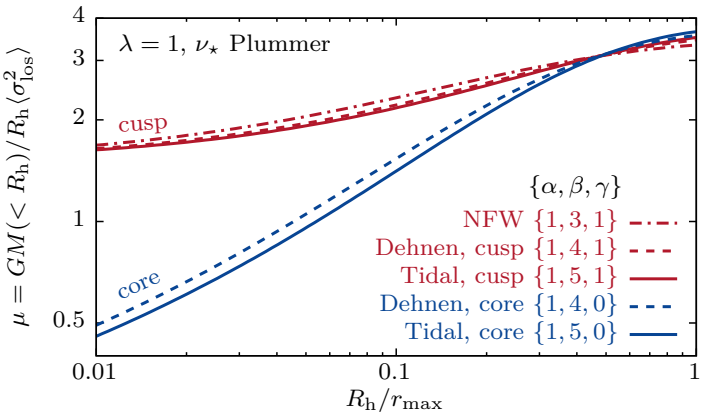

Figure 4.1: Dimensionless factor μ for $\lambda = 1$ (see equation 4.8) as a function of segregation $R_\mathrm{h}/r_\mathrm{max}$ for stellar Plummer profiles with projected half-light radius R_h embedded in cored ($\gamma = 0$) and cuspy ($\gamma = 1$) DM haloes for tidally stripped systems, $\{\alpha, \beta, \gamma\} = \{1, 5, \gamma\}$ (see equation 4.5). For comparison, the functional dependence of μ on segregation is also shown for cuspy and cored Dehnen ($\beta = 4$) and NFW ($\beta = 3$) profiles.

2009, 2010, and Figure 2.4, p. 37, in this thesis) in contrast to the outer slope of $\beta = 3$ of NFW profiles (Navarro et al., 1997), Fig. 4.1 shows μ for the choice of $\lambda = 1$ as a function of the segregation parameter $R_\mathrm{h}/r_\mathrm{max}$ for stellar Plummer spheres embedded in cored ($\gamma = 0$) and cuspy ($\gamma = 1$) DM haloes with density profile as in equation 4.5, using $\beta = 5$ and $\varrho_s = M_\mathrm{tot}(3-\gamma)(4-\gamma)/4\pi a^3$. We choose $\alpha = 1$ motivated by the value found for equilibrium haloes in cosmological N-body simulations (Navarro et al., 1997). For comparison, the functional behaviour of μ is also shown for Dehnen, i.e. $\{\alpha, \beta, \gamma\} = \{1, 4, \gamma\}$, and NFW $\{1, 3, 1\}$ profiles. In the limit $R_\mathrm{h}/r_\mathrm{max} \to 0$, we recover the asymptotic behaviour of equation 4.9 for $\lambda = 1$: $\mu \to 3/2$ for haloes with $\gamma = 1$, and $\mu \to 0$ for cored ones. For the segregations shown, μ is less sensitive to the steepness of the outer slope ($\beta = 3, 4, 5$) of the DM halo than it is to the inner one ($\gamma = 0, 1$).

Our ignorance of $R_\mathrm{h}/r_\mathrm{max}$ limits us to the use of a constant value of μ when estimating masses using equation 4.8. This leads to a systematic uncertainty on the estimated masses, and this uncertainty is more pronounced for cored haloes where $\mu_{\gamma=0} \to 0$ for the case of deeply embedded stellar populations. In section 4.3 we will discuss choices of μ, λ which minimize this uncertainty.

4.2.3 Slope estimates from two stellar populations

For dSph galaxies containing two chemo-dynamically distinguishable stellar populations with projected half-light radii $R_\mathrm{h,inner}$ and $R_\mathrm{h,outer}$ (where $R_\mathrm{h,inner} < R_\mathrm{h,outer}$), the combined velocity dispersion measurements from both populations can be used to further constrain structural properties of the underlying DM halo. Agnello & Evans (2012) use the virial theorem to obtain a lower limit on the core size of the DM halo

of the Sculptor dSph, modelling the stellar populations as Plummer spheres and the DM halo as a cored NFW profile (Agnello & Evans, 2012, equation 18).

Based on a mass estimator with the functional form of equation 4.8, assuming $\mu = \text{const}$, Walker & Peñarrubia (2011) introduce an estimator for the central slope $\Gamma = \mathrm{d}\ln M(<r)/\mathrm{d}\ln r$ of the underlying DM halo which does not rely on assumptions about the DM profile shape. Approximating Γ as a finite difference, and allowing μ to vary with radius r, we obtain from equation 4.8

$$\Gamma \;=\; \frac{\mathrm{d}\ln M(<r)}{\mathrm{d}\ln r} \;\approx\; \underbrace{\frac{\Delta\ln\mu}{\Delta\ln R_\mathrm{h}}}_{\varepsilon} \;+\; \underbrace{1 \;+\; \frac{2\ln\left(\sigma_\mathrm{outer}/\sigma_\mathrm{inner}\right)}{\ln\left(R_\mathrm{h,outer}/R_\mathrm{h,inner}\right)}}_{\mathrm{WP11}}\,, \tag{4.10}$$

where WP11 refers to the estimator introduced by Walker & Peñarrubia (2011), and writing for brevity $\sigma \equiv \langle\sigma^2_\mathrm{los}\rangle^{1/2}$. The virial theorem allows us to study the systematics of this estimator for different DM and stellar density profiles. For this aim, we embed two stellar tracer populations with density $\nu_\star(r)$ and projected half-light radii $R_\mathrm{h,inner}$ and $R_\mathrm{h,outer} = 2\,R_\mathrm{h,inner}$ in cuspy ($\gamma = 1$) or cored ($\gamma = 0$) tidally stripped DM haloes (equation 4.5 with $\alpha = 1, \beta = 5$). The top panel of Fig. 4.2 shows the resulting $\varepsilon = \Delta\ln\mu/\Delta\ln R_\mathrm{h}$ as a function of segregation.

(i) If $\nu_\mathrm{\star,inner}$ and $\nu_\mathrm{\star,outer}$ are Plummer profiles, $\{\alpha_\star, \beta_\star, \gamma_\star\} = \{2, 5, 0\}$, (solid lines), then $\varepsilon > 0$ for the range of segregations $R_\mathrm{h}/r_\mathrm{max}$ shown, i.e. in this case WP11 underestimates the slope Γ of the underlying DM profile with $\varepsilon \lesssim 0.2, 0.6$ for the cuspy and cored DM halo, respectively.

(ii) WP11 also underestimates Γ if the inner population has a shallow central density cusp, $\{\alpha_\star, \beta_\star, \gamma_\star\} = \{2, 5, 0.5\}$, and the outer population follows a Plummer density profile (dotted lines).

(iii) If instead the outer population has a shallow central density cusp and the inner population is a Plummer profile, then $\varepsilon < 0$ for cuspy haloes and segregations $R_\mathrm{h}/r_\mathrm{max} \lesssim 0.1$, i.e. in this configuration, WP11 overestimates Γ (dashed lines).

In the bottom panel of Fig. 4.2, the outer slope of one of the stellar tracers is chosen to be steeper, $\{\alpha_\star, \beta_\star, \gamma_\star\} = \{2, 6, 0\}$, than in the Plummer case:

(iv) If the outer population has a steeper outer slope $\beta_\star$ whereas the inner population is a Plummer profile, then $\varepsilon < 0$ for deeply embedded tracers (dashed lines).

(v) On the other hand, if the inner population has a steeper outer slope and the outer population is a Plummer profile, ε takes values of up to order of unity for deeply embedded tracers in cored DM haloes (dotted lines).

These results show that the shapes of the stellar tracer profiles need to be taken into account when estimating Γ, as omitting to do so may lead to underestimation of Γ by values of up to order of unity.

Furthermore, note that the mass estimator of Eq. 4.12 assumes spherically symmetric dark matter and stellar distributions. Genina et al. (2018) show that for simulated dwarf galaxies with aspherical stellar distributions, inferred slopes of the underlying dark matter distribution can be systematically biased, falsely suggesting cored dark matter distributions even in the presence of density cusps.

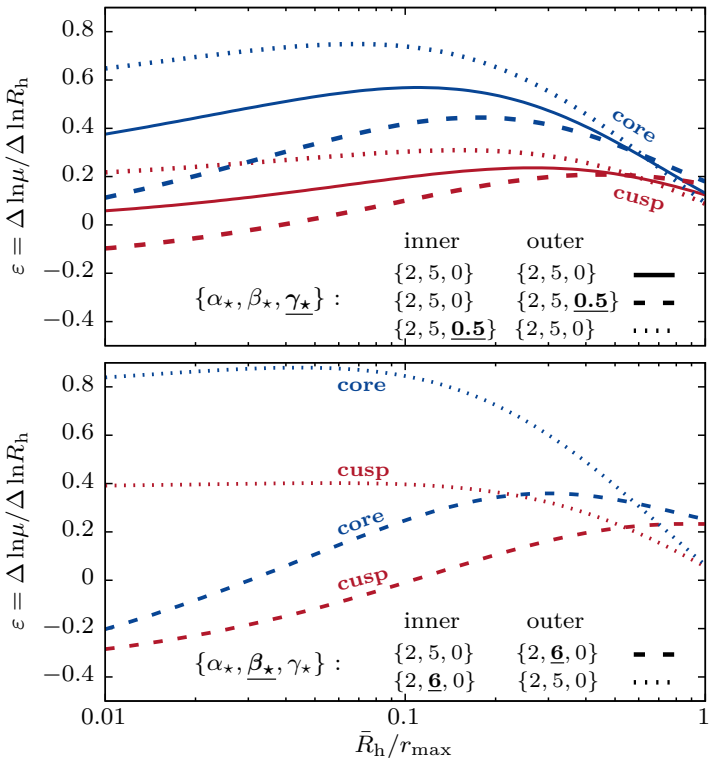

Figure 4.2: Logarithmic slope $\varepsilon = \Delta \ln \mu / \Delta \ln R_{\rm h}$ computed for two stellar tracer populations with half-light radii $R_{\rm h,inner}$ and $R_{\rm h,outer} = 2R_{\rm h,inner}$, embedded in cuspy ($\gamma = 1$) or cored ($\gamma = 0$) DM haloes with $\{\alpha, \beta, \gamma\} = \{1, 5, \gamma\}$ density profile (equation 4.5). The slope is shown as a function of the mean half-light radius $\bar{R}_{\rm h} = (R_{\rm h,inner} + R_{\rm h,outer})/2$. *Top panel*: solid lines show ε for systems where both the inner and the outer stellar tracer populations have Plummer $\{\alpha_\star, \beta_\star, \gamma_\star\} = \{2, 5, 0\}$ density profiles. The dashed curves correspond to systems where one of the tracer populations has a shallow central density cusp of slope $\gamma_\star$. *Bottom panel:* the outer slope $\beta_\star$ of one of the tracers is chosen to be steeper than the Plummer case.

4.3 Unbiased minimum variance mass estimates

In the previous section, we have shown how our ignorance on the segregation parameter $R_\mathrm{h}/r_\mathrm{max}$ leads to an uncertainty on the estimated masses which depends on the shape of the underlying DM profile. We now aim to determine values $\bar{\lambda}, \bar{\mu}$ so that the mass estimator of equation 4.8 is unbiased regarding (i) the DM profile shape (ii) how deeply embedded the stellar population is within the DM halo. By unbiased we intend not to make prior assumptions about the specific value of the segregation parameter $R_\mathrm{h}/r_\mathrm{max}$ and the inner[4] slope γ of the DM potential. By minimum variance we intend to choose $\bar{\lambda}, \bar{\mu}$ so that the relative error on the estimated masses due to our ignorance on $R_\mathrm{h}/r_\mathrm{max}$ and γ is minimized.

[4] *As shown in Fig. 4.1, comparing the cuspy Dehnen profile with outer slope β=4 to the NFW profile ($\beta = 3$), for deeply embedded stellar systems, the outer slope of the DM halo does not affect the value of μ by much*

4.3.1 Minimizing the variance as a function of λ

Under the assumption of stellar Plummer spheres which are deeply embedded inside tidally stripped DM haloes ($\alpha = 1, \beta = 5$ in equation 4.5), for a given value of λ, we marginalize μ (equation 4.8) over segregations in the range $0 \leq R_\mathrm{h}/r_\mathrm{max} \leq 1$ and central DM slopes in the range $0 \leq \gamma \leq 1$. We assume flat distributions when marginalizing over R_h and r_max:

$$\langle \mu(\lambda) \rangle = \int_0^1 \mathrm{d}(R_\mathrm{h}/r_\mathrm{max}) \int_0^1 \mathrm{d}\gamma \; \mu_\gamma(\lambda, R_\mathrm{h}/r_\mathrm{max}) \quad . \tag{4.11}$$

The steepest central slope considered corresponds to the central slope of the NFW profile, and the range of slopes is consistent with the slopes measured in the hydrodynamical simulations of the MaGICC project (Di Cintio et al., 2014). The upper limit of the integration range in $R_\mathrm{h}/r_\mathrm{max}$ is motivated by the findings reported in section 4.5.3 from a sample of Milky Way dwarf galaxies. Fig. 4.3 shows how $\langle \mu(\lambda) \rangle \pm s$ with $s^2 = \langle \mu(\lambda)^2 \rangle - \langle \mu(\lambda) \rangle^2$ evolves as a function of λ, as well as $\langle \mu_\gamma(\lambda) \rangle$ where we marginalize over $R_\mathrm{h}/r_\mathrm{max}$ alone, separately for cuspy ($\gamma = 1$) and cored ($\gamma = 0$) DM profiles.

At λ_eq, there is no functional dependence on γ as $\langle \mu_{\gamma=0} \rangle = \langle \mu_{\gamma=1} \rangle \equiv \mu_\mathrm{eq}$. For each DM profile, $\bar{\lambda}_\gamma$ minimizes the squared relative error $s^2_\gamma / \mu^2_\gamma$ when marginalizing over $R_\mathrm{h}/r_\mathrm{max}$ alone. The values $\bar{\lambda} = 1.8$, $\bar{\mu} = 3.5$ minimize the squared relative error after marginalizing over both γ and $R_\mathrm{h}/r_\mathrm{max}$. Table 4.1 lists the numerical values for μ, λ. For $\bar{\mu}, \bar{\lambda}$ as above, our minimum variance estimator becomes:

$$M_\mathrm{est}(< 1.8\, R_\mathrm{h}) \approx 3.5 \times 1.8\, R_\mathrm{h}\, G^{-1}\, \langle \sigma^2_\mathrm{los} \rangle \; . \tag{4.12}$$

This μ =const minimum variance estimator (equation 4.12) allows to constrain the enclosed mass $M(< 1.8\, R_\mathrm{h})$ with an uncertainty of $s/\bar{\mu} \approx 10$ per cent without making assumptions about the central slope of the underlying DM profile.

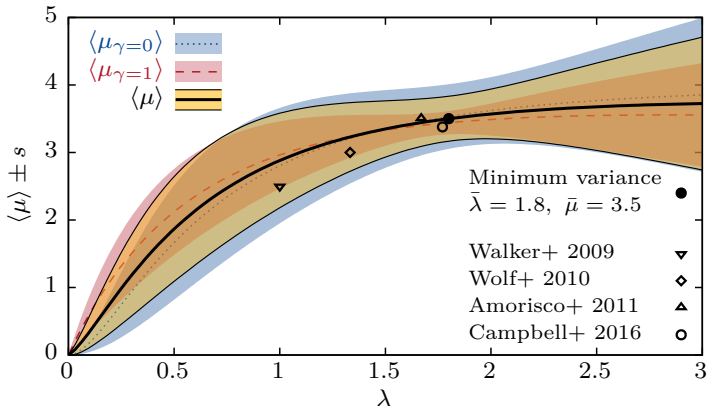

Figure 4.3: $\langle\mu_\gamma(\lambda)\rangle \pm s$ marginalized over segregation $0 \leq R_\mathrm{h}/r_\mathrm{max} \leq 1$ as a function of λ for stellar Plummer spheres with projected half-light radius R_h embedded in cored ($\gamma = 0$, blue dotted curve and blue shaded area) and cuspy ($\gamma = 1$, red dashed curve and red shaded area) $\{\alpha, \beta, \gamma\} = \{1, 5, \gamma\}$ DM profiles (equation 4.5). The black curve and yellow shaded area show $\langle\mu\rangle \pm s$ marginalized not only over segregation, but also over $0 < \gamma < 1$. The values $\bar{\lambda}, \bar{\mu}$ for our minimum variance estimator are indicated by a filled circle, whereas literature values for λ, μ are plotted using open symbols.

Table 4.1: Numerical values for λ and μ of equation 4.8. $\bar{\lambda}$ minimizes the squared relative error s^2/μ^2 when marginalizing both over $R_\mathrm{h}/r_\mathrm{max}$ and γ (equation 4.11). When marginalizing instead only over $R_\mathrm{h}/r_\mathrm{max}$, then $\lambda_{\gamma,\mathrm{min}}$ minimizes the squared relative error for a given γ, whereas for λ_eq, $\langle\mu_{\gamma=0}\rangle = \langle\mu_{\gamma=1}\rangle \equiv \mu_\mathrm{eq}$.

	$\bar{\lambda}$	$\bar{\mu}$	$\pm\, s$	λ_eq	μ_eq	$\pm\, s_\gamma$	$\bar{\lambda}_\gamma$	$\bar{\mu}_\gamma$	$\pm\, s_\gamma$
$\gamma = 0$	1.83	3.51	0.33	1.43	3.30	0.61	1.88	3.57	0.48
$\gamma = 1$						0.26	1.75	3.42	0.17

The numerical values of $\bar{\lambda}, \bar{\mu}$ depend on the choice of shape for the DM profile (in our case $\alpha = 1, \beta = 5$ and $0 \leq \gamma \leq 1$) and stellar profile (in our case Plummer spheres), as well as on the range of segregations $R_\mathrm{h}/r_\mathrm{max}$ and central slopes γ to marginalize over. Both $\bar{\lambda}_\gamma$ and $\bar{\mu}_\gamma$ differ by less than ten per cent between $\gamma = 0$ and $\gamma = 1$, i.e. the marginalization is fairly insensitive to the slope γ for the range of segregations chosen. Recall from Figure 4.1 that for highly segregated systems, $\mu_0(\lambda, R_\mathrm{h}/r_\mathrm{max} \to 0) \to 0$, whereas $\mu_1(\lambda, R_\mathrm{h}/r_\mathrm{max} \to 0) \to 3\lambda/2$. The larger variation of $\mu_\gamma(\lambda, R_\mathrm{h}/r_\mathrm{max})$ over the range of segregations for cored systems with respect to cuspy ones is reflected in the larger uncertainty $s_{\gamma=0}/\bar{\mu}_{\gamma=0} = 0.13$ compared to $s_{\gamma=1}/\bar{\mu}_{\gamma=1} = 0.05$

Other studies have found similar values for λ, μ using conceptually different approaches: Walker et al. (2009c) use Jeans analysis to motivate the choice of $\lambda = 1,\ \mu = 5/2$ under the assumption of isotropy and a constant projected velocity dispersion. Wolf et al. (2010) use Jeans analysis to estimate the mass enclosed within the 3D half-light radius using the approximation $r_\mathrm{h} = 4/3R_\mathrm{h}$, which translates to $\lambda = 4/3, \mu \approx 3$. Amorisco & Evans (2011, 2012) use a distribution-function approach to determine $\lambda \approx 1.67,\ \mu \approx 3.50$ for Michie-King models, measuring σ^2_los at the projected half-light radius. Campbell et al. (2017) find $\lambda \approx 1.77, \mu \approx 3.38$ empirically from a dispersion-supported sample of galaxies of the APOSTLE simulation project (Sawala et al., 2016), averaging σ^2_los within $1.04R_\mathrm{h}$.

4.3.2 Method comparison using *N*-body models

In the following, we will test the minimum variance estimator on a suite of N-body models taken from the controlled cosmological simulations introduced in chapter 3[5]. This suite of N-body models consists of re-simulations of the accretion of all subhaloes with $M > 10^8\,\mathrm{M}_\odot$ of the Aq-A2 merger tree (Springel et al., 2008) on to an evolving, analytical Milky Way-like host potential consisting of an NFW halo and an axisymmetric disc. Subhaloes are modelled as equilibrium N-body realizations of either cuspy or cored Dehnen profiles with 10^7 particles and injected in the host potential at z_infall, defined by the peak of their mass evolution. All subhaloes are re-simulated with the same number of N-body particles independent of their mass, and the spatial resolution of the particle-mesh code is chosen as a function of the scale radius of each subhalo. This re-simulation technique allows us to follow the dynamical evolution of accreted substructures with the same numerical resolution for systems spanning many orders of magnitude in mass and size, and limits the impact of artificial disruption as discussed by van den Bosch et al. (2018). The subhaloes of the Aquarius simulation are cuspy, and have mass distributions before accretion consistent with the Navarro et al. (1997) profile. We generate our cuspy and cored Dehnen equilibrium subhaloes keeping M_{200} as given by the Aquarius simulation. We obtain r_{-2} (i.e. the radius where $\mathrm{d}\ln\varrho/\mathrm{d}\ln r = -2$), which coincides with the NFW scale radius, from M_{200} using the median Prada et al. (2012) relation, and generate Dehnen models with that value of r_{-2}. We model the evolution of the stellar populations

[5] *In contrast to the set-up used in chapter 3, here we use 10^7 N-body particles per satellite, the spatial resolution of the highest-resolving grid of the particle mesh code equals $r_\mathrm{max}/128$, and the Miyamoto & Nagai (1975) galactic disc has mass and scales evolving with redshift as in Bullock & Johnston (2005), with M=0.025 M_{200}, a=3.5 kpc, b = 0.3 kpc at $z = 0$, where by M_{200} we denote the virial mass of the Aquarius Aq-A2 main halo, and by a, b the horizontal and vertical disc scale lengths, respectively. See section 3.A (p. 65) for further detail.*

under the assumption that they are collision-less and mass-less systems which only trace the underlying DM potential by assigning mass-to-light ratios to each N-body particle at infall, following the approach of Bullock & Johnston (2005). At $z = 0$, average observational properties of the stellar population, e.g. the velocity dispersion, can be obtained from the DM N-body particles by applying the initially assigned mass-to-light ratios as weights. We consider all haloes which at $z = 0$ host a stellar population in virial equilibrium, requiring that $|2K + W|/(2K - W) < 0.2$ for the DM enclosed within $r_{\rm max}$, and $|2K_{\rm los} + W_{\rm los}|/(2K_{\rm los} - W_{\rm los}) < 0.05$ for the stars. Masses and velocity dispersions are measured from these N-body haloes using bound particles only.

Fig. 4.4 shows the estimated enclosed masses $M(< \lambda R_{\rm h})$ of N-body models at $z = 0$ normalized by the true enclosed mass measured directly from the simulation as a function of segregation. The stellar population has a segregation of $R_{\rm h,0}/r_{\rm max,0} = 1/10$ at infall, which increases due to tides, spreading at $z = 0$ over an interval $1/10 \lesssim R_{\rm h}/r_{\rm max} \lesssim 1$ for cuspy, and $1/10 \lesssim R_{\rm h}/r_{\rm max} \lesssim 1/2$ for cored systems. In the top panel, we compare our minimum variance estimator ($\mu = 3.5, \lambda = 1.8$) against the

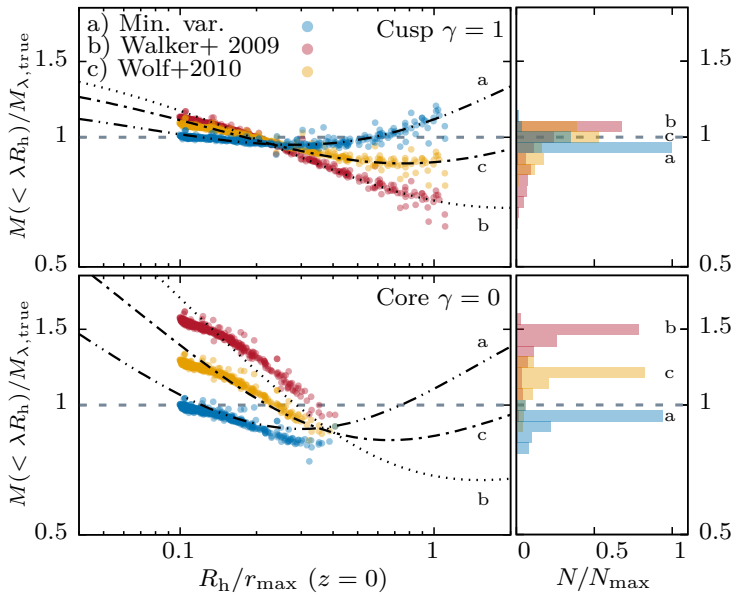

Figure 4.4: Estimated enclosed mass $M(< \lambda R_{\rm h})$ at $z = 0$ of N-body models taken from controlled re-simulations of the Aquarius A2 merger tree (see text), normalized by the true enclosed mass $M_{\lambda,\rm true}$ measured directly from the simulation, as a function of segregation $R_{\rm h}/r_{\rm max}$. The embedded stellar tracers have a segregation of $R_{\rm h,0}/r_{\rm max,0} = 1/10$ at infall. We compare our minimum variance estimator ($\mu = 3.5, \lambda = 1.8$) against the estimators of Walker et al. (2009c) and Wolf et al. (2010) separately for cuspy (top panel) and cored (bottom panel) DM haloes. Lines show the theoretical prediction of $M(< \lambda R_{\rm h})/M_{\lambda,\rm true}$ from the virial theorem for stellar Plummer spheres embedded in $\{\alpha, \beta, \gamma\} = \{1, 5, \gamma\}$ DM halo profiles. The panels on the right are histograms obtained when summing over all haloes of the simulation.

estimators of Walker et al. (2009c) and Wolf et al. (2010) for cuspy DM haloes, whereas cored ones are plotted in the bottom panel. Dotted lines show the theoretical prediction of $M(<\lambda R_{\rm h})/M_{\lambda,\rm true}$ from the virial theorem, i.e. $\mu_{\rm const}/\mu(\lambda, R_{\rm h}/r_{\rm max})$ for stellar Plummer spheres embedded in $\{\alpha,\beta,\gamma\}=\{1,5,\gamma\}$ DM halo profiles. The estimated masses follow closely the predictions of the virial theorem, which leads us to the conclusion that the main uncertainty on the estimated masses for a given DM profile shape originates from our ignorance on how deeply embedded the stellar population is within the DM halo. The scatter around the predicted curve is mainly caused by deviations of the DM halo shape from the assumed $\{1,5,\gamma\}$ profile. For the range of segregations shown, when marginalizing over the entire population of N-body mocks, the masses estimated from the minimum variance estimator are within ≈ 10 per cent of the true value. The other two estimators in question give a similar accuracy for cuspy systems. For cored systems, the Wolf et al. (2010) estimator overestimates masses of cored systems by ≈ 20 per cent, whereas the Walker et al. (2009c) estimator overestimates the masses of cored systems by ≈ 50 per cent. The uncertainties we find when estimating masses of cored haloes using $\mu=$ const mass estimators are notably larger than the uncertainties described in Campbell et al. (2017), derived from the APOSTLE simulations (Sawala et al., 2016), and González-Samaniego et al. (2017), based on the FIRE simulations (Hopkins et al., 2014). This is due to the fact the N-body haloes in these simulations follow mass profiles close to the cuspy Navarro et al. (1997) profile (for FIRE, see also Chan et al., 2015, discussing the core sizes as function of halo mass), whereas our cored haloes have a large core size equal to the DM scale radius.

4.4 Estimating the (total) halo mass

In the previous sections, we focused on determining the mass enclosed within multiples of the half-light radius of dwarf galaxies embedded in DM haloes using $\mu=$const mass estimators (equation 4.8). These estimators do not require to assume a specific DM profile when applying them to observational data - although the values of μ,λ can be motivated by a specific choice of profile, as done for the minimum-variance estimator, equation 4.12. We now focus on estimating the total halo mass from measurements of the stellar velocity dispersion $\langle\sigma^2_{\rm los}\rangle$ and the half-light radius $R_{\rm h}$.

4.4.1 Degeneracy of halo structural parameters

For a DM halo density profile $\varrho(r)$ with two free parameters, e.g. the total mass $M_{\rm tot}$ and a scale radius a for the profile of equation 4.5 with fixed $\{\alpha,\beta,\gamma\}$, the measurement of $\langle\sigma^2_{\rm los}\rangle$ and half-light radius $R_{\rm h}$ can be used to constrain one parameter as a function of the other, but is not sufficient to determine numerical values for both parameters simultaneously. Let us explore this degeneracy for the case of $\{\alpha,\beta,\gamma\}=\{1,5,\gamma\}$ DM

density profiles, i.e. DM profiles of tidally stripped systems, separately for the case of central DM cusps ($\gamma = 1$) and cores ($\gamma = 0$).

Extrapolating the enclosed mass

One way to obtain the degeneracy curve between the two halo structural parameters is to extrapolate the enclosed mass $M_{\rm est}(< \lambda R_{\rm h}) = \mu\lambda R_{\rm h}\langle\sigma^2_{\rm los}\rangle/G$ estimated using a μ=const mass estimator. The cumulative mass profile corresponding to the density profile of equation 4.5 with $\alpha = 1, \beta = 5$ reads

$$M(< r/a, \gamma) = M_{\rm tot}\left(\frac{r}{a} + 4 - \gamma\right)\left(\frac{r}{a}\right)^{3-\gamma}\left(\frac{r}{a} + 1\right)^{\gamma-4} \quad . \tag{4.13}$$

Defining $\tilde{M}(< r/a, \gamma) = M(< r/a, \gamma)/M_{\rm tot}$, which is a function of the radius r and the scale radius a in the combination r/a alone, the total mass extrapolated from the enclosed mass $M_{\rm est}(< \lambda R_{\rm h})$ then becomes

$$M_{\rm tot}(R_{\rm h}/a, \gamma) = M_{\rm est}(< \lambda R_{\rm h}/a)\ \tilde{M}^{-1}(< \lambda R_{\rm h}/a, \gamma)\ . \tag{4.14}$$

This total mass estimate is a function of the scale radius a of the DM halo, or equivalently of $r_{\rm max}$, using

$$r_{\rm max} = \frac{a}{2}\left(\sqrt{5\gamma^2 - 34\gamma + 57} + \gamma - 5\right)\ . \tag{4.15}$$

Equation 4.14 is defined for a specific DM profile shape and, for a given γ, can be written as a function of the segregation parameter $R_{\rm h}/r_{\rm max}$ alone, but relies on a μ =const mass estimate originally constructed to avoid the segregation dependence and the choice of a DM profile shape in the first place. Moreover, equation 4.4 tells us how to calculate μ directly from the virial theorem as a function of the segregation parameter and the choice of DM profile. This motivates to estimate the total mass directly from the virial theorem.

Total mass from the virial theorem

Consider the projected potential energy term $W_{\rm los}$ of the spherical virial theorem, equation 4.1. This term can be computed for given density profiles of the DM halo and the stellar tracer population. For $\{\alpha, \beta, \gamma\} = \{1, 5, \gamma\}$ profiles with convergent total mass $M_{\rm tot}$, we now define $\tilde{W}_{\rm los}(\gamma, R_{\rm h}/r_{\rm max}) = W_{\rm los}(M, \gamma, R_{\rm h}/r_{\rm max})/M_{\rm tot}$, which does depend on the scale $r_{\rm max}$ and inner slope γ but not on the total mass $M_{\rm tot}$ of the DM halo. Then, using equation 4.1, we find

$$M_{\rm tot}(R_{\rm h}/r_{\rm max}, \gamma) = -\langle\sigma^2_{\rm los}\rangle\ \tilde{W}^{-1}_{\rm los}(\gamma, R_{\rm h}/r_{\rm max})\ . \tag{4.16}$$

For given observed values of $\langle\sigma^2_{\rm los}\rangle$ and $R_{\rm h}$, and a choice of γ, the above equation for $M_{\rm tot}$ is a function of the segregation parameter $R_{\rm h}/r_{\rm max}$ alone.

$\{r_{\rm max}, v_{\rm max}\}$ degeneracy curves

To facilitate comparison with literature, this mass-segregation degeneracy can be cast as a one-dimensional degeneracy curve in the plane of the structural parameters $\{r_{\rm max}, v_{\rm max}\}$ of the DM halo, as first discussed by Peñarrubia et al. (2008a) for the case of stellar King profiles embedded in NFW haloes. For our case of tidally stripped systems with $\{\alpha, \beta, \gamma\} = \{1, 5, \gamma\}$ profiles, $v_{\rm max} = [GM(< r_{\rm max})/r_{\rm max}]^{1/2}$ is calculated from equation 4.13 using for the total mass either equation 4.14 (μ=const extrapolation) or equation 4.16 (virial theorem). When including observational errors, this degeneracy curve becomes equivalent to what Agnello & Evans (2012) named *virial stripe*. Fig. 4.5 compares the $\{r_{\rm max}, v_{\rm max}\}$ curves obtained directly from the virial theorem to the ones based on extrapolated masses using the Walker et al. (2009c) estimator, i.e. $\lambda = 1$ and using a constant $\mu = 5/2$ in equation 4.8. The curves are shown as an example for the Fornax dSph with a single stellar population[6] modelled as Plummer sphere with projected half-light radius $R_{\rm h} = (0.71 \pm 0.08)$ kpc and velocity dispersion $\sqrt{\langle \sigma^2_{\rm los} \rangle} = (9.2 \pm 1.1)\,{\rm km\,s^{-1}}$ (for references see Table 4.2) embedded in an $\{\alpha, \beta, \gamma\} = \{1, 5, \gamma\}$ DM halo. For low (high) values of $r_{\rm max}$, the virial theorem predicts larger (lower) values of $v_{\rm max}$ compatible with the same observed $\langle \sigma^2_{\rm los} \rangle$, $R_{\rm h}$. For the range of $r_{\rm max}$ shown in Fig. 4.5, the difference in the compatible values of $v_{\rm max}$ for the Fornax dwarf between the Walker et al. (2009c) and the virial theorem is below a factor of ~ 2.

[6] *More complete models have been discussed in the literature: Walker & Peñarrubia (2011) distinguish two and Amorisco et al. (2013) three distinct stellar populations in the Fornax dSph.*

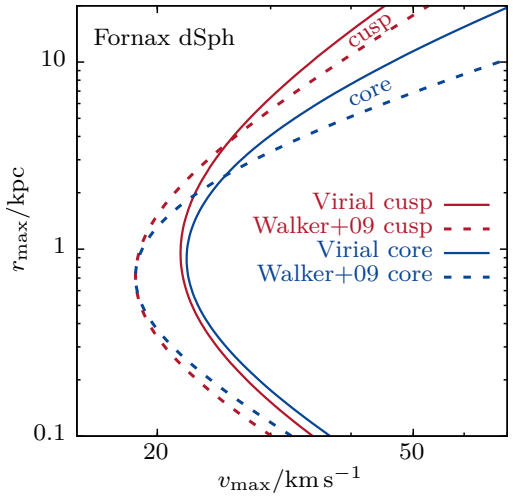

Figure 4.5: $\{r_{\rm max}, v_{\rm max}\}$ degeneracy curves for $\{\alpha, \beta, \gamma\} = \{1, 5, \gamma\}$ DM haloes compatible with the measurements of $\sqrt{\langle \sigma^2_{\rm los} \rangle} = (9.2 \pm 1.1)\,{\rm km\,s^{-1}}$ and $R_{\rm h} = (0.71 \pm 0.08)$ kpc of the Fornax dSph (for references see Table 4.2). Curves obtained directly from the virial theorem are compared to those based on mass estimates using the Walker et al. (2009c) estimator, shown separately for cuspy ($\gamma = 1$) and cored ($\gamma = 0$) DM profiles.

4.4.2 Breaking the degeneracy: halo parameters from controlled cosmological simulations

We aim to constrain the location of a DM halo hosting an observed dwarf galaxy along the $\{r_{\rm max}, v_{\rm max}\}$ degeneracy curve which is determined by the measured values of $\langle\sigma^2_{\rm los}\rangle$ and $R_{\rm h}$. We use controlled simulations of the formation of Milky Way-like DM haloes to model the population of subhaloes at $z = 0$. For each Milky Way dwarf of Table 4.2 we infer the values of $\{r_{\rm max}, v_{\rm max}\}$ consistent with the observed kinematics and the population of simulated subhaloes of our controlled simulations discussed in section 4.3.2. This allows us to put constraints on structural parameters like sizes and total masses of the DM haloes which host the Milky Way dwarfs for different assumptions about the population of DM subhaloes in the Milky Way. In specific we will study separately the cases in which the Milky Way DM halo population consists of DM subhaloes which were either cuspy or cored at accretion.

This approach of breaking the $\{r_{\rm max}, v_{\rm max}\}$ degeneracy is closely related to the method introduced by Peñarrubia et al. (2008a), where a cosmological $\{r_{\rm max}, v_{\rm max}\}$ relation for field haloes was used. Using a relation for field haloes neglects the effects of tidal stripping on the DM profiles as experienced by satellite galaxies like the Milky Way dSphs, which we do take into account by using $\{r_{\rm max}, v_{\rm max}\}$ values of simulated tidally stripped haloes. Fig. 4.6 shows the values of $\{r_{\rm max}, v_{\rm max}\}$ of the surviving population of simulated haloes at $z = 0$, separately for cuspy (left-hand panel) and cored (right-hand panel) models. We only consider simulated haloes where both the DM enclosed within $r_{\rm max}$ and the stars are approximately in virial equilibrium, requiring $|2K + W|/(2K - W) < 0.2$ for the DM, and $|2K_{\rm los} + W_{\rm los}|/(2K_{\rm los} - W_{\rm los}) < 0.05$ for the stars. When determining $r_{\rm max}$ and $v_{\rm max}$ of the N-body subhaloes, we consider bound particles only. The difference between cuspy and cored models becomes more pronounced with decreasing $v_{\rm max}$. Cored models are more extended than their cuspy counterparts for $v_{\rm max} \lesssim 20\,{\rm km/s}$, and the relation shows substantially more outliers than in the cored case. Also shown is the evolution of $\{r_{\rm max}, v_{\rm max}\}$ along *tidal tracks* (see Appendix 4.A) as a function of the fraction of remnant mass $M_{\rm max}$ enclosed within $r_{\rm max}$ with respect to the value at infall. Whereas cuspy systems evolve approximately along the initial $\{r_{\rm max}, v_{\rm max}\}$ relation, keeping the range of $\{r_{\rm max}, v_{\rm max}\}$ values at a given total halo mass rather narrow, cored systems evolve away from the initial relation, causing the larger observed scatter. While cored substructures are prone to disruption by tides, which explains the absence of systems with mass losses as high as for some cuspy models (see colour coding in Fig. 4.6), in this study, we do not match abundances of the simulated systems but structural parameters only, either by fitting the enclosed mass $M(< \lambda R_{\rm h})$ using a μ =const mass estimator, or by fitting the observed velocity dispersion $\langle\sigma^2_{\rm los}\rangle$.

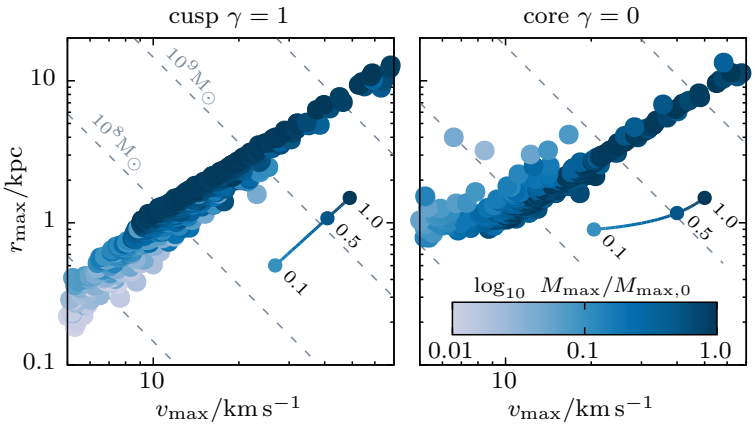

Figure 4.6: $\{r_{\rm max}, v_{\rm max}\}$ values of DM subhaloes at $z = 0$ of our controlled re-simulations of the Aquarius A2 merger tree. We model the accreted subhaloes to have either cuspy (left panel) or a cored (right panel) density profiles. The colour coding shows the mass $M_{\rm max}$ enclosed within $r_{\rm max}$ at $z = 0$ relative to the enclosed mass at infall. The solid curve and filled circles show the evolution within the $\{r_{\rm max}, v_{\rm max}\}$ plane along tidal evolutionary tracks (see Appendix 4.A), numbers denoting the fraction of remnant mass $M_{\rm max}$ enclosed within $r_{\rm max}$.

Fitting the enclosed mass $M(< \lambda R_{\rm h})$

When obtaining the $\{r_{\rm max}, v_{\rm max}\}$ degeneracy curve by extrapolating masses estimated through a μ =const mass estimator (see equation 4.14), it is a natural choice to break the degeneracy by selecting the simulated halo which matches best the estimated enclosed mass $M_{\rm est}(< \lambda R_{\rm h})$ computed from the observed values of $\langle \sigma^2_{\rm los} \rangle$ and $R_{\rm h}$. For each simulated halo, we measure $\{r_{\rm max}, v_{\rm max}\}$ and compute the mass $M_{\rm sim}(< \lambda R_{\rm h})$ assuming an $\{\alpha, \beta, \gamma\} = \{1, 5, \gamma\}$ profile with structural parameters $\{r_{\rm max}, v_{\rm max}\}$. We then select the halo which minimizes

$$\chi^2_{M(<\lambda R_{\rm h})} = \Big(M_{\rm est}(< \lambda R_{\rm h}) - M_{\rm sim}(< \lambda R_{\rm h}) \Big)^2 \; / \; {\rm var} \; , \tag{4.17}$$

where by var we denote the propagated variances from the observational uncertainties on $\langle \sigma^2_{\rm los} \rangle$ and $R_{\rm h}$. The variance is estimated through Monte-Carlo runs assuming Gaussian errors on $\langle \sigma^2_{\rm los} \rangle$ and $R_{\rm h}$ to account for the correlation between var($M_{\rm est}(< \lambda R_{\rm h})$) and var($M_{\rm sim}(< \lambda R_{\rm h})$) introduced by the uncertainty in $R_{\rm h}$.

Fitting the velocity dispersion $\langle \sigma^2_{\rm los} \rangle$

When obtaining the degeneracy curve directly from the viral theorem (equation 4.16), for each simulated halo with structural parameters $\{r_{\rm max}, v_{\rm max}\}$, we calculate the expected velocity dispersion $\langle \sigma^2_{\rm los,sim} \rangle$ from the virial theorem, using the observed

value of $R_{\rm h}$,

$$\langle \sigma^2_{\rm los,sim} \rangle = -W_{\rm los} = \frac{4\pi G}{3} \int_0^\infty r \nu_\star(r) M(<r)\, {\rm d}r \ . \tag{4.18}$$

In the above equation, $\nu_\star(r)$ is the density profile of a Plummer sphere, $\{\alpha_\star, \beta_\star, \gamma_\star\} = \{2, 5, 0\}$, with projected half-light radius $R_{\rm h}$, and $M(<r)$ is the cumulative mass profile for an $\{\alpha, \beta, \gamma\} = \{1, 5, \gamma\}$ DM halo with structural parameters $\{r_{\rm max}, v_{\rm max}\}$. We then confront this expected velocity dispersion $\langle \sigma^2_{\rm los,sim} \rangle$ to the observed velocity dispersion $\langle \sigma^2_{\rm los} \rangle$ by computing

$$\chi^2_{\langle \sigma^2_{\rm los} \rangle} = \left(\langle \sigma^2_{\rm los} \rangle - \langle \sigma^2_{\rm los,sim} \rangle \right)^2 \ / \ {\rm var} \ . \tag{4.19}$$

The variance term in the denominator is again obtained by Monte-Carlo sampling, assuming Gaussian errors on the observables $R_{\rm h}$ and $\langle \sigma^2_{\rm los} \rangle$.

4.4.3 Test of self-consistency using *N*-body models

Before applying the mass estimator to kinematic data of Milky Way dwarf galaxies in section 4.5.3, as a consistency check we recover the masses of the catalogue of N-body subhaloes described in section 4.3.2, i.e. we embed stellar populations in the same DM subhaloes which we use to break the $\{r_{\rm max}, v_{\rm max}\}$ degeneracy. In Fig. 4.7 we compare the masses estimated through direct $\langle \sigma^2_{\rm los} \rangle$ fits to masses extrapolated from μ =const estimators, assuming DM profiles with $\alpha = 1$ and $\beta = 5$ (see equation 4.5). The logarithms of the masses obtained from the virial estimator (black lines) are distributed approximately symmetrically around the true mass with $\langle \log_{10} M_{\rm tot}/M_{\rm true} \rangle = 0.0 \pm 0.2$ for cuspy systems, and 0.0 ± 0.2 (0.1 ± 0.5) for cored systems with an initial segregation of $R_{\rm h,0}/r_{\rm max,0} = 1/10$ (1/20).

On average, masses extrapolated from the three μ =const estimators are overestimated, i.e. $\langle \log_{10} M_{\rm tot}/M_{\rm true} \rangle > 0$ for all four subhalo catalogues. For masses extrapolated for cuspy systems from the minimum variance μ =const estimator introduced in section 4.3 we find $\langle \log_{10} M_{\rm tot}/M_{\rm true} \rangle \sim 0.0 \pm 0.3$, and $\lesssim 0.2 \pm 0.5$ for cored systems, i.e. bias and spread of the distribution are larger than for the masses obtained directly from the virial theorem. The bias $\langle \log_{10} M_{\rm tot}/M_{\rm true} \rangle$ is larger for the other two μ =const estimators. For systems with an initial segregation of 1/20, both the Walker et al. (2009c) and the Wolf et al. (2010) estimator give $\langle \log_{10} M_{\rm tot}/M_{\rm true} \rangle = 0.2 \pm 0.3$ (0.2 ± 0.6) for cuspy (cored) systems. Overall, we find larger biases and spreads in the distribution of recovered masses for cored systems than for cuspy ones. Cored systems do lose mass to tides more easily than cuspy systems, and their mass profiles show more extra-tidal features, i.e. our assumption of $\{\alpha, \beta, \gamma\} = \{1, 5, 0\}$ profiles does not match cored systems well which have lost large fractions of their initial mass.

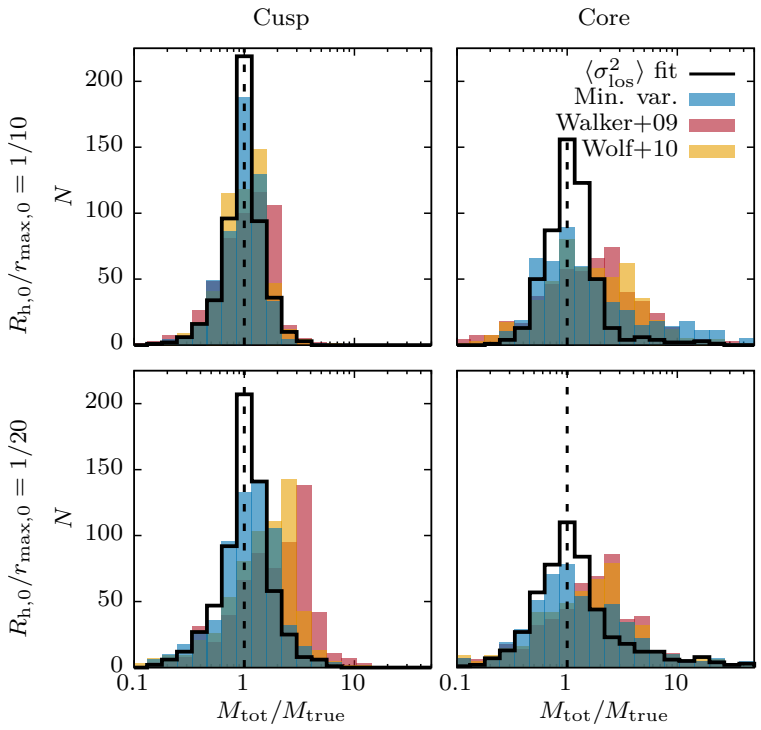

Figure 4.7: Histograms of estimated over true total halo mass $M_{\rm tot}/M_{\rm true}$ for four different catalogues of N-body subhaloes obtained from re-simulations of the Aquarius A2 merger tree: cuspy (cored) models are shown in the left (right) column, and the embedded stellar populations have an initial segregation of $R_{\rm h,0}/r_{\rm max,0} = 1/10$ (1/20) in the top row (bottom row). For each catalogue of N-body subhaloes, four different methods are used to estimate the total halo mass: direct fits of $\langle\sigma^2_{\rm los}\rangle$ (see equation 4.18), as well as masses extrapolated from three μ =const estimators, including the minimum variance estimator introduced in section 4.3.

4.5 Halo masses of Milky Way dSphs

We apply the minimum variance mass estimator to observational data of Milky Way dwarf galaxies compiled by McConnachie (2012) (supplemented with more recent measurements as detailed in Table 4.2) to infer the structural properties of DM haloes compatible with the observed values of $\langle\sigma^2_{\rm los}\rangle$ and $R_{\rm h}$. The velocity dispersions measured for Milky Way dSphs are often limited to one measurement per galaxy, e.g. the central velocity dispersion, or the velocity dispersion averaged within a certain radius, not necessarily up to infinity. Limited by the data available, for the following mass estimates we use the observed $\sigma_{\rm los,obs}$ as listed in McConnachie (2012) and assume $\sigma^2_{\rm los,obs} = \langle\sigma^2_{\rm los}\rangle$ in the notation of equation 4.2.

Table 4.2: Structural parameters for the brightest Milky Way dSphs. V-band luminosity $L_\star$, half-light radius R_h and line-of-sight velocity dispersion σ_los are taken from McConnachie (2012) unless indicated differently. References to the number of member stars N used for the computation of σ_los are listed at the bottom of the table. The mass $M_{1.8} \equiv M(< 1.8\,R_\mathrm{h})$ enclosed within 1.8 half-light radii R_h is estimated using the minimum-variance estimator of equation 4.12, which is subsequently used to obtain the mean density $\varrho_{1.8} \equiv \langle \varrho(< 1.8\,R_\mathrm{h}) \rangle$. *Continued on next page.*

	$\log_{10} \frac{L_\star}{\mathrm{L}_\odot}$	$\frac{R_\mathrm{h}}{\mathrm{kpc}}$	$\frac{\sigma_\mathrm{los}}{\mathrm{km\,s^{-1}}}$	N	$\log_{10} \frac{M_{1.8}}{\mathrm{M}_\odot}$	$\log_{10} \frac{\varrho_{1.8}}{\mathrm{M}_\odot \mathrm{kpc}^{-3}}$
Sagittarius dSph	$7.33^{+0.18}_{-0.18}$	2.62 ± 0.20	11.40 ± 0.70	114 [1]	$8.7^{+0.1}_{-0.1}$	$6.1^{+0.1}_{-0.1}$
Fornax	$7.31^{+0.19}_{-0.20}$	0.71 ± 0.08	11.70 ± 0.90	2633 [2]	$8.2^{+0.1}_{-0.1}$	$7.2^{+0.1}_{-0.1}$
Leo I	$6.74^{+0.17}_{-0.18}$	0.25 ± 0.03	9.20 ± 0.40 [3]	328 [3]	$7.5^{+0.1}_{-0.1}$	$7.9^{+0.1}_{-0.1}$
Sculptor	$6.36^{+0.25}_{-0.26}$	0.28 ± 0.04	9.20 ± 1.10 [2]	1541 [2]	$7.5^{+0.1}_{-0.1}$	$7.8^{+0.2}_{-0.2}$
Leo II	$5.87^{+0.17}_{-0.18}$	0.18 ± 0.04	6.60 ± 0.70	171 [4]	$7.0^{+0.1}_{-0.1}$	$7.9^{+0.2}_{-0.2}$
Sextans (I)	$5.64^{+0.24}_{-0.24}$	0.69 ± 0.04	7.90 ± 1.30	947 [2]	$7.8^{+0.1}_{-0.2}$	$6.9^{+0.1}_{-0.2}$
Carina	$5.58^{+0.25}_{-0.26}$	0.25 ± 0.04	6.60 ± 1.20	1982 [2]	$7.2^{+0.2}_{-0.2}$	$7.6^{+0.2}_{-0.2}$
Ursa Minor	$5.45^{+0.24}_{-0.24}$	0.18 ± 0.03	8.10 ± 1.10 [5]	235 [5]	$7.2^{+0.1}_{-0.1}$	$8.1^{+0.2}_{-0.2}$
Draco	$5.45^{+0.14}_{-0.15}$	0.22 ± 0.02	9.10 ± 1.20	413 [6]	$7.4^{+0.1}_{-0.1}$	$8.0^{+0.1}_{-0.1}$
Canes Venatici (I)	$5.37^{+0.12}_{-0.12}$	0.56 ± 0.04	7.60 ± 0.40	214 [7]	$7.7^{+0.1}_{-0.1}$	$7.0^{+0.1}_{-0.1}$
Crater 2	$5.21^{+0.04}_{-0.04}$ [8]	1.07 ± 0.08 [8]	2.70 ± 0.30 [9]	390 [9]	$7.1^{+0.1}_{-0.1}$	$5.6^{+0.1}_{-0.1}$
Leo T	$5.13^{+0.24}_{-0.24}$	0.12 ± 0.01	7.50 ± 1.60	19 [7]	$7.0^{+0.2}_{-0.2}$	$8.4^{+0.2}_{-0.2}$
Hercules	$4.57^{+0.19}_{-0.21}$	0.33 ± 0.06	3.72 ± 0.91 [10]	28 [10]	$6.8^{+0.2}_{-0.3}$	$6.9^{+0.3}_{-0.3}$
Bootes (I)	$4.46^{+0.11}_{-0.11}$	0.24 ± 0.02	2.40 ± 0.70	50 [11]	$6.3^{+0.2}_{-0.3}$	$6.8^{+0.2}_{-0.3}$
Leo IV	$4.27^{+0.19}_{-0.20}$	0.21 ± 0.04	3.30 ± 1.70	18 [7]	$6.5^{+0.4}_{-0.6}$	$7.2^{+0.4}_{-0.6}$
Ursa Major (I)	$4.14^{+0.16}_{-0.16}$	0.32 ± 0.05	7.60 ± 1.00	39 [7]	$7.4^{+0.1}_{-0.1}$	$7.5^{+0.2}_{-0.2}$
Leo V	$4.03^{+0.21}_{-0.21}$	0.13 ± 0.03	3.70 ± 1.85	7 [12]	$6.4^{+0.4}_{-0.6}$	$7.7^{+0.4}_{-0.6}$
Canes Venatici II	$3.90^{+0.22}_{-0.22}$	0.07 ± 0.01	4.60 ± 1.00	25 [7]	$6.4^{+0.2}_{-0.2}$	$8.4^{+0.2}_{-0.3}$
Ursa Major II	$3.61^{+0.31}_{-0.34}$	0.15 ± 0.02	6.70 ± 1.40	20 [7]	$7.0^{+0.2}_{-0.2}$	$8.1^{+0.2}_{-0.2}$
Coma Berenices	$3.57^{+0.27}_{-0.29}$	0.08 ± 0.01	4.60 ± 0.80	59 [7]	$6.4^{+0.2}_{-0.2}$	$8.3^{+0.2}_{-0.2}$
Willman 1	$3.01^{+0.42}_{-0.48}$	0.03 ± 0.01	4.30 ± 1.80	15 [14]	$5.8^{+0.3}_{-0.5}$	$9.2^{+0.4}_{-0.5}$
Bootes II	$3.01^{+0.38}_{-0.38}$	0.05 ± 0.02	10.50 ± 7.40	5 [13]	$6.9^{+0.4}_{-0.7}$	$9.5^{+0.5}_{-0.8}$
Segue II	$2.93^{+0.16}_{-0.16}$	0.03 ± 0.00	3.40 ± 1.85	5 [15]	$5.8^{+0.4}_{-0.6}$	$8.8^{+0.4}_{-0.6}$
Segue (I)	$2.53^{+0.39}_{-0.41}$	0.03 ± 0.01	3.90 ± 0.80	24 [16]	$5.8^{+0.2}_{-0.2}$	$9.0^{+0.3}_{-0.3}$

[1] Ibata et al. (1997) [2] Walker et al. (2009a) [3] Mateo et al. (2008) [4] Koch et al. (2007)
[5] Spencer et al. (2018) [6] Walker et al. (2007) [7] Simon & Geha (2007) [8] Torrealba et al. (2016)
[9] Caldwell et al. (2017) [10] Adén et al. (2009) [11] Koposov et al. (2011) [12] Walker et al. (2009b)
[13] Koch et al. (2009) [14] Martin et al. (2007) [15] Belokurov et al. (2009) [16] Geha et al. (2009)

Table 4.2 (continued): Structural parameters of the DM haloes, i.e. $r_{\rm max}$, $v_{\rm max}$ and total halo mass $M_{\rm tot}$, are obtained by fitting the observed velocity dispersion $\sigma_{\rm los}$ to the N-body subhaloes of our re-simulations of the Aquarius A2 merger tree, as discussed in section 4.4. These quantities are listed separately for fits to N-body subhaloes with cuspy ($\gamma = 1$) and cored ($\gamma = 0$) DM profiles. Total halo masses of N-body subhaloes are extrapolated from the mass $M_{\rm max}$ enclosed within $r_{\rm max}$ under the assumption of $\{\alpha, \beta, \gamma\} = \{1, 5, \gamma\}$-profiles. Uncertainties on $r_{\rm max}$, $v_{\rm max}$ and $M_{\rm tot}$ indicate the range of values of those N-body subhaloes which satisfy $\chi^2 \leq \chi^2_{\rm min} + 1$.

Cusp			Core			
$\frac{v_{\rm max}}{\rm km\,s^{-1}}$	$\frac{r_{\rm max}}{\rm kpc}$	$\log_{10}\frac{M_{\rm tot}}{\rm M_\odot}$	$\frac{v_{\rm max}}{\rm km\,s^{-1}}$	$\frac{r_{\rm max}}{\rm kpc}$	$\log_{10}\frac{M_{\rm tot}}{\rm M_\odot}$	
$21.8^{+1.4}_{-1.3}$	$2.0^{+1.1}_{-0.4}$	$8.8^{+0.2}_{-0.1}$	$21.5^{+0.7}_{-0.8}$	$2.9^{+0.1}_{-0.4}$	$8.9^{+0.0}_{-0.1}$	Sagittarius dSph
$23.4^{+5.5}_{-2.0}$	$2.3^{+2.2}_{-0.7}$	$8.9^{+0.5}_{-0.2}$	$31.7^{+26.6}_{-4.0}$	$4.6^{+8.8}_{-0.6}$	$9.4^{+1.0}_{-0.2}$	Fornax
$27.9^{+4.2}_{-6.4}$	$3.7^{+1.3}_{-1.8}$	$9.3^{+0.3}_{-0.5}$	$65.0^{+2.4}_{-0.0}$	$10.7^{+0.6}_{-0.0}$	$10.4^{+0.1}_{-0.0}$	Leo I
$27.2^{+4.9}_{-9.4}$	$3.9^{+1.1}_{-2.5}$	$9.3^{+0.2}_{-0.8}$	$65.0^{+8.6}_{-24.8}$	$10.7^{+3.7}_{-4.6}$	$10.4^{+0.2}_{-0.7}$	Sculptor
$16.9^{+9.9}_{-4.2}$	$1.6^{+2.4}_{-0.7}$	$8.5^{+0.8}_{-0.5}$	$65.0^{+8.6}_{-46.8}$	$10.7^{+3.7}_{-9.1}$	$10.4^{+0.2}_{-1.9}$	Leo II
$15.5^{+3.0}_{-3.5}$	$2.0^{+0.5}_{-1.1}$	$8.5^{+0.3}_{-0.5}$	$17.2^{+3.2}_{-4.5}$	$2.4^{+0.4}_{-1.1}$	$8.6^{+0.2}_{-0.5}$	Sextans (I)
$16.4^{+5.5}_{-6.5}$	$2.1^{+1.1}_{-1.6}$	$8.6^{+0.4}_{-1.0}$	$29.0^{+44.6}_{-16.0}$	$4.2^{+10.2}_{-3.0}$	$9.3^{+1.3}_{-1.2}$	Carina
$23.4^{+16.3}_{-5.7}$	$2.3^{+4.5}_{-0.9}$	$8.9^{+0.9}_{-0.5}$	$65.0^{+6.1}_{-24.8}$	$10.7^{+2.5}_{-4.6}$	$10.4^{+0.2}_{-0.7}$	Ursa Minor
$32.1^{+7.7}_{-11.9}$	$4.9^{+1.9}_{-3.3}$	$9.5^{+0.3}_{-0.8}$	$65.0^{+6.1}_{-16.7}$	$10.7^{+2.5}_{-3.1}$	$10.4^{+0.2}_{-0.4}$	Draco
$15.3^{+1.1}_{-1.9}$	$1.9^{+0.3}_{-0.9}$	$8.5^{+0.1}_{-0.4}$	$17.1^{+1.4}_{-2.1}$	$2.2^{+0.5}_{-0.6}$	$8.6^{+0.1}_{-0.2}$	Canes Venatici (I)
$5.9^{+0.6}_{-0.7}$	$0.4^{+0.0}_{-0.1}$	$7.0^{+0.1}_{-0.2}$	$5.2^{+1.4}_{-0.6}$	$0.9^{+3.1}_{-0.1}$	$7.2^{+0.8}_{-0.1}$	Crater 2
$37.5^{+21.3}_{-22.4}$	$6.2^{+5.0}_{-5.1}$	$9.8^{+0.6}_{-1.5}$	$18.2^{+55.4}_{-5.3}$	$1.6^{+12.8}_{-0.4}$	$8.5^{+2.2}_{-0.4}$	Leo T
$6.9^{+2.0}_{-1.8}$	$0.4^{+0.5}_{-0.2}$	$7.1^{+0.6}_{-0.6}$	$8.1^{+8.5}_{-2.7}$	$1.2^{+3.0}_{-0.4}$	$7.6^{+1.2}_{-0.5}$	Hercules
$4.4^{+1.3}_{-1.1}$	$0.2^{+0.2}_{-0.1}$	$6.4^{+0.5}_{-0.4}$	$5.7^{+2.8}_{-2.3}$	$1.1^{+2.1}_{-0.4}$	$7.3^{+0.8}_{-0.6}$	Bootes (I)
$6.4^{+4.7}_{-5.0}$	$0.5^{+0.8}_{-0.4}$	$7.2^{+0.9}_{-1.7}$	$10.2^{+8.2}_{-7.6}$	$1.8^{+2.4}_{-1.1}$	$8.0^{+0.8}_{-1.6}$	Leo IV
$16.4^{+7.1}_{-3.2}$	$1.5^{+2.0}_{-0.6}$	$8.5^{+0.7}_{-0.4}$	$24.7^{+48.9}_{-8.0}$	$3.1^{+11.3}_{-1.5}$	$9.0^{+1.6}_{-0.6}$	Ursa Major (I)
$8.1^{+8.4}_{-6.8}$	$0.7^{+1.5}_{-0.6}$	$7.5^{+1.1}_{-2.0}$	$14.0^{+59.6}_{-11.4}$	$1.7^{+12.7}_{-1.0}$	$8.3^{+2.4}_{-1.8}$	Leo V
$18.2^{+10.8}_{-10.7}$	$2.2^{+2.2}_{-1.9}$	$8.7^{+0.7}_{-1.6}$	$18.2^{+52.9}_{-5.3}$	$1.6^{+11.6}_{-0.4}$	$8.5^{+2.1}_{-0.4}$	Canes Venatici II
$23.7^{+8.4}_{-12.4}$	$3.3^{+1.7}_{-2.6}$	$9.1^{+0.4}_{-1.3}$	$65.0^{+8.6}_{-48.4}$	$10.7^{+3.7}_{-9.1}$	$10.4^{+0.2}_{-2.0}$	Ursa Major II
$17.2^{+9.6}_{-8.5}$	$2.0^{+2.0}_{-1.6}$	$8.6^{+0.7}_{-1.3}$	$18.2^{+49.2}_{-0.0}$	$1.6^{+9.7}_{-0.0}$	$8.5^{+2.0}_{-0.0}$	Coma Berenices
$58.8^{+11.3}_{-54.9}$	$11.3^{+3.0}_{-11.1}$	$10.4^{+0.3}_{-4.2}$	$18.2^{+55.4}_{-15.7}$	$1.6^{+12.8}_{-0.9}$	$8.5^{+2.2}_{-2.0}$	Willman 1
$63.0^{+7.1}_{-61.7}$	$8.9^{+5.3}_{-8.8}$	$10.4^{+0.3}_{-4.9}$	$18.2^{+55.4}_{-15.7}$	$1.6^{+12.8}_{-0.9}$	$8.5^{+2.2}_{-2.0}$	Bootes II
$22.0^{+36.9}_{-20.6}$	$3.1^{+8.2}_{-3.0}$	$9.0^{+1.4}_{-3.6}$	$18.2^{+55.4}_{-15.7}$	$1.6^{+12.8}_{-0.9}$	$8.5^{+2.2}_{-2.0}$	Segue II
$37.5^{+21.3}_{-28.8}$	$6.2^{+5.0}_{-5.9}$	$9.8^{+0.6}_{-2.5}$	$18.2^{+49.2}_{-7.7}$	$1.6^{+9.7}_{-0.5}$	$8.5^{+2.0}_{-0.7}$	Segue (I)

An ASCII version of this table is available at github.com/rerrani/dwarfs.

4.5.1 The tight correlation of enclosed mass and luminosity

In this section we show that enclosed mass $M(< 1.8\,R_\mathrm{h})$ and luminosity $L_\star$ of Milky Way dSph galaxies are tightly correlated, and that the effect of the tidal field of the Milky Way is small for the evolution of this correlation since accretion of the dwarfs. To estimate the enclosed mass within $\bar{\lambda} = 1.8$ half-light radii R_h, we use the minimum-variance μ =const estimator (equation 4.12). Fig. 4.8 shows the tight correlation between $L_\star$ and $M(< 1.8\,R_\mathrm{h})$, and numerical values are listed in Table 4.2. The faintest dwarfs of the sample with $L_\star \sim 10^3\,\mathrm{L}_\odot$ have enclosed masses of $\sim 10^6\,\mathrm{M}_\odot$, whereas the Fornax and Sagittarius[7] dwarf galaxies with $L_\star \sim 10^7\,\mathrm{L}_\odot$ have enclosed masses of the order $\sim 10^8\,\mathrm{M}_\odot$. The mean mass-to-light ratios $\langle M/L\rangle$ averaged within the respective half-light radii therefore decrease with luminosity and span a range of $1 \lesssim \log_{10}\langle M/L\rangle \lesssim 3$. This correlation has already been noted by Amorisco & Evans (2011, fig. 9), using the mass $M(< 1.7\,R_\mathrm{h})$ enclosed within 1.7 half-light radii, and McConnachie (2012), applying the Walker et al. (2009c) mass estimator and plotting masses enclosed within the half-light radius $M(< R_\mathrm{h})$ as a

[7] *The Sagittarius dwarf galaxy is close to pericentre and perturbed by tidal forces of the Milky Way halo and disc (see e.g. Peñarrubia et al., 2009; Łokas et al., 2010). Our mass estimates are derived under the assumption of virial equilibrium of the stellar tracer component, a requirement which is not guaranteed to hold for Sagittarius.*

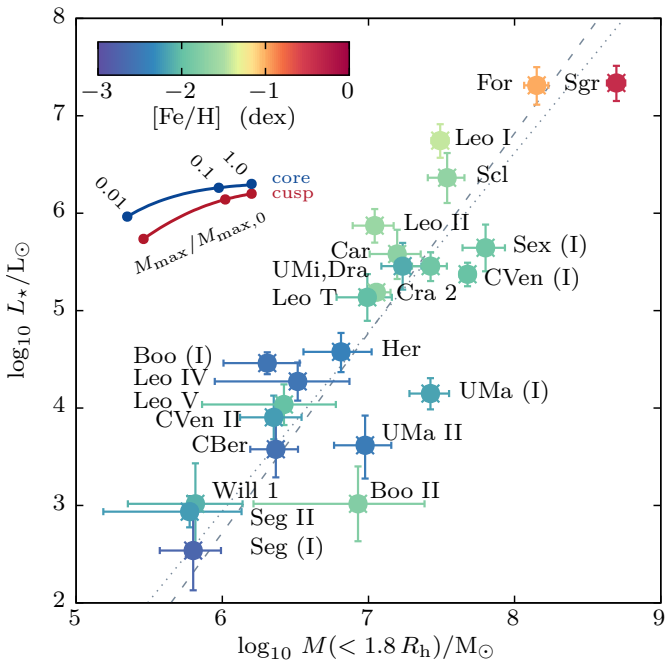

Figure 4.8: Luminosity $L_\star$ as a function of the mass $M(< 1.8\,R_\mathrm{h})$ enclosed within 1.8 half-light radii for Milky Way dwarf galaxies. Masses are estimated using the minimum-variance estimator (equation 4.12). The colour-coding shows metallicity Fe/H. Uncertainties are estimated by Monte Carlo sampling of symmetric Gaussian errors on $\langle\sigma^2_\mathrm{los}\rangle$ and R_h. The blue (red) solid curve shows the evolution along tidal tracks (see Appendix 4.A) for a stellar population with $R_{\mathrm{h},0}/r_{\mathrm{max},0} = 1/10$ embedded in a cored (cuspy) DM profile. The dashed (dotted) grey lines are power-law fits excluding (including) the Sagittarius dSph, see text. Numerical values are listed in table 4.2.

function of absolute V-band magnitude. Note that the luminosity $L_\star$ is not used in the inference of $M(< 1.8\,R_\mathrm{h})$, distinguishing this correlation from the relation between enclosed mass $M(< R_\mathrm{h})$ and half-light radius R_h discussed in Walker et al. (2009c). The correlation between $L_\star$ and $M(< 1.8\,R_\mathrm{h})$ can be fit by a power law of the form $L_\star/\mathrm{L}_\odot = 10^a \times [M(< 1.8\,R_\mathrm{h})/\mathrm{M}_\odot]^b$. Assuming symmetric uncertainties on $\log_{10} M(< 1.8\,R_\mathrm{h})$ and $\log_{10} L_\star$, we find $a = -9.6 \pm 2.3$, $b = 2.1 \pm 0.3$ when excluding the Sagittarius dSph from the fit, and $a = -8.1 \pm 1.7$, $b = 1.8 \pm 0.2$ when including it. The colour-coding of Fig. 4.8 shows the metallicity Fe/H of the dwarfs, which also increases with $M(< 1.8\,R_\mathrm{h})$.

Our results suggest that the correlation of $M(< 1.8\,R_\mathrm{h})$ and $L_\star$ is mainly driven by internal processes, i.e. star formation and feedback, and that tides through by Milky Way halo do have little effect on the relation. Solid lines in Fig. 4.8 show the evolution of luminosity and enclosed mass along tidal evolutionary tracks (see Appendix 4.A), i.e. as a function of the remnant mass fraction $M_\mathrm{max}/M_\mathrm{max,0}$, separately for the assumption of stellar populations embedded in cuspy and cored DM haloes. The initial segregation of the stellar populations is chosen to be $R_\mathrm{h,0}/r_\mathrm{max,0} = 1/10$. Dwarf galaxies evolving along these tidal tracks can lose up to two orders of magnitude of their mass M_max enclosed within r_max, or equivalently of their total mass under the assumption that the profile shape does not change, but experience a decrease in $M(< 1.8\,R_\mathrm{h})$ by only one order of magnitude. This is related to r_max decreasing during tidal stripping (see top panel of Fig. 4.A.1), which causes the mass enclosed within the central regions of the halo to decrease less rapidly than the total mass. As a consequence, the relation of luminosity and enclosed mass of Fig. 4.8 is not expected to broaden significantly during the tidal evolution of the dwarfs after accretion, and this holds both under the assumption of cuspy and cored DM halo profiles. However, internal processes like star formation will likely have an effect on the relation also after accretion, with star formation shown to be ongoing in some dSphs also after accretion - see e.g. de Boer et al. (2012), discussing that the latest star formation in the Fornax dwarf happened as recently as 250 Myrs ago.

4.5.2 Confronting measured densities and simulated haloes

When comparing the mean densities of ultrafaint Milky Way dwarfs to those of cored DM haloes taken from our re-simulations of the Aquarius A2 merger tree, we find that none of the simulated cored haloes are dense enough to host an ultrafaint Milky Way dwarf. We compute the mean density, averaged within a spherical volume of radius $1.8R_\mathrm{h}$, using the minimum variance mass estimator (equation 4.12):

$$\langle \varrho(< 1.8\,R_\mathrm{h})\rangle = M(< 1.8\,R_\mathrm{h})(4\pi/3)^{-1}(1.8\,R_\mathrm{h})^{-3}. \tag{4.20}$$

Fig. 4.9 shows the mean densities $\varrho(< 1.8\,R_\mathrm{h})\rangle$ as a function of half-light radius R_h, as well as the mean density profiles of the cuspy ($\gamma = 1$) and cored ($\gamma = 0$) DM haloes

of the controlled cosmological simulations of the formation of Milky Way-like haloes described in section 4.3.2. These profiles are obtained by determining $\{r_{\rm max}, v_{\rm max}\}$ for each simulated DM halo at $z = 0$, and assuming an $\{\alpha, \beta, \gamma\} = \{1, 5, \gamma\}$ profile with those values of $\{r_{\rm max}, v_{\rm max}\}$. Whereas for the re-simulation using cuspy subhaloes there are subhaloes with densities as high as the measured densities $\varrho(< 1.8\, R_{\rm h})\rangle$ of Milky Way dwarfs, in the case of cored simulations, none of the simulated haloes is dense enough to be compatible with the ultrafaint galaxies in the sample (see bottom panel of Fig. 4.9). Also shown in Fig. 4.9 is the evolution along tidal tracks (see Appendix 4.A) for a stellar population with an initial segregation of $R_{\rm h,0}/r_{\rm max,0} = 1/10$, assuming $L_\star \propto M_\star$. With half-light radii staying near constant, the evolution of the mean density for cuspy systems reflects the previously discussed behaviour that a system being stripped two orders of magnitude of its total mass only loses one order of magnitude of its enclosed mass $M(< 1.8 R_{\rm h})$, and therefore also $\langle\varrho(< 1.8\, R_{\rm h})\rangle$ drops by only one order of magnitude. The situation is notably different for dSphs embedded in cored DM haloes, which have half-light radii that expand during tidal stripping (see bottom panel of Fig. 4.A.1). For cored systems, losing two orders of magnitude of their total mass results in the average central density $\langle\varrho(< 1.8\, R_{\rm h})\rangle$ to drop by two orders of magnitude as well. As a consequence, if the ultrafaint galaxies of the sample did lose mass through tides previously, they must have been even denser in the past, rendering them even more incompatible with the cored DM haloes of our simulations. This tension is a consequence of our choice of core size of the simulated haloes. The cored subhaloes injected in the evolving host potential are modelled as Dehnen (1993) density profiles with $\gamma = 0$, i.e. density profiles where the core size is equal to the scale radius, chosen to highlight the different tidal evolution of cored substructures compared to cuspy ones. *Our findings therefore suggest that the ultra faint dwarfs require core sizes that are much smaller than the dark matter scale radius.*

It is interesting to note that increasing the mass of the host halo will not ease the difference between the measured densities and those of cored simulated haloes: whereas for cuspy density profiles, those systems with the highest total mass also have the highest densities (see Fig. 4.9, and Fig. 1.1), this does not hold for cored haloes. For the case of tidally evolved, cored $\{\alpha, \beta, \gamma\} = \{1, 5, 0\}$ profiles, from equation 4.13 we find for the central density $\varrho(0) = \varrho_s \propto M_{\rm tot}/a^3$. An empirical power-law fit to the relation between $M_{\rm tot}$ and the scale radius a, derived from the Aquarius A2 merger tree for systems with mass $\geq 10^8\,{\rm M}_\odot$, gives $a \propto M_{\rm tot}^{0.4}$. Consequently for these mass scales, the central density decreases with increasing mass. This result holds for the mass-size (or equivalently $\{r_{\rm max}, v_{\rm max}\}$) relation of the Aquarius merger tree. However note that in principle DM models which predict cored haloes may have different clustering properties and different mass-size relations compared to the choices made in this chapter, which will effect the densities of haloes in such DM models.

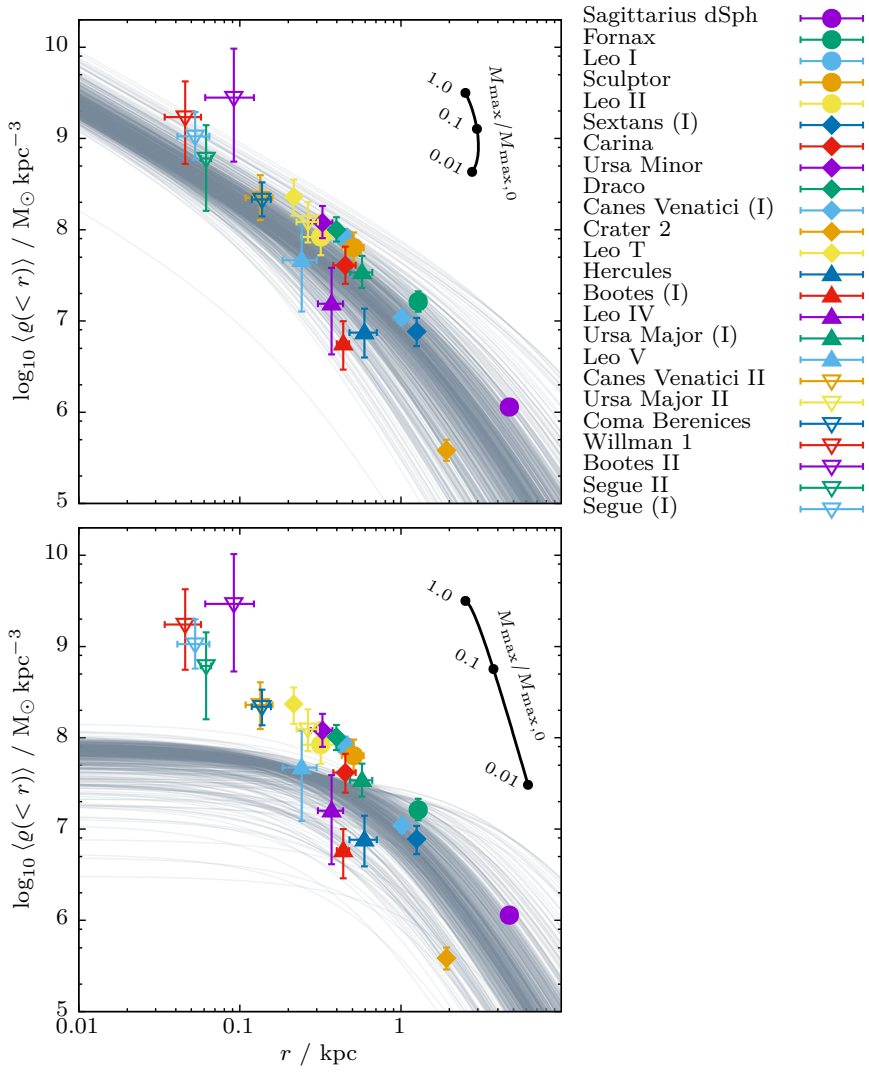

Figure 4.9: Mean densities $\varrho(< 1.8\,R_\mathrm{h})$ within 1.8 half-light radii R_h of Milky Way dSphs, estimated using the minimum-variance mass estimator (equation 4.12). Grey curves show the mean density profiles of cuspy ($\gamma = 1$, top panel) and cored ($\gamma = 0$, bottom panel) haloes of the controlled cosmological simulations introduced in section 4.3.2. These curves assume $\{\alpha, \beta, \gamma\} = \{1, 5, \gamma\}$ profiles with $\{r_\mathrm{max}, v_\mathrm{max}\}$ as fitted to the simulated haloes. Note that the ultrafaint Milky Way dwarfs are too dense to be compatible with any of the simulated cored DM haloes.

4.5.3 (Total) halo mass - stellar mass relation

Extrapolating total halo masses from measured enclosed masses is an uncertain endeavour: whereas enclosed masses within multiples of the half-light radius are well constrained by measurements of $\langle\sigma^2_{\rm los}\rangle$ and $R_{\rm h}$, constraints on the total halo mass are very weak ($\lambda \gg 1$ in Fig. 4.3). Total halo masses are therefore commonly extrapolated from enclosed masses under the assumption of median cosmological mass - concentration relations obtained for cuspy Navarro et al. (1997) profiles (see e.g. the discussion in Strigari et al. (2008), making use of the Bullock et al. (2001) relation between virial mass $M_{\rm vir}$ and $v_{\rm max}$ derived using cosmological N-body simulations). Tidally stripped systems do have density profiles with steep outer slopes ($\beta \approx 5$, see Peñarrubia et al., 2009, 2010, and Fig. 2.4 in this thesis) and convergent total masses, in contrast to the Navarro et al. (1997) profile of field haloes with outer slope $\beta = 3$ and a divergent total mass. Adding to this, following the tidal evolution of low-mass subhaloes is a challenging task for traditional cosmological simulation with fixed N-body particle mass, and recent studies call for caution regarding numerical convergence of these simulations (van den Bosch et al., 2018).

We infer the total halo mass of Milky Way dwarf galaxies by fitting the observed line-of-sight velocity dispersion $\langle\sigma^2_{\rm los}\rangle$ to N-body DM subhaloes extracted from a re-simulation of the Aquarius A2 merger tree, as described in section 4.4. Fig. 4.10 shows $\{r_{\rm max}, v_{\rm max}\}$ degeneracy curves constrained by the measurements of velocity dispersion $\langle\sigma^2_{\rm los}\rangle$ and half-light radius $R_{\rm h}$ for Milky Way dSph galaxies assuming cuspy ($\gamma = 1$) or cored ($\gamma = 0$) DM density profiles for tidally stripped systems ($\alpha = 1$, $\beta = 5$ in equation 4.5). The $\{r_{\rm max}, v_{\rm max}\}$ values of N-body subhaloes at $z = 0$ of our controlled simulations are depicted by grey filled circles, and the haloes corresponding to the minimum-χ^2 estimates (see equation 4.19) are indicated using crosses. Table 4.2 lists the inferred masses and structural parameters for the minimum-χ^2 estimate. For the case of cored DM profiles, the dwarfs Leo I and Segue (I) have $\chi^2_{\rm min} > 2$ and therefore result incompatible with all simulated subhaloes. Note that for cored systems, the $\{r_{\rm max}, v_{\rm max}\}$ degeneracy curves corresponding to ultrafaint galaxies do not intersect with any of the simulated cored DM haloes. Nevertheless the large observational uncertainties of the kinematics of these ultrafaint systems, for the case of cored DM profiles, we have $\chi^2_{\rm min} \gtrsim 0.3$ for all dwarfs with $L_\star < 10^4\,{\rm L}_\odot$.

Based on the inferred total halo masses $M_{\rm tot}$, we study the stellar- to halo mass relation of Milky Way satellite galaxies at $z = 0$. Using the rough approximation that on average $M_\star/{\rm M}_\odot \approx 1.5\,L_\star/{\rm L}_\odot$ (e.g. Martin et al., 2008), Fig. 4.11 shows the stellar- and total halo masses of MW dwarfs. While this approximation for $M_\star/{\rm M}_\odot$ is uncertain by a factor of the order of unity, the general trends discussed below regarding Fig. 4.11, spanning over several orders of magnitude in luminosity and mass, will not be effected by choosing a different mean stellar mass- luminosity ratio. Halo masses inferred under the assumption of cuspy and cored subhaloes are shown in the top and bottom panels, respectively. Errorbars show the minimum and maximum masses of

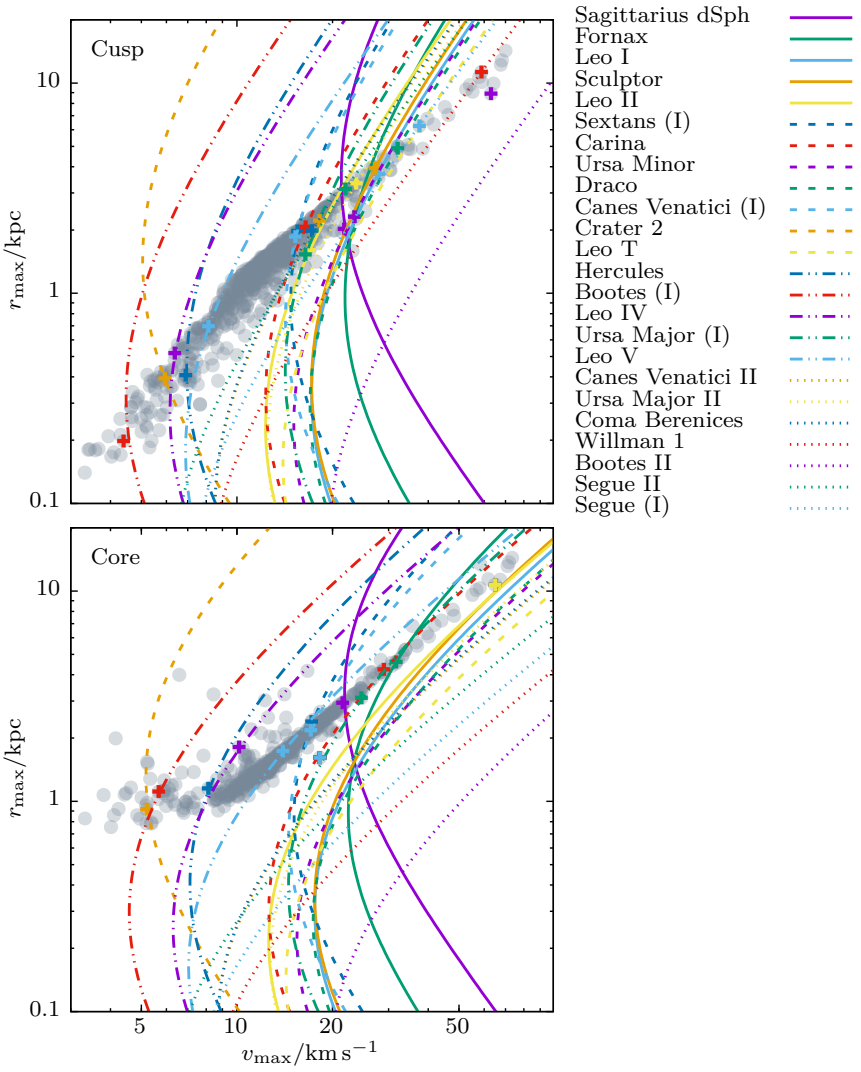

Figure 4.10: $\{r_{max}, v_{max}\}$ degeneracy curves of the DM haloes of Milky Way dSphs obtained by assuming cuspy (top panel, $\gamma = 1$) and cored (bottom panel, $\gamma = 0$) DM density profiles for tidally stripped systems ($\alpha = 1$, $\beta = 5$ in equation 4.5). $\{r_{max}, v_{max}\}$ values of subhaloes of our controlled cosmological simulations are shown by grey filled circles. Crosses indicate the minimum-χ^2 estimates (see equation 4.19). Note that the $\{r_{max}, v_{max}\}$ curves of the ultrafaint Milky Way dwarfs result incompatible with any of the simulated cored DM haloes.

simulated subhaloes which satisfy $\chi^2 < \chi^2_{\rm min} + 1$. The stellar- to halo mass relations by Moster et al. (2010), Behroozi et al. (2013) and Sawala et al. (2016) are plotted using dashed grey lines, showing M_{200} as a proxy to the total halo mass (which for NFW, i.e. non-tidally stripped profiles with $\beta = 3$, is diverging). Note that for satellite galaxies, these relations refer to the peak (i.e. maximum) halo mass the satellite reached before being tidally stripped. For systems with $\log_{10} L_\star/\mathrm{L}_\odot \gtrsim 5$, our findings are compatible with all three stellar- to halo mass relations shown. For the case of the Sagittarius and the Fornax dSphs, our inferred masses are smaller by one order of magnitude than the halo mass predictions for field haloes given the observed luminosities. In general, for the case of cuspy subhaloes, all classical Milky Way dSphs have inferred masses at the low-mass end of the abundance matching relations shown. This discrepancy is consistent with our understanding of the tidal evolution of dSph galaxies: when being accreted on to a larger galaxy, dSph galaxies initially lose predominantly DM and not stars, which are embedded deeply inside the galaxies' potential and are therefore less prone to stripping (see e.g. Peñarrubia et al., 2008b). The tidal evolutionary tracks shown in Fig. 4.11 and discussed in Appendix 4.A show that dSphs with both cuspy and cored DM profiles can be stripped one order of magnitude of their dynamical mass due to tides while losing less than ten per cent of their stellar mass. Note also that the correlation between luminosity and enclosed mass $M(< 1.8\, R_{\rm h})$ (see Fig. 4.8) is notably tighter than the correlation found between stellar mass and total halo mass. This could be a consequence of the tidal evolution of the dwarfs: if at infall stellar mass and total halo mass were more tightly correlated, tides may have stripped significant fractions of DM but not of stars, as consistent with the tidal tracks for highly segregated stellar populations.

4.5.4 Puzzling halo masses for ultrafaint dwarfs

For systems with $\log_{10} L_\star/\mathrm{L}_\odot \lesssim 5$, we find an anticorrelation between stellar mass and halo mass, associating the faintest galaxies to the most massive haloes. For cored systems, Milky Way dwarf galaxies with luminosities spanning between $2 \lesssim \log_{10} L_\star/\mathrm{L}_\odot \lesssim 4$ are associated to the DM haloes of mass of $\sim 10^9 \mathrm{M}_\odot$, with an uncertainty of two orders of magnitude and $\chi^2_{\rm min} \gtrsim 0.3$. The corresponding $\{r_{\rm max}, v_{\rm max}\}$ degeneracy curves of Fig. 4.10 do not intersect with any $\{r_{\rm max}, v_{\rm max}\}$ value measured from the cored simulations. Note that dwarf galaxies evolving along the tidal tracks shown in Fig. 4.11 primarily lose DM and not stellar mass, and move away from the stellar mass- halo mass relation found for ultrafaints, i.e. tidal evolution cannot be at the origin of the observed anticorrelation.

There are however observational challenges which might be related to this counter-intuitive anticorrelation:

(i) Inflated masses might result from inflated velocity dispersion measurements: a striking example being the Hercules dSph, where Adén et al. (2009) found

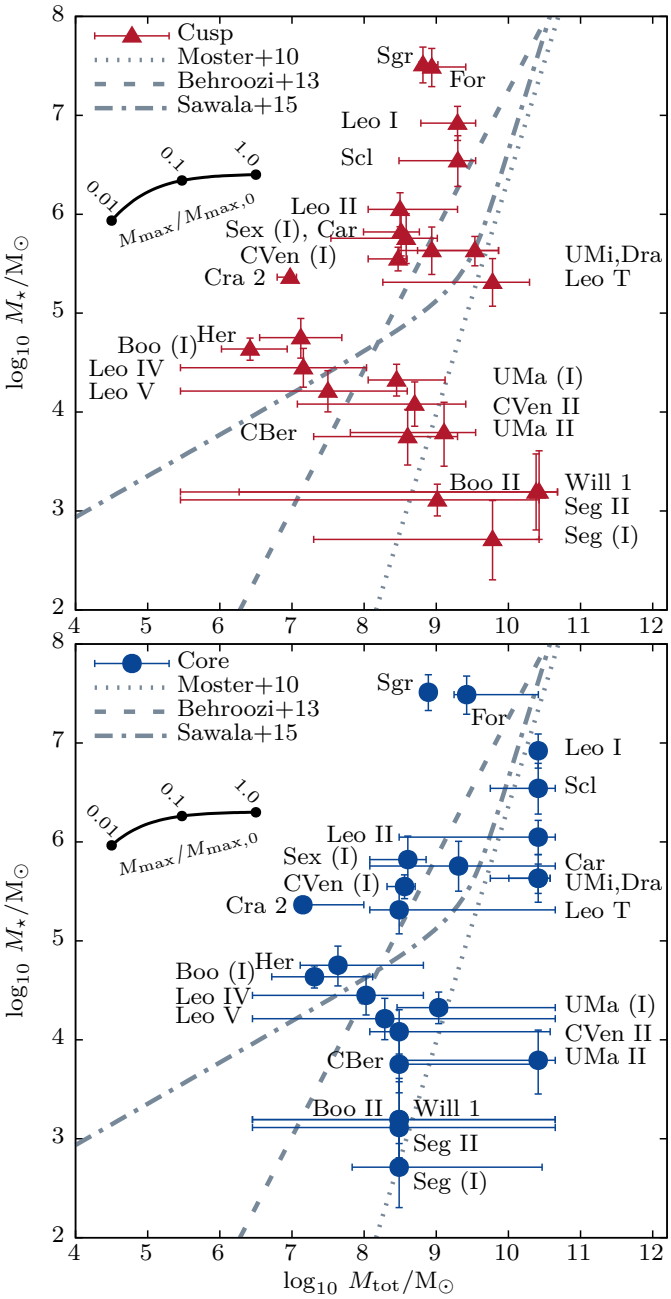

Figure 4.11: Stellar- and total halo masses inferred for Milky Way dwarf galaxies (McConnachie, 2012) by fitting the observed velocity dispersion $\langle\sigma^2_{los}\rangle$ to the catalogue of subhaloes of our re-simulations of the Aquarius A2 merger tree. Abundance matching relations (Moster et al., 2010; Behroozi et al., 2013; Sawala et al., 2015) are shown as grey dashed lines. The black solid lines show the median evolution of $M_\star$ following the tidal tracks of Appendix 4.A as a function of the fraction of remnant mass M_{max} enclosed within r_{max}.

a reduction by roughly half from $7.33 \pm 1.08 \mathrm{km\,s^{-1}}$ to $3.72 \pm 0.91\,\mathrm{km\,s^{-1}}$ after removing foreground contaminants. In comparison, Simon & Geha (2007) computed a dispersion of $5.1 \pm 0.9\,\mathrm{km\,s^{-1}}$.

(ii) Similarly, peculiar velocities due to binary motion add to the observed velocity dispersion (see e.g. McConnachie & Côté, 2010).

(iii) Low-number statistics for systems with few stellar tracers add to the uncertainty on the estimated dispersion. Table 4.2 lists the number N of stars with measured velocities used to infer the dispersion σ_{los}. Most dwarfs with luminosity $L_\star \lesssim 10^5\,\mathrm{L_\odot}$ have fewer than 50 member stars with measured velocities, the only exceptions being Bootes (I) with ~ 50 member stars and Coma Berenices with 59 stars. The ultrafaint dwarfs in the sample with $L_\star \lesssim 10^3\,\mathrm{L_\odot}$ have less than 25 member stars with measured velocities, Bootes II and Segue II having only five member stars each. Following Laporte et al. (2019, table 1), for seven stars and a ratio between measured dispersion and measurement error of $\sigma/\varepsilon_v = 2.0$, the uncertainty on the inferred velocity dispersion due to sample size is ~ 50 per cent, whereas for 51 member stats, the uncertainty is ~ 25 per cent.

Furthermore, there are several systematic aspects of our method which call for caution.

(i) All our analysis is based on the virial theorem and thereby assumes dynamical equilibrium of the underlying stellar tracer component. Some dSphs do show extra-tidal (i.e. possibly non-equilibrium) features, and the applicability of the virial theorem is then limited to the virialized core of the systems.

(ii) We infer total halo masses of Milky Way dwarfs by selecting subhaloes extracted from simulations of Milky Way-like DM haloes compatible with the observed kinematics. For this purpose, we re-simulated a single merger tree of the Aquarius simulation. Cosmic variance will allow for a wider range of accretion scenarios, and possibly for a wider range of $\{r_{\mathrm{max}}, v_{\mathrm{max}}\}$ values at $z = 0$. This may increase the number of haloes compatible with the observed kinematics. Moreover, we use the same $\{r_{\mathrm{max}}, v_{\mathrm{max}}\}$ relation at infall for both cuspy and cored models, whereas in principle DM models that result in cored haloes may have different clustering properties and $\{r_{\mathrm{max}}, v_{\mathrm{max}}\}$ relations compared to their cuspy counterparts.

(iii) The Aquarius A2 main halo has a virial mass of $1.84 \times 10^{12}\,\mathrm{M_\odot}$, which is larger by a factor ~ 2 than estimates of the (total) Milky Way mass derived by use of the timing argument (Peñarrubia et al., 2016a). Therefore also the simulated subhaloes, which we use to break the $\{r_{\mathrm{max}}, v_{\mathrm{max}}\}$ degeneracy of Milky Way dSphs, might have on average higher masses than Milky Way subhaloes.

(iv) We infer masses separately under the assumption of cuspy and cored DM profiles, using a single choice of core size. Different core sizes are motivated by various

physical models for core formation. Our choice to model the subhaloes at infall as Dehnen (1993) profiles with $\gamma = 0$ and $\gamma = 1$ are extreme cases, but as shown in Fig. 4.11, the impact of the assumed core size on the inferred total halo masses is relatively small.

4.5.5 Comparison with other studies

The masses enclosed within the luminous radii of dwarf galaxies have been extensively discussed in the literature, and the enclosed masses $M(< 1.8\,R_\mathrm{h})$ estimated using the minimum variance estimator (equation 4.12) listed in Table 4.2 differ at most by factors of order of unity from the mass estimates in Walker et al. (2009c), Wolf et al. (2010), Amorisco & Evans (2011), McConnachie (2012) when extrapolated to the same radius. The differences are due to i) differently motivated choices of the factors μ, λ (see equation 4.4) and ii) updated velocity dispersion measurements.

Following Mateo et al. (1993), Strigari et al. (2008) and Wolf et al. (2010) discuss a single mass scale of $\sim 10^9\,\mathrm{M}_\odot$ for the total masses of all Milky Way dwarf galaxies, making use of cosmological mass-size relations for cuspy haloes to extrapolate the total mass from masses enclosed within 300 pc and the deprojected half-light radius, respectively. This mass scale is in agreement with the total masses we derive for most Milky Way dSphs, however on the low-mass end, we derive total masses of $\sim 10^7\,\mathrm{M}_\odot$ for Crater 2, Hercules and Leo IV and $\sim 10^6\,\mathrm{M}_\odot$ for Bootes (I). In the following we compare our mass estimates (as listed in Table 4.2) for four selected Milky Way dwarf galaxies against other studies.

Fornax ($L_\star \approx 2 \times 10^7\,\mathrm{L}_\odot$)

We infer an enclosed mass of $M_\mathrm{est}(< 1.8\,R_\mathrm{h}) = (1.4^{+0.3}_{-0.3}) \times 10^8\,\mathrm{M}_\odot$ for Fornax and, assuming a cuspy $\{\alpha, \beta, \gamma\} = \{1, 5, 1\}$ DM profile for tidally stripped systems, a total halo mass of $M_\mathrm{tot} = (8.7^{+16.9}_{-3.0}) \times 10^8\,\mathrm{M}_\odot$. For a cored $\{1, 5, 1\}$ DM profile, we find $M_\mathrm{tot} = (2.6^{+23.1}_{-0.9}) \times 10^9\,\mathrm{M}_\odot$. For models where mass follows light, Łokas (2009) obtain through Jeans modelling a total mass of $(1.6 \pm 0.1) \times 10^8\,\mathrm{M}_\odot$, lower than our total mass estimate by an order of magnitude, and more similar to our estimated enclosed mass. The best-fitting model of Diakogiannis et al. (2017) is as well a model where mass follows light, with total mass and uncertainty equal to the value of Łokas (2009). From a distribution function based approach Pascale et al. (2018) find total masses of $(2.1 \pm 0.1) \times 10^8\,\mathrm{M}_\odot$ for models where mass follows light, $(5.8^{+1.9}_{-1.1}) \times 10^9\,\mathrm{M}_\odot$ for a cuspy DM profile and $(9.5^{+12}_{-2}) \times 10^9\,\mathrm{M}_\odot$ for their best-fitting cored model. All DM halo models considered have convergent total masses, but outer slopes of $\beta = -\mathrm{d}\ln\varrho/\mathrm{d}\ln r \approx 3$. Consequently these systems have slowly converging total masses[8]. We assume an outer slope of $\beta = 5$ for tidally stripped systems, with much more rapidly converging total mass. The enclosed mass $M(< 1.7\,R_\mathrm{h}) = (1.4 \pm 0.1) \times 10^8\,\mathrm{M}_\odot$ inferred by Pascale et al. (2018) is in good agreement with our estimate from the virial theorem using $\mu(\lambda = 1.7) = 3.46$ (see Fig. 4.3): $M_\mathrm{est}(< 1.7\,R_\mathrm{h}) = (1.3 \pm 0.3) \times 10^8\,\mathrm{M}_\odot$.

[8] *Note that for $r/a \gg 1$, the NFW outer slope of $\beta \equiv 3$ leads to a diverging total mass $M(< r/a) \propto \ln(r/a)$.*

Sculptor ($L_\star \approx 2 \times 10^6\,\mathrm{L}_\odot$)

The enclosed mass we infer for Sculptor, $M(< 1.8\,R_\mathrm{h} = (3.5^{+1.1}_{-0.9}) \times 10^7\,\mathrm{M}_\odot$, is again close to the total mass quoted by Łokas (2009) for models where mass follows light, $(3.1 \pm 0.2) \times 10^7\,\mathrm{M}_\odot$. Strigari et al. (2017) use a distribution function based approach to conclude that observed stellar velocities in the Sculptor dwarf are consistent with an NFW DM halo with a maximum circular velocity of $20 < v_\mathrm{max}/\mathrm{km\,s^{-1}} < 35$. This is similar to the range of maximum circular velocities we find under the assumption of cuspy $\{1, 5, 1\}$ profiles, $18 \lesssim v_\mathrm{max}/\mathrm{km\,s^{-1}} \lesssim 32$. This corresponds to a total halo mass of $M_\mathrm{tot} = (2.0^{+1.6}_{-1.7}) \times 10^9\,\mathrm{M}_\odot$. For cored $\{1, 5, 0\}$ profiles, we find $40 \lesssim v_\mathrm{max}/\mathrm{km\,s^{-1}} \lesssim 74$, and $M_\mathrm{tot} = (2.6^{+1.9}_{-2.1}) \times 10^{10}\,\mathrm{M}_\odot$.

Carina ($L_\star \approx 4 \times 10^5\,\mathrm{L}_\odot$)

For the Carina dwarf, we obtain an enclosed mass of $M_\mathrm{est}(< 1.8\,R_\mathrm{h}) = (1.6^{+0.7}_{-0.6}) \times 10^7\,\mathrm{M}_\odot$, similar to the total mass inferred by Łokas (2009) $(2.3 \pm 0.2) \times 10^7\,\mathrm{M}_\odot$ under the assumption that mass follows light. Non-equilibrium N-body models of the Carina dwarf have been studied by Ural et al. (2015). They model the DM distribution of Carina separately under the assumption of cuspy ($\gamma = 1$) and cored ($\gamma = 0$) Dehnen (1993) profiles, i.e. $\{\alpha, \beta, \gamma\} = \{1, 4, \gamma\}$. For the cuspy model, they find a total halo mass at $z = 0$ of $4.0^{+4.1}_{-2.4} \times 10^8\,\mathrm{M}_\odot$. This result is consistent with the total mass we find under the assumption of virial equilibrium and a $\{\alpha, \beta, \gamma\} = \{1, 5, 1\}$ DM profile, namely $3.8^{+6.4}_{-3.5} \times 10^8\,\mathrm{M}_\odot$. For the cored model, Ural et al. (2015) find a total mass of $3.5^{+3.9}_{-2.3} \times 10^8\,\mathrm{M}_\odot$. Our cored model for the Carina dSph is particularly poorly constrained (see bottom panel of Fig. 4.10), and a large range of simulated haloes with masses spanning $1.2 \times 10^8 \; - \; 4.5 \times 10^{10}\,\mathrm{M}_\odot$ result compatible with the observed kinematics.

Hercules ($L_\star \approx 4 \times 10^4\,\mathrm{L}_\odot$)

On the low-mass end of Milky Way satellites, for the Hercules dwarf, we find an enclosed mass of $M_\mathrm{est}(< 1.8 R_\mathrm{h})/\mathrm{M}_\odot = 6.5^{+4.0}_{-2.9} \times 10^6$. To compare this value against the mass $M < (0.3\,\mathrm{kpc})/\mathrm{M}_\odot = 1.9^{+1.1}_{-0.8} \times 10^6$ inferred by Adén et al. (2009), we use the general form of the virial mass estimator (equation 4.8) with $\mu(\lambda = 0.3\,\mathrm{kpc}/R_\mathrm{h}) \approx 2.7$ (see Fig. 4.3). We find $M_\mathrm{est}(< 0.3\,\mathrm{kpc})/\mathrm{M}_\odot = 2.6^{+1.8}_{-1.2} \times 10^6$, in good agreement with the findings of Adén et al. (2009).

4.6 Summary and discussion

Mass estimators for pressure-supported systems play an important role in constraining the distribution of dark matter (DM) on the scale of dSphs. Kinematic data for these systems is often limited to velocity dispersion measurements $\sigma_{\rm los}(r)$ along the line of sight. The challenge lies in constructing an estimator which does not rely on strong assumptions about quantities inaccessible to observation. In this chapter, we construct an estimator for the mass enclosed within 1.8 multiples of the projected half-light radius $R_{\rm h}$ of the stellar tracer population (equation 4.12):

$$M_{\rm est}(< 1.8\,R_{\rm h}) \approx 3.5 \times 1.8\,R_{\rm h}\,G^{-1}\,\langle\sigma^2_{\rm los}\rangle\ ,$$

where by $\langle\sigma^2_{\rm los}\rangle = 2K$ we denote the luminosity-averaged squared line-of-sight velocity dispersion of the stellar tracer population. This estimator is based on the projected virial theorem and minimizes the uncertainty on the inferred masses arising from our ignorance on (i) the central slope γ of the DM profile, as well as on (ii) how deeply embedded the stellar tracer population is within the DM halo. The estimator has been tailored to give accurate masses for tidally stripped dwarf galaxies, which follow density profiles that scale as $\varrho(r) \propto r^{-5}$ at large radii (see e.g. Fig. 2.4).

The use of the projected virial theorem has several advantages over the Jeans equations for the construction of mass estimators:

(i) Our method does not suffer from the mass - anisotropy degeneracy. The Jeans equations depend on information about the anisotropy of the velocity dispersion, parametrized by the function $\beta(r) \equiv 1 - \sigma^2_{\rm los}(r)/\sigma^2_{\perp}(r)$, therefore requiring knowledge about the velocity dispersion component $\sigma_{\perp}(r)$ orthogonal to the line of sight. The form of $\beta(r)$ might be different for each stellar population, and could be more complicated than a simple monotonic function of radius. Our ignorance of $\beta(r)$ gives rise to the infamous mass - anisotropy degeneracy. The projected virial theorem $2K_{\rm los} + W_{\rm los} = 0$ instead makes use of the luminosity-averaged squared line-of-sight velocity dispersion $\langle\sigma^2_{\rm los}\rangle = 2K$, accessible to observation.

(ii) Systematic biases of inferred enclosed masses $M_{\rm est}(< 1.8\,R_{\rm h})$ and derived central slopes γ are straightforward to estimate: they follow directly from the assumptions on the DM and stellar density profiles, and do not rely on assumptions on the difficult to constrain form of $\beta(r)$.

(iii) The average squared dispersion $\langle\sigma^2_{\rm los}\rangle$ is a sum over all stars and does not require data to be binned. It therefore can be robustly computed also for systems with a low number of stars - carefully modelling the uncertainties due to sample size as pointed out by Laporte et al. (2019).

However, the application of the virial theorem in this context requires to specify a (family of) DM mass distributions, i.e. the estimated enclosed masses are model

dependent. The bias of the derived masses is predominantly driven by how deeply embedded the stellar tracer is within the DM halo. For this reason, masses enclosed within multiples of the half-light can be determined fairly accurately, whereas the total halo mass is only weakly constrained from measurements of $\langle\sigma^2_{\rm los}\rangle$ and $R_{\rm h}$ alone (see Fig. 4.3 for $\lambda \gg 1$).

We have tested the mass estimator on a suite of N-body mocks extracted from controlled re-simulations of the Aquarius A2 merger tree, and recover the enclosed masses with an accuracy of $\lesssim 10$ per cent in systems with mass-loss fractions that differ by orders of magnitude. The re-simulations cover all subhaloes of the merger tree with masses at infall $\geq 10^8\,{\rm M}_\odot$, and model each subhalo with the same number of 10^7 N-body particles independent of its mass. This set-up allows us to follow the tidal evolution of subhaloes spanning many orders of magnitude of mass and size, limiting numerical issues like artificial disruption of poorly resolved low-mass substructures (see van den Bosch et al., 2018). Motivated by the mounting observational evidence of DM cores in Milky Way dwarfs (see e.g. Walker & Peñarrubia, 2011; Amorisco et al., 2013), we run simulations assuming either cuspy or cored Dehnen (1993) DM density profiles for the subhaloes at infall. Furthermore, we apply the minimum variance mass estimator to a catalogue Milky Way dwarf galaxies (McConnachie, 2012), showing a tight correlation between enclosed mass $M(<1.8\,R_{\rm h})$ and luminosity $L_\star$. Using empirical functions (*tidal tracks*) fitted to the evolution of stellar tracers embedded in the DM subhaloes of our re-simulations of the Aquarius A2 merger tree, we show that the correlation between enclosed mass and luminosity does not evolve significantly due to tidal stripping even when dwarfs lose more than one order of magnitude of their initial mass. Our results suggest that the currently observed correlation is mainly driven by internal processes such as star-formation and feedback. We furthermore find that the mean densities $\langle\varrho(<1.8\,R_{\rm h})\rangle$ of ultrafaint galaxies are too high to be compatible with any of the simulated cored DM haloes, and show that tidal evolution further increases this discrepancy. This is a consequence of our choice of core size of the simulated DM haloes (a core size equal to the scale radius), and our findings suggest that the densities of ultra faint galaxies require core sizes that are much smaller than the scale radius of the DM halo.

Constraints on the total halo mass from measurements of $\langle\sigma^2_{\rm los}\rangle$ and $R_{\rm h}$ alone are weak given our ignorance on how deeply embedded the stellar population is within the DM halo. For two-parameter DM density profiles - like the $\{\alpha,\beta,\gamma\}=\{1,5,0\}$ and $\{1,5,1\}$ profiles - the measurements of $\langle\sigma^2_{\rm los}\rangle$ and $R_{\rm h}$ however do constrain the DM halo structural parameters $\{r_{\rm max}, v_{\rm max}\}$ to follow a one-dimensional degeneracy curve which can be cast as a function of the segregation parameter $R_{\rm h}/r_{\rm max}$. Using our re-simulations of the Aquarius merger tree, we break this degeneracy by selecting those simulated DM subhaloes with $\{r_{\rm max}, v_{\rm max}\}$ values consistent with the degeneracy curve. This allows us to infer the total halo masses of Milky Way dwarf galaxies, assuming that the simulated subhaloes are representative of the population of Milky Way subhaloes.

We have tested this method using mocks generated from re-simulations of the Aquarius merger tree and show that total halo masses are robustly recovered with an uncertainty of the order of unity for both cuspy and cored DM haloes. Our findings suggest that the classical Milky Way dSphs are embedded in haloes spanning a narrow range of masses, $8 < \log_{10}(M/\mathrm{M}_\odot) < 10$, with no clear trend with either galaxy size or luminosity. Surprisingly, we find that stellar mass and total halo mass of ultrafaint galaxies are *anticorrelated*, i.e. the halo mass *decreases* with increasing stellar mass. We caution that this anticorrelation may be caused by either observational inaccuracies (contamination by foreground stars, inflated velocity dispersions due to binary motion), or that the Aquarius A2 merger tree does not contain subhaloes representative of those of ultrafaint dwarfs.

With velocity measurements becoming available also tangentially to the line of sight (e.g. Massari et al., 2018), note that it is straightforward to extend the virial mass estimator to systems with full kinematic information, as the spherical virial theorem reads (cf. equations 4.1 – 4.3):

$$\langle\sigma^2_{\mathrm{los}}\rangle + \langle\sigma^2_\alpha\rangle + \langle\sigma^2_\delta\rangle = 4\pi G \int_0^\infty r\nu_\star(r)M(<r)\mathrm{d}r \ , \tag{4.21}$$

with $\langle\sigma^2_\alpha\rangle$ and $\langle\sigma^2_\delta\rangle$ denoting the luminosity-averaged squared velocity dispersions of the two velocity components tangential to the line of sight.

Appendix to Chapter 4

4.A Tidal evolutionary tracks

Structural parameters of tidally stripped dwarf galaxies can be parametrized as simple analytical functions which depend only on the total fraction of mass lost, but not on the specific orbit of the dwarf, or the host potential. This has been first discussed by Peñarrubia et al. (2008b) for the case of spherical stellar systems embedded in cuspy DM haloes, who named these analytical functions *tidal evolutionary tracks*. Similarly, Errani et al. (2015) discuss tidal tracks for spherical dwarf galaxies with cored DM haloes, whereas Sanders et al. (2018) study dwarf galaxies where both the stellar tracer and the DM halo are flattened. In the following, we derive such tracks for DM subhaloes and dwarf galaxies in the re-simulations of the Aquarius A2 merger tree discussed in section 4.3.2. In contrast to the tracks of Peñarrubia et al. (2008b), instead of fitting the evolution of single galaxies on different orbits at subsequent apocentres, we fit tracks to the entire population of simulated dwarf galaxies at $z = 0$. We fit the DM halo radius of maximum circular velocity $r_{\rm max}$, the total stellar mass of the embedded stellar population $M_\star$ and the half-light radius $R_{\rm h}$, normalized by their initial values (i.e. at $z_{\rm infall}$), as functions of the remnant mass fraction $M_{\rm max}$ enclosed within $r_{\rm max}$. This parametrisation is motivated by the fact that the enclosed mass $M_{\rm max}$ can be measured directly from the N-body snapshots of the simulation, without having to assume a specific mass profile. For the fits, we adapt the empirical formula of Peñarrubia et al. (2008b) introducing as third parameter the scale x_s:

$$g(x) = \frac{(1+x_s)^\alpha \; x^\beta}{(x+x_s)^\alpha} \qquad \text{with} \qquad x = M_{\rm max}/M_{\rm max,0} \quad , \tag{4.A.1}$$

where $g(x) = r_{\rm max}(x)/r_{\rm max,0}$, $M_\star(x)/M_{\star,0}$ or $R_{\rm h}(x)/R_{\rm h,0}$, respectively, subscript zero denoting values at infall. We introduce the scale x_s to use the same parametrisation $x = M_{\rm max}/M_{\rm max,0}$ for both the DM- and the stellar tracks: the choice of $x_s = 1$ in the formula of Peñarrubia et al. (2008b) was adapted for tidal tracks parametrized by mass lost within the initial half-light radius, but does not yield reasonable fits for structural parameters of the stellar population when expressing the tidal tracks as functions of $x = M_{\rm max}/M_{\rm max,0}$. We do not fit the scale parameter x_s, but where the functional shape of $g(x)$ requires it, we use as scale the initial fraction of mass enclosed within the initial half-light radius: $x_s = (1 + a_0/R_{\rm h,0})^{\gamma-3}$, where by a_0 we denote the Dehnen (1993) scale radius of the halo at infall. This choice reduces the dependence of the fits on segregation, and motivated the choice of $x_s = 1$ in the stellar tracks derived by Peñarrubia et al. (2008b). We fit tidal tracks separately for cuspy ($\gamma = 1$) and cored ($\gamma = 0$) dwarf galaxies which at $z_{\rm infall}$ had Dehnen (1993) density profiles, i.e. $\{\alpha, \beta, \gamma\} = \{1, 4, \gamma\}$. Fits are done separately for two stellar populations with initial segregations of $R_{\rm h,0}/r_{\rm max,0} = 1/20$ and $1/10$. To limit the impact of

numerical artefacts caused by the spatial resolution of the particle mesh code, the highest resolving co-moving grid having a spacing of $r_{\rm max,0}/128$, we include only haloes in the fits with $r_{\rm max}/r_{\rm max,0} > 1/10$. We only consider bound N-body particles for the fits, and fit only haloes where both the DM and the stellar tracer are approximately in virial equilibrium, requiring that $|2K + W|/(2K - W) < 0.2$ for the DM enclosed within $r_{\rm max}$, and $|2K_{\rm los} + W_{\rm los}|/(2K_{\rm los} - W_{\rm los}) < 0.05$ for the stars. Halo properties are then averaged in logarithmically spaced bins spanning $0.01 \leq M_{\rm max}/M_{\rm max,0} \leq 1$ to avoid giving different weight to various mass fractions based on the halo abundance at that mass fraction. The empirical fit parameters are listed in Table 4.A.1. Fig. 4.A.1 shows the fitted tidal tracks, as well as the parameters of single dwarf galaxies at $z = 0$ used for the fit. Note that $r_{\rm max}$ of cored dwarf galaxies decreases less rapidly during tidal stripping than for their cuspy counterparts, and half-light radii of stellar populations embedded in cored DM haloes expand during tidal stripping.

Table 4.A.1: Empirical fit parameters for equation 4.A.1. By $r_{\rm max/0} \equiv r_{\rm max}/r_{\rm max,0}$ we denote the radius of maximum circular velocity of the DM halo at $z = 0$, normalized by its initial value. Similarly, $M_{\star/0} \equiv M_\star/M_{\star,0}$ and $R_{\rm h/0} \equiv R_{\rm h}/R_{\rm h,0}$ are the total stellar mass and half-light radius of stellar populations embedded inside the DM halo, normalized by their respective initial value. We separately list parameters for two stellar populations with initial segregations of $R_{\rm h,0}/r_{\rm max,0} = 1/20$ and $1/10$.

		Cusp			Core		
	$R_{\rm h,0}/r_{\rm max,0}$	α	β	$\log_{10} x_s$	α	β	$\log_{10} x_s$
$r_{\rm max/0}$	–	0.00	0.48	0.00	-0.85	0.00	0.00
$M_{\star/0}$	1/20	1.87	1.87	-2.64	2.83	2.83	-3.12
	1/10	1.80	1.80	-2.08	2.05	2.05	-2.33
$R_{\rm h/0}$	1/20	0.47	0.41	-2.64	-0.25	-0.25	0.00
	1/10	0.50	0.42	-2.08	-0.23	-0.23	0.00

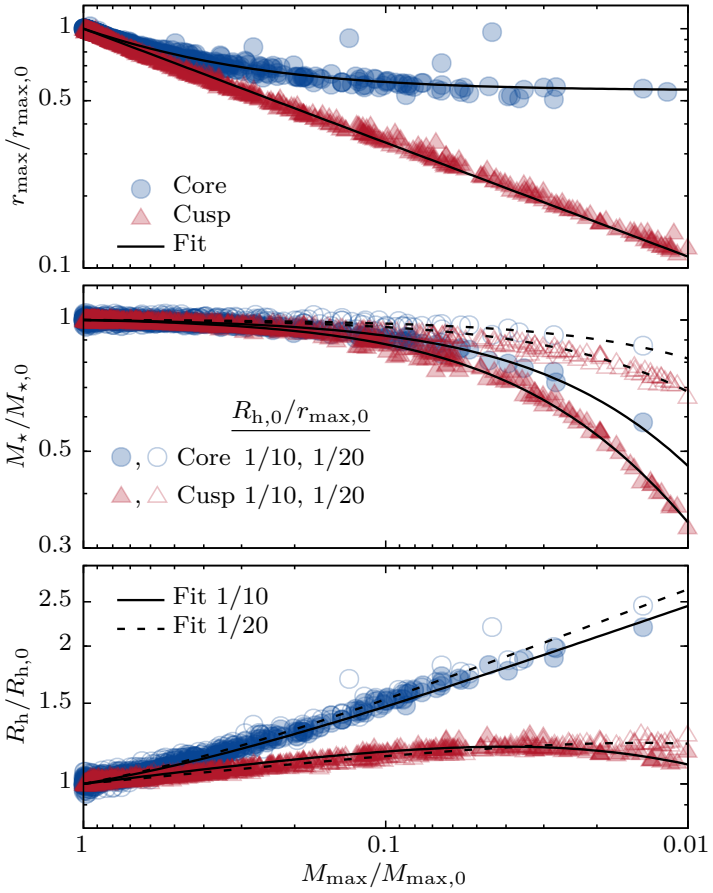

Figure 4.A.1: Structural properties of dwarf galaxies are simple functions of the remnant bound mass only. The top panel shows $r_{\rm max}$ of the underlying DM halo, normalized by its initial value $r_{\rm max,0}$, as a function of the mass $M_{\rm max}/M_{\rm max,0}$ enclosed within $r_{\rm max}$. The evolution of $r_{\rm max}$ is shown separately for cuspy (red triangles) and cored (blue circles) DM profiles. The central and bottom panel show the evolution of the stellar mass and half-light radii of stellar populations embedded inside the DM haloes with initial segregation of $R_{\rm h,0}/r_{\rm max,0} = 1/10$ (filled symbols), 1/20 (open symbols).

Chapter 5

Conclusions

Dwarf spheroidal (dSph) galaxies, lying at the faintest end of the galaxy luminosity function, are the most dark matter (DM) dominated systems observed to date: in equilibrium, their dynamics cannot be explained by (Newtonian) gravity sourced from their stellar component alone. The faintest of systems reach dynamical mass-to-light ratios as large as $\sim 10^4$ (e.g. McConnachie, 2012; Simon, 2019). They therefore present a compelling window on the clustering of DM on galactic scales - where DM (e.g. particle) properties and potential interactions with baryons play a crucial role for the distribution of DM (e.g. Kuhlen et al., 2012; Bullock & Boylan-Kolchin, 2017; Strigari, 2018).

This thesis discusses the tidal evolution of dSph galaxies embedded in DM subhaloes, as well as their abundance and observable properties in the light of different models for distribution of DM on kpc scales.

Cuspy subhaloes and embedded dSph galaxies survive tidal stripping. *Chapter 2*

(i) We argue that dark matter subhaloes with centrally divergent *cuspy* density profiles cannot be completely disrupted by smooth tidal fields. This applies also to dSph galaxies embedded in such cuspy DM subhaloes. Dynamical times in cuspy subhaloes become arbitrarily small for $r \to 0$. Consequently tidal interactions between a subhalo and its host galaxy are experienced as mere adiabatic perturbations for particles in the central regions of the subhalo. Crucially, tidal evolution of cuspy subhaloes increases the relative fraction of particles that react adiabatically to tidal perturbations.

(ii) For subhaloes with constant density cores however, dynamical times reach a finite (non-zero) value in their centre. Tidal evolution in cored subhaloes increases the central dynamical time and thereby decreases the fraction of particles that may react adiabatically to tides. This drives the tidal disruption of cored subhaloes.

(iii) In agreement with previous studies, we furthermore show that insufficient numerical resolution of collisionless N-body simulation causes the formation of density cores in subhaloes, which subsequently facilitate their *artificial* tidal disruption.

We develop a re-simulation technique that reconstructs the density cusp in numerical simulations and allows to follow the tidal evolution of cuspy subhaloes for arbitrarily large fractions of tidally stripped mass. Using a distribution-function based approach, we embed stars in these models to study the tidal evolution of dSph galaxies, noting that tidal evolution of cuspy subhaloes may cause the formation of shallow density cusps also in the stellar population.

(iv) We show that tides can strip dSph galaxies in cuspy subhaloes down to subsolar luminosity. During tidal stripping, the half-light radii and stellar velocity dispersions of dSphs decrease while their dynamical mass-to-light ratios increase. The remnant 'micro-galaxies' would appear as co-moving groups of metal-poor, low-mass stars of similar age, embedded in sub-kpc DM subhaloes. We illustrate this using the Tucana III dSph galaxy as an example. Stripping the dwarf model to a remnant luminosity of $L \approx 1 L_{\odot}$, the evolved system has a half-light radius of $\approx 20\,\mathrm{pc}$ and a luminosity-averaged velocity dispersion of $\approx 0.5\,\mathrm{km/s}$.

Chapter 3 **The galactic disc drives tidal depletion.**

(v) Using controlled simulations of the formation of Milky Way-like DM haloes, we show how (a) the inner subhalo profile shape and (b) the presence of a galactic disc effects the abundance of subhaloes. We find that at redshift $z = 0$, models with cored subhaloes (with a core size of the order of the DM scale radius) have half as many surviving subhaloes within the virial radius r_{200} of the host halo as their cuspy counterparts, and four times less if considering only subhaloes with pericentre distances $r_p \lesssim 0.1\, r_{200}$. The presence of a galactic disc reduces the number of subhaloes further by a factor of $\lesssim 2$ for subhaloes on orbits that pass through the disc.

(vi) These results are obtained from re-simulation of all subhaloes of the Aquarius A2 merger tree with masses $M \geq 10^8\,\mathrm{M}_{\odot}$ at accretion, i.e. those subhaloes sufficiently massive to allow star formation. Each subhalo is modelled using $N = 2 \times 10^6$ particles (and $N = 10^7$ in a second suite of simulations) independently of subhalo mass with the aim to follow all subhaloes with the same relative numerical resolution. This is of particular relevance in the context of *artificial* disruption of low-mass substructures in cosmological simulations due to insufficient resolution. In the light of the apparent *indestructability* of cuspy subhaloes discussed in chapter 2, note that also these re-simulations are limited by a finite N-body particle number per subhalo and a constant spatial resolution defined for each subhalo at infall. Consequently also these re-simulations do not fully prevent artificial disruption: at redshift $z = 0$, approximately 200 of the simulated $\sim 10^3$ cuspy subhaloes have been stripped to masses below the resolution limit.

(vii) We furthermore fit empirical formulae in the style of Peñarrubia et al. (2008b) to the population of simulated subhaloes at $z = 0$, describing the tidal evolution

of their structural parameters as functions of their remnant bound mass fraction. Deriving such empirical relations from controlled re-simulations with cosmologically motivated initial conditions is particularly important for subhaloes with constant-density cores (and dwarf galaxies embedded in such haloes), as the response of cored systems to tides is sensitive to their individual density profiles and orbital distribution.

Mass estimates with minimum uncertainty: use the virial theorem. *Chapter 4*

(viii) To confront observed properties of Milky Way dSph galaxies to numerical simulations, we construct an estimator for enclosed masses based on the virial theorem, insensitive to velocity anisotropy and tailored to yield masses with minimum uncertainty introduced by our ignorance on (a) the shape of the inner DM profile, and (b) how deeply the stellar component is embedded within the subhalo. The estimator reads:

$$M_{\rm est}(< 1.8\,R_{\rm h}) \approx 3.5 \times 1.8\,R_{\rm h}\,G^{-1}\,\langle\sigma^2_{\rm los}\rangle \qquad \text{(see Eq. 4.12)}$$

where by $R_{\rm h}$ we denote the projected half-light radius and by $\langle\sigma^2_{\rm los}\rangle$ the luminosity-averaged squared velocity dispersion. We have tested the mass estimator on a suite of N-body mocks extracted from controlled re-simulations of the Aquarius A2 merger tree, and recover the enclosed masses with an accuracy of $\lesssim 10$ per cent in systems with mass-loss fractions that differ by orders of magnitude. We also quantify systematic deviations of density slopes $\mathrm{d}\ln\rho(r)/\mathrm{d}\ln r$ inferred from mass estimates of two distinct stellar populations: the inferred slopes are sensitive to the profile shapes assumed for the stellar populations, necessitating accurate modelling for reliable slope estimates.

(ix) Applying the mass estimator to a sample of Milky Way dSph galaxies, we find a tight correlation between enclosed mass and luminosity, and show based on the results of numerical simulations that tidal mass loss has little effect on the evolution of this correlation.

(x) With the aim to estimate *total* halo masses, we match structural parameters of Milky Way dSphs to simulated subhaloes from re-simulations of the Aquarius A2 merger tree. We find that the high mass densities of ultrafaint galaxies are not compatible with large DM cores, and that the total halo masses of the classical Milky Way dSph galaxies span a remarkably narrow range ($8 \lesssim \log_{10}(M/\mathrm{M}_\odot) \lesssim 10$) at present, showing no clear trend with either galaxy size or luminosity.

Outlook

Ultra-faint dwarfs

The number of known Milky Way dwarf spheroidal galaxies has more than doubled within the last decade (Simon, 2019, figure 1), and wide-field surveys like CFIS (Ibata et al., 2017) promise further discoveries of (ultra-)faint systems in the coming years. Robust mass estimators with simple systematics like the virial estimator of chapter 4.3 can be used to infer the dark matter content of such faint galaxies hosting only a small number of stars.

Internal kinematics

Accurate measurements of the internal kinematics of dwarf galaxies, accessible with instruments like the Subaru PFS (Takada et al., 2014), can help to decide whether the high central densities of ultra-faint galaxies require dark matter cusps, or whether they result compatible with cored density profiles, as discussed in section 4.5.2. Repeated measurements of single-star velocities as performed by Koposov et al. (2011), and the inclusion of velocity components orthogonal to the line-of-sight (Massari et al., 2018), can yield further improvements on the inferred internal velocity dispersions and on derived constraints on masses and shapes of dark matter subhaloes.

Orbital constraints

Proper motion measurements obtained from current and upcoming data releases of the Gaia satellite (Gaia Collaboration et al., 2018) allow to model the orbits and the tidal stripping of dwarf galaxies in the Milky Way. The tidal evolutionary tracks of chapter 4.A may be used to reconstruct the initial properties of Milky Way dwarf galaxies before accretion (e.g. Fattahi et al., 2018). Similar strategies may be used to model the different tidal evolution of dwarf galaxies embedded in cuspy or cored dark matter subhaloes, e.g. with the aim to understand formation mechanisms for ultra-faint and ultra-diffuse galaxies (e.g. Carleton et al., 2019).

Micro-galaxies

Statistics on the abundance of co-moving groups of stars, derived from surveys of metal-poor stars in the Milky Way stellar halo (e.g. Pristine, see Starkenburg et al., 2017) and potential kinematic follow-up, may be used to confront the predictions of chapter 2.5 on the structural properties of highly tidally stripped dwarf galaxy remnants against observational data.

Dark subhaloes

Similarly, the survival of dark matter subhaloes discussed in chapter 3.3 has implications for potential detection of subhaloes (including those which do not host stars) through strong gravitational lensing (e.g. Vegetti & Koopmans, 2009; Despali & Vegetti, 2017), annihilation signals (e.g. Lavalle et al., 2007; Stref et al., 2019), and the number of gaps in stellar tidal streams (e.g. Ibata et al., 2002; Erkal & Belokurov, 2015).

References

Aarseth S. J., Gott III J. R., Turner E. L., 1979, ApJ, 228, 664
Adén D., et al., 2009, ApJ, 706, L150
Agnello A., Evans N. W., 2012, ApJ, 754, L39
Agnello A., Evans N. W., Romanowsky A. J., 2014, MNRAS, 442, 3284
Aguilar L., Hut P., Ostriker J. P., 1988, ApJ, 335, 720
Amorisco N. C., Evans N. W., 2011, MNRAS, 411, 2118
Amorisco N. C., Evans N. W., 2012, MNRAS, 419, 184
Amorisco N. C., Agnello A., Evans N. W., 2013, MNRAS, 429, L89
Barnes J., Hut P., 1986, Nature, 324, 446
Battaglia G., et al., 2008, ApJ, 681, L13
Bechtol K., et al., 2015, ApJ, 807, 50
Behroozi P. S., Wechsler R. H., Conroy C., 2013, ApJ, 770, 57
Belokurov V., et al., 2008, ApJ, 686, L83
Belokurov V., et al., 2009, MNRAS, 397, 1748
Belokurov V., et al., 2010, ApJ, 712, L103
Benson A. J., et al., 2002, MNRAS, 333, 177
Binney J., Mamon G. A., 1982, MNRAS, 200, 361
Binney J., Tremaine S., 1987, Galactic dynamics
Bird S., et al., 2016, Physical Review Letters, 116, 201301
Blumenthal G. R., Faber S. M., Primack J. R., Rees M. J., 1984, Nature, 311, 517
de Boer T. J. L., et al., 2012, A&A, 544, A73
Bond J. R., Kofman L., Pogosyan D., 1996, Nature, 380, 603
van den Bosch F. C., Ogiya G., 2018, MNRAS, 475, 4066
van den Bosch F. C., Tormen G., Giocoli C., 2005, MNRAS, 359, 1029
van den Bosch F. C., Ogiya G., Hahn O., Burkert A., 2018, MNRAS, 474, 3043
Boylan-Kolchin M., Bullock J. S., Kaplinghat M., 2011, MNRAS, 415, L40
Breddels M. A., et al., 2013, MNRAS, 433, 3173
Bressan A., et al., 2012, MNRAS, 427, 127
Buist H. J. T., Helmi A., 2014, A&A, 563, A110
Bullock J. S., Boylan-Kolchin M., 2017, ARA&A, 55, 343
Bullock J. S., Johnston K. V., 2005, ApJ, 635, 931
Bullock J. S., Kravtsov A. V., Weinberg D. H., 2000, ApJ, 539, 517
Bullock J. S., et al., 2001, MNRAS, 321, 559
Caldwell N., et al., 2017, ApJ, 839, 20
Campbell D. J. R., et al., 2017, MNRAS, 469, 2335
Cappellari M., et al., 2006, MNRAS, 366, 1126
Carleton T., et al., 2019, MNRAS, 485, 382
Cautun M., Frenk C. S., 2017, MNRAS, 468, L41
Chan T. K., et al., 2015, MNRAS, 454, 2981
Chandrasekhar S., 1943, ApJ, 97, 255
Cole S., Lacey C., 1996, MNRAS, 281, 716
Collins M. L. M., et al., 2014, ApJ, 783, 7
D'Onghia E., Springel V., Hernquist L., Keres D., 2010, ApJ, 709, 1138
Davis M., Huchra J., Latham D. W., Tonry J., 1982, ApJ, 253, 423
Davis M., Efstathiou G., Frenk C. S., White S. D. M., 1985, ApJ, 292, 371
Dehnen W., 1993, MNRAS, 265, 250
Dehnen W., 2002, Journal of Computational Physics, 179, 27
Dekel A., Silk J., 1986, ApJ, 303, 39
Delos M. S., 2019, arXiv e-prints, arXiv:1907.13133
Despali G., Vegetti S., 2017, MNRAS, 469, 1997
Despali G., Giocoli C., Tormen G., 2014, MNRAS, 443, 3208
Di Cintio A., et al., 2014, MNRAS, 441, 2986
Diakogiannis F. I., Lewis G. F., Ibata R. A., 2014, MNRAS, 443, 598

Diakogiannis F. I., et al., 2017, MNRAS, 470, 2034
Diemand J., Moore B., Stadel J., 2005, Nature, 433, 389
Diemand J., Kuhlen M., Madau P., 2007, ApJ, 657, 262
Diemand J., et al., 2008, Nature, 454, 735
Drlica-Wagner A., et al., 2015, ApJ, 813, 109
Dror J. A., Ramani H., Trickle T., Zurek K. M., 2019, arXiv e-prints, arXiv:1901.04490
Efstathiou G., Eastwood J. W., 1981, MNRAS, 194, 503
Elbert O. D., et al., 2015, MNRAS, 453, 29
Erkal D., Belokurov V., 2015, MNRAS, 450, 1136
Erkal D., et al., 2018, MNRAS, 481, 3148
Errani R., Peñarrubia J., 2019, arXiv e-prints, arXiv:1906.01642
Errani R., Peñarrubia J., Tormen G., 2015, MNRAS, 449, L46
Errani R., Peñarrubia J., Laporte C. F. P., Gómez F. A., 2017, MNRAS, 465, L59
Errani R., Peñarrubia J., Walker M. G., 2018, MNRAS, 481, 5073
Fattahi A., et al., 2016, arXiv e-prints, arXiv:1607.06479
Fattahi A., et al., 2018, MNRAS, 476, 3816
Fellhauer M., Lin D. N. C., 2007, MNRAS, 375, 604
Fellhauer M., et al., 2000, NA, 5, 305
Frenk C. S., White S. D. M., 2012, Annalen der Physik, 524, 507
Frenk C. S., White S. D. M., Davis M., Efstathiou G., 1988, ApJ, 327, 507
Fujii M., Funato Y., Makino J., 2006, PASJ, 58, 743
Gaia Collaboration et al., 2018, A&A, 616, A1
Gao L., et al., 2004, MNRAS, 355, 819
Gao L., et al., 2008, MNRAS, 387, 536
Garrison-Kimmel S., et al., 2017, MNRAS, 471, 1709
Geha M., et al., 2009, ApJ, 692, 1464
Genina A., et al., 2018, MNRAS, 474, 1398
Gill S. P. D., Knebe A., Gibson B. K., Dopita M. A., 2004, MNRAS, 351, 410
Giocoli C., Tormen G., van den Bosch F. C., 2008, MNRAS, 386, 2135
Gnedin N. Y., 2000, ApJ, 542, 535
Goerdt T., et al., 2007, MNRAS, 375, 191
González-Samaniego A., et al., 2017, MNRAS, 472, 4786
Griffen B. F., et al., 2016, ApJ, 818, 10
Harris W. E., 1996, AJ, 112, 1487
Hayashi E., et al., 2003, ApJ, 584, 541
Hayashi E., et al., 2004, MNRAS, 355, 794
Hernquist L., 1990, ApJ, 356, 359
Hockney R. W., Eastwood J. W., 1988, Computer simulation using particles
Hopkins P. F., et al., 2014, MNRAS, 445, 581
Hu W., Barkana R., Gruzinov A., 2000, Physical Review Letters, 85, 1158
Ibata R. A., et al., 1997, AJ, 113, 634
Ibata R. A., Lewis G. F., Irwin M. J., Quinn T., 2002, MNRAS, 332, 915
Ibata R. A., et al., 2013, Nature, 493, 62
Ibata R. A., et al., 2014, ApJ, 784, L6
Ibata R. A., et al., 2017, ApJ, 848, 128
Illingworth G., 1976, ApJ, 204, 73
Jiang F., van den Bosch F. C., 2016, MNRAS, 458, 2848
Kamdar H., et al., 2019, arXiv e-prints, arXiv:1904.02159
Kashiyama K., Oguri M., 2018, arXiv e-prints, arXiv:1801.07847
Kazantzidis S., et al., 2004, ApJ, 608, 663
Kirby E. N., et al., 2013, ApJ, 779, 102
Klypin A., Gottlöber S., Kravtsov A. V., Khokhlov A. M., 1999a, ApJ, 516, 530
Klypin A., Kravtsov A. V., Valenzuela O., Prada F., 1999b, ApJ, 522, 82
Klypin A. A., Trujillo-Gomez S., Primack J., 2011, ApJ, 740, 102
Klypin A., et al., 2016, MNRAS, 457, 4340
Koch A., et al., 2007, AJ, 134, 566
Koch A., et al., 2009, ApJ, 690, 453
Koposov S. E., et al., 2011, ApJ, 736, 146
Koposov S. E., Belokurov V., Torrealba G., Evans N. W., 2015, ApJ, 805, 130
Kroupa P., Theis C., Boily C. M., 2005, A&A, 431, 517

Kuhlen M., Vogelsberger M., Angulo R., 2012, Physics of the Dark Universe, 1, 50
Laporte C. F. P., Peñarrubia J., 2015, MNRAS, 449, L90
Laporte C. F. P., White S. D. M., 2015, MNRAS, 451, 1177
Laporte C. F. P., Walker M. G., Peñarrubia J., 2013, MNRAS, 433, L54
Laporte C. F. P., Agnello A., Navarro J. F., 2019, MNRAS, 484, 245
Lavalle J., Pochon J., Salati P., Taillet R., 2007, A&A, 462, 827
Li T. S., et al., 2018, ApJ, 866, 22
Libeskind N. I., et al., 2005, MNRAS, 363, 146
Łokas E. L., 2009, MNRAS, 394, L102
Łokas E. L., Mamon G. A., 2003, MNRAS, 343, 401
Łokas E. L., et al., 2010, ApJ, 725, 1516
Lovell M. R., et al., 2014, MNRAS, 439, 300
Ludlow A. D., et al., 2013, MNRAS, 432, 1103
Ludlow A. D., et al., 2014, MNRAS, 441, 378
Lux H., Read J. I., Lake G., 2010, MNRAS, 406, 2312
Lynden-Bell D., 1976, MNRAS, 174, 695
Macciò A. V., et al., 2012, MNRAS, 424, 1105
Martin N. F., et al., 2007, MNRAS, 380, 281
Martin N. F., de Jong J. T. A., Rix H.-W., 2008, ApJ, 684, 1075
Massari D., et al., 2018, Nature Astronomy, 2, 156
Mateo M. L., 1998, ARA&A, 36, 435
Mateo M., et al., 1993, AJ, 105, 510
Mateo M., Olszewski E. W., Walker M. G., 2008, ApJ, 675, 201
McConnachie A. W., 2012, AJ, 144, 4
McConnachie A. W., Côté P., 2010, ApJ, 722, L209
McMillan P. J., 2011, MNRAS, 414, 2446
Merrifield M. R., Kent S. M., 1990, AJ, 99, 1548
Merritt D., 1987, ApJ, 313, 121
Miyamoto M., Nagai R., 1975, PASJ, 27, 533
Moore B., et al., 1998, ApJ, 499, L5
Moore B., et al., 1999, ApJ, 524, L19
Moster B. P., et al., 2010, ApJ, 710, 903
Murray C. D., Dermott S. F., 1999, Solar system dynamics
Nagai R., Miyamoto M., 1976, PASJ, 28, 1
Navarro J. F., White S. D. M., 1993, MNRAS, 265, 271
Navarro J. F., Eke V. R., Frenk C. S., 1996, MNRAS, 283, L72
Navarro J. F., Frenk C. S., White S. D. M., 1997, ApJ, 490, 493
Navarro J. F., et al., 2004, MNRAS, 349, 1039
Navarro J. F., et al., 2010, MNRAS, 402, 21
Nipoti C., Binney J., 2015, MNRAS, 446, 1820
Oñorbe J., et al., 2015, MNRAS, 454, 2092
Oman K. A., et al., 2015, MNRAS, 452, 3650
Ostriker J. P., Spitzer Jr. L., Chevalier R. A., 1972, ApJ, 176, L51
Pascale R., Posti L., Nipoti C., Binney J., 2018, MNRAS, 480, 927
Peñarrubia J., 2019, MNRAS, 484, 5409
Peñarrubia J., McConnachie A. W., Navarro J. F., 2008a, ApJ, 672, 904
Peñarrubia J., Navarro J. F., McConnachie A. W., 2008b, ApJ, 673, 226
Peñarrubia J., Navarro J. F., McConnachie A. W., Martin N. F., 2009, ApJ, 698, 222
Peñarrubia J., et al., 2010, MNRAS, 406, 1290
Peñarrubia J., Pontzen A., Walker M. G., Koposov S. E., 2012, ApJ, 759, L42
Peñarrubia J., et al., 2016a, MNRAS, 456, L54
Peñarrubia J., Ludlow A. D., Chanamé J., Walker M. G., 2016b, MNRAS, 461, L72
Planck Collaboration et al., 2018, arXiv e-prints, arXiv:1807.06209
Pontzen A., Governato F., 2012, MNRAS, 421, 3464
Power C., et al., 2003, MNRAS, 338, 14
Prada F., et al., 2012, MNRAS, 423, 3018
Press W. H., Teukolsky S. A., Vetterling W. T., Flannery B. P., 1992, Numerical recipes
Read J. I., Gilmore G., 2005, MNRAS, 356, 107
Read J. I., Steger P., 2017, MNRAS, 471, 4541
Read J. I., Agertz O., Collins M. L. M., 2016, MNRAS, 459, 2573

Renaud F., Gieles M., Boily C. M., 2011, MNRAS, 418, 759
Richardson T., Fairbairn M., 2014, MNRAS, 441, 1584
Richings J., et al., 2018, arXiv e-prints, arXiv:1811.12437
Riley A. H., et al., 2019, MNRAS, 486, 2679
Rocha M., et al., 2013, MNRAS, 430, 81
Saglia R. P., Kronawitter A., Gerhard O., Bender R., 2000, AJ, 119, 153
Sanders J. L., Evans N. W., Dehnen W., 2018, MNRAS, 478, 3879
Sawala T., et al., 2015, MNRAS, 448, 2941
Sawala T., et al., 2016, MNRAS, 457, 1931
Sawala T., et al., 2017, MNRAS, 467, 4383
Schaye J., et al., 2015, MNRAS, 446, 521
Shipp N., et al., 2018, ApJ, 862, 114
Simon J. D., 2018, ApJ, 863, 89
Simon J. D., 2019, arXiv e-prints, arXiv:1901.05465
Simon J. D., Geha M., 2007, ApJ, 670, 313
Simon J. D., et al., 2017, ApJ, 838, 11
Spencer M. E., et al., 2018, AJ, 156, 257
Spergel D. N., Steinhardt P. J., 2000, Physical Review Letters, 84, 3760
Spitzer L., 1987, Dynamical evolution of globular clusters
Springel V., et al., 2008, MNRAS, 391, 1685
Starkenburg E., et al., 2017, MNRAS, 471, 2587
Stref M., Lacroix T., Lavalle J., 2019, arXiv e-prints, arXiv:1905.02008
Strigari L. E., 2018, Reports on Progress in Physics, 81, 056901
Strigari L. E., Bullock J. S., Kaplinghat M., 2007, ApJ, 657, L1
Strigari L. E., et al., 2008, Nature, 454, 1096
Strigari L. E., Frenk C. S., White S. D. M., 2017, ApJ, 838, 123
Takada M., et al., 2014, PASJ, 66, R1
Tormen G., Bouchet F. R., White S. D. M., 1997, MNRAS, 286, 865
Torrealba G., Koposov S. E., Belokurov V., Irwin M., 2016, MNRAS, 459, 2370
Tremaine S., Gunn J. E., 1979, Physical Review Letters, 42, 407
Ural U., Wilkinson M. I., Read J. I., Walker M. G., 2015, Nature Communications, 6, 7599
Vegetti S., Koopmans L. V. E., 2009, MNRAS, 400, 1583
Velazquez H., White S. D. M., 1999, MNRAS, 304, 254
Vogelsberger M., Zavala J., Loeb A., 2012, MNRAS, 423, 3740
Walker M. G., Peñarrubia J., 2011, ApJ, 742, 20
Walker M. G., et al., 2007, ApJ, 667, L53
Walker M. G., et al., 2009a, AJ, 137, 3109
Walker M. G., et al., 2009b, ApJ, 694, L144
Walker M. G., et al., 2009c, ApJ, 704, 1274
Wang W., et al., 2015, MNRAS, 453, 377
Watkins L. L., van de Ven G., den Brok M., van den Bosch R. C. E., 2013, MNRAS, 436, 2598
Weinberg M. D., 1994a, AJ, 108, 1398
Weinberg M. D., 1994b, AJ, 108, 1403
Weinberg M. D., 1994c, AJ, 108, 1414
White S. D. M., Rees M. J., 1978, MNRAS, 183, 341
Wolf J., et al., 2010, MNRAS, 406, 1220
Yurin D., Springel V., 2015, MNRAS, 452, 2367
Zehavi I., et al., 2002, ApJ, 571, 172
Zentner A. R., Kravtsov A. V., Gnedin O. Y., Klypin A. A., 2005, ApJ, 629, 219
Zhu Q., et al., 2016, MNRAS, 458, 1559

BT87 see Binney & Tremaine (1987)
P+92 see Press et al. (1992)
HE88 see Hockney & Eastwood (1988)
MD99 see Murray & Dermott (1999)
S87 see Spitzer (1987)

Paper 1 see Errani, Peñarrubia, Laporte & Gómez (2017)
Paper 2 see Errani, Peñarrubia & Walker (2018)
Paper 3 see Errani & Peñarrubia (2019)

Acknowledgements

Thank you Jorge, for the enthusiastic yet patient guidance during these years, with plenty of walks up Blackford hill and wee espresso chats.

The *Cusp Core Comparison Project* has been a tremendously enjoyable collaboration thanks to the devotion of Chervin Laporte and Facundo Gómez.

Matt Walker has played a significant role in the discussions leading to the *virial mass estimator*, and was a marvellous host at Carnegie Mellon University during my visit in February 2019.

Thanks Annette Ferguson, for reminding me gently to build models that can be compared to observations, and general academic career advice.

Grazie Bepi.